DIFFUSIONAL MOTION AS A GAUGE OF INTERFACIAL FLUIDITY AND ADHESION OF SUPPORTED MODEL MEMBRANE FILMS

By

Stephen M Baumler

A DISSERTATION

Submitted to
Michigan State University
in partial fulfillment of the requirements
for the degree of

Chemistry – Doctor of Philosophy

2017

ABSTRACT

DIFFUSIONAL MOTION AS A GAUGE OF INTERFACIAL FLUIDITY AND ADHESION OF SUPPORTED MODEL MEMBRANE FILMS

By

Stephen M Baumler

The plasma membrane plays an important role in cellular processes. Not only does the membrane act as a barrier to the outside world, compartmentalizing cell functions by providing a two-dimensional solvent, but directly, by changing protein conformation and function, and indirectly, by changes in diffusional properties of the membrane through changes in chemical composition. The utility of model membrane systems in chemical sensing is predicated upon housing transmembrane proteins in their active conformation(s). Therefore, an understanding of the role the supporting surface has on mimicking the physical properties of plasma membranes is necessary in the creation of biomimetic films that maintain the functional properties of the imbedded proteins.

Measuring diffusional motions via time-resolved picosecond laser spectroscopies and fluorescence microscopies, the fluidity and interfacial adhesion strength at an organic/inorganic interface of both monolayer thin films and supported lipid bilayers has been examined. Films have been prepared using both Langmuir-Blodgett deposition and small unilamellar vesicle (SUV) deposition. Both physical and chemical interactions were found to play an important role in mediating the dynamical properties exhibited by these films. First, the addition of an aqueous adlayer to lipid films produced using SUV deposition was found to significantly disrupt the organizational order within the alkyl chain region. Second, by combining rotational and translational diffusion measurements from a tethered fluorescent probe molecule, compositional variations within alkylphosphonic acid Langmuir films induced varying degrees of adhesion and

fluidity. Lastly, the extent to which the fluidity of a supported lipid film is mediated by the ionic interactions between head-group and supporting surface vs. that of the lipid-lipid tail-group interactions was examined and shown to be system dependent.

This research has led to an adaptable methodology based on the use of rotational and translational diffusional data to quantitate the strength of supported films over a range of length scales (sub-diffraction limit – to – hundreds of microns). A novel family of interfaces that can be physically bound to a surface and at the same time have controlled fluidity depending upon a range of chemical conditions of the underlying inorganic support has been developed. These developments move closer to providing an understanding of the impact a supporting surface plays in mediating model membrane dynamical properties and function.

To Mom, Dad, Kathy, and Ronny.

ACKNOWLEDGMENTS

I would like to sincerely thank everyone who has contributed to my personal and professional development over the past few years. First and foremost, I would like to thank my research advisor Professor Gary J. Blanchard. I am thankful for the freedom you gave me to pursue different projects, and the many helpful suggestions when they failed. Without your mentorship, I would not be the scientist I am today.

I also want to express my gratitude to my committee members: Professors Tom Hamann, Jim McCusker, and Greg Swain for their guidance and insightful suggestions. Thanks to Dr. Kathy Severin, and Professors Merlin Bruening and Greg Swain for their mentorship in teaching the many semesters of the analytical and physical chemistry lab sequence. I am thankful to the Michigan State University Chemistry Department, and United States Department of Education (GAANN Fellowship) for funding this project and allowing me to perform this research.

Many thanks to my colleagues and lab mates for the fun times inside and outside of lab. I would like to specifically thank Dr. Omid Zandi and Josh Baillargeon for their friendship, camaraderie, and enjoyment from countless hours of fruitful science discussions at the local watering holes. I would also like to thank past and present Blanchard group members for truly making graduate school a wonderful experience.

I could not be more thankful for the constant support from my parents, brother, family and friends. Specifically, I would like to thank my parents for their love, devotion and unwavering support throughout my education. Finally, I would like to thank Emily. Thank you for your continued optimism, putting up with my long hours at work, support and encouragement. I am truly grateful and look forward to many future adventures.

TABLE OF CONTENTS

LIST OF TABLES

LIST OF FIGURES

CHAPTER 1: INTRODUCTION

1.1 Motivation

Since the introduction of the fluid mosaic model, the primary role of lipids has been thought to be that of a barrier to the outside world; compartmentalizing cell functions by providing a two-dimensional solvent for the myriad of proteins performing various tasks.[1] Continued research suggests that lipids play a much more important role. The plasma membrane plays an important role in cellular processes both directly, by mediating protein conformation and function, and indirectly, via changes in diffusional properties of the membrane.[2-3] The study of transmembrane processes at the molecular level, such as transport of ions and molecules, cell signaling and adhesion, have relied upon the formation of cell membrane model systems such as supported lipid monolayers and bilayers (SLBs) and black lipid membranes.[4] While these model systems create a biomimetic environment for the study of cellular structure-function relationships, examination of a means to control the dynamical properties of such systems has been limited. The aim of this dissertation is to better understand ways to characterize and control the dynamical properties of the supported films, with the long-term goal of utilizing this knowledge to create and control the functional properties of a biomimetic bilayer structure.

1.2 Lipid Bilayer Membranes

Membranes are ubiquitous in all living things and are a complex barrier to the outside world. The membrane not only serves as a means to protect a cell from the external environment, but is the critical interface at which chemical transport is regulated and cellular signal transmission occurs. At the most basic level, plasma membranes consist of a bilayer of amphiphilic biomolecules consisting of lipids (phospholipids and cholesterol), biopolymers (peptides and proteins), and carbohydrates.

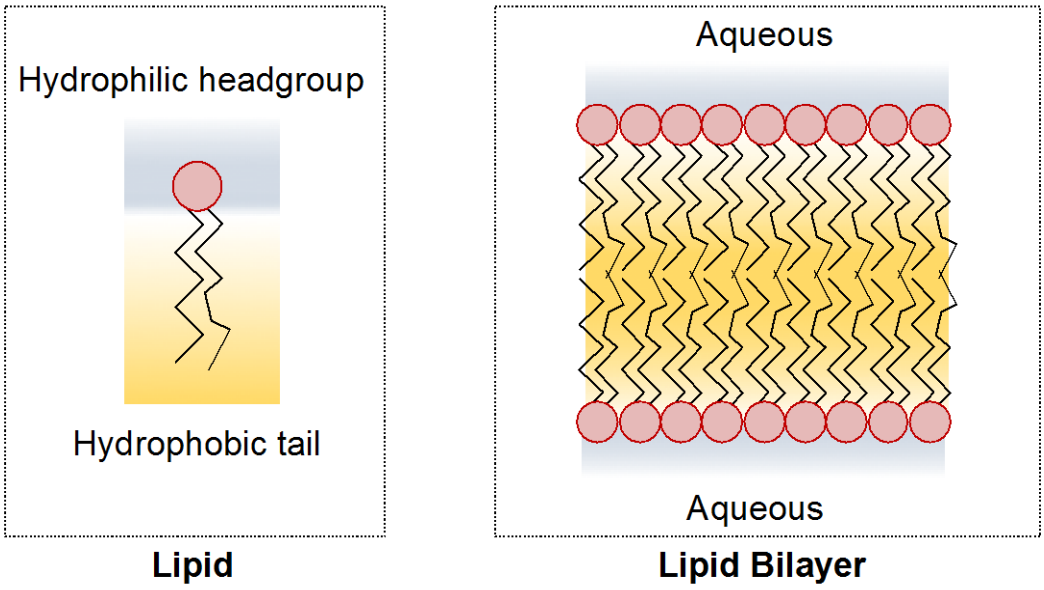

Figure 1-1: The amphiphilic nature of a lipid molecule is shown as a combination of the hydrophilic headgroup and hydrophobic tail (left). The amphiphilic nature of lipids gives rise to the self-assembly of lipid bilayers in the presence of an aqueous environment (right).

Lipids are amphiphilic molecules containing both a hydrophilic region (headgroup) and hydrophobic region (tail) (Fig. 1-1). In the presence of water, the amphiphilic nature of the phospholipid results in their self-assembly into a bilayer structure with the headgroup in contact with water, and the tails facing each other.

Native plasma membranes consist of thousands of unique chemical species, with over 500 unique lipids in the human plasma membrane alone.[5] Lipids are commonly sorted by both their headgroup type, and tail length and degree of saturation. The five most common lipid headgroups are shown in figure 1-2. The different headgroups are a result of the esterification of a single oxygen on the phosphonic acid group attached to the phospholipid (Fig. 1-2, a.). The headgroup is important in defining both the overall charge at the lipid-water interface as well as contributing to lipid-lipid interactions through electrostatic interactions or hydrogen bonding. For example, at pH = 7, headgroups containing hydroxyl groups, with the exception of phosphatidylserine, will

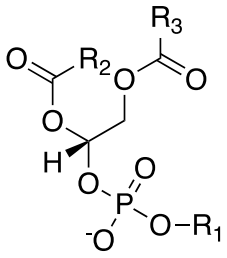

Figure 1-2: Molecular structure for a typical lipid is shown in (a.) Both R_2 and R_3 consist of alkyl chains of varying lengths and degrees of saturation. R_1 corresponds to the esterified side group giving the lipid a unique charge at different pH values, commonly named (b.) phosphatidic acid, (c.) phosphatidylglycerol, (d.) phosphatidylinositol, (e.) phosphatidylserine, (f.) phosphatidylethanolamine, and (g.) phosphatidylcholine.

add zero charge to the lipid headgroup, giving a net (-1) charge to the lipid. In comparison, both ethanolamine and choline contribute a (+1) charge to the headgroup, giving the lipid zwitterionic character or a net neutral charge.[6]

Over the life of a typical cell, diverse and dynamic chemical compositional and morphological changes occur.[7-8] Steinman, et. al. have shown that the plasma membrane experiences a complete turnover or recycling of lipids over the course of an hour.[9] As a result of the constant turnover of lipids, the formation of membrane patches or domains occurs lasting tens of seconds, but disperse soon after.[10] Developing a biomimetic platform, whether for the study of transmembrane processes or utilization as a biosensor, that maintains the fully functional form of the proteins without the full morphological and compositional complexity of the native environment, remains a challenge.

1.3 Model Membrane Systems

There are many different types of model membrane systems, but are commonly grouped as either supported or unsupported model membrane systems. Below, a brief review of a few

relevant methods for preparing model membrane systems, their limitations and applications, with the focus on solid supported membranes is examined.

Unsupported Lipid Membranes. Unsupported lipid membranes are relatively easy to fabricate and maintain similar dynamic properties to native plasma membranes. The preservation of the natural properties of plasma membranes in unsupported lipid bilayers allows for the embedding of transmembrane proteins that maintain their functional form. Unsupported lipid membranes are limited in their stability (typically hours), availability of analytical techniques to characterize their properties, and need for a solid support to act as a transducer for many bio-technological applications (biosensors, separations, self-healing and tribological surfaces).[11]

Black Lipid Membranes (BLMs). Early work on the formation and examination of lipid membrane models involved using a Langmuir trough to self-assemble lipids at the air-water interface and transfer to a small aperture (typically < 1mm diameter) contained on a thin film of Teflon.[12-13] The membranes were termed "black" due to the observation that under reflected light, the birefringent quality of the pinhole region became non-reflecting over time.[14] Fabrication of BLMs leaves both outer in inner leaflets available to interrogation. As a result of the easy access to both interfaces, BLMs have found wide use in the investigation of ion-channel activity and membrane permeability studies.[15] Despite recent efforts to decrease the aperture size to sub-micrometer diameters for increased structural robustness, these systems have yet to exhibit long-term stability.[16-18]

Liposomes (Lipid Vesicles). Liposomes are spherically structured lipid bilayers containing an internal volume of an aqueous phase and are typically classified by their size and degree of lamella.[19-22] Multilamellar vesicles (MLVs) are vesicles containing more than a singular bilayer. Because of their ill-defined geometry, and lack of structural uniformity, MLVs are rarely used for analytical study. MLVs form readily by self-assembly when dried lipids are introduced to an aqueous phase. They are often an observed initial structure in the preparation small unilamellar vesicles (SUVs, diameter < 100 nm), large unilamellar vesicles (LUVs, d > 100 nm), and giant unilamellar vesicles (GUVs, d > 10 μm). Recently, lipid vesicles have been extensively studied and found widespread use as liposomal drug delivery systems.[23] Despite these successes, vesicles remain less than ideal candidates for studying protein-lipid interfaces and for use in biotechnological applications. The curvature induced by formation of the vesicles is much higher compared to the curvature observed in cell membranes, resulting in packing constraints different than the native plasma membrane.[24] Furthermore, polydispersity in vesicle size gives rise to curvature induced differential responses in the physical properties of the lipid-lipid or lipid-protein interface limiting the ability to precisely measure a given property.[25-26]

Supported Lipid Membranes. In the mid-1980s Tamm and McConnell first showed the viability of supporting phospholipid bilayers at a solid interface.[27] The method presents a one-step procedure for creating solid supported model membranes containing different lipid mixtures. Since then, there have been extensive studies on the use of supported lipid bilayers (SLBs) as a tool to understand lipid domain formation, and protein membrane interactions.[28-31] Recent advancements combining both quartz crystal microbalance with dissipation monitoring (QCM-D)

and atomic force microscopy (AFM) have led to an understanding of the mechanisms involved in the formation of these SLB systems.[32-33]

In general, there are two methods commonly used for the formation of SLBs. The first method involves the deposition of small unilamellar vesicles (SUVs) onto the supporting surface. Recent studies have examined the extent to which the composition of the underlying support influences the formation and adhesion of supported lipid bilayers prepared by the fusion deposition of small unilamellar vesicles (SUVs). The identity of the underlying support has a marked effect on both the rupture and spreading processes of the SUVs.[34-38] The second method utilizes the Langmuir-Blodgett or Langmuir-Schaffer technique to prepare monomolecular or multilayer films. [39-41] The use of the Langmuir-Blodgett technique provides a controlled means for the formation of these SLBs in comparison to the SUV approach. Because these films are built one molecular layer at a time, the bilayer can be built asymmetrically, a property of natural membranes that is not accessible using the SUV approach.[42-43]

SLBs can be categorized into two main types based upon the supporting interface. The simplest type consists of a mono- or bilayer on a solid support. Formation of SLBs on a solid support has seen a variety of supporting materials such as silica, glass, mica, various metal oxides such as TiO_2 and $SrTiO_3$, and more recently inorganic nanoparticles.[34-38] The formation of such films is relatively simple and straightforward provided the proper pH and ionic strength during preparation.[44] The second type of supported lipid membrane, commonly referred to as hybrid bilayer membranes (HBMs)[45-47] contain an added organic (self-assembled monolayer) or biological (protein or peptide) cushioning between the supporting surface and lipid layer.[48-50] Often, these HBMs are formed at a metallic interface lending themselves amenable for use as

electrochemical biosensors.[51] Unfortunately, these systems are often plagued with poor stability in air and exhibit slowed dynamical properties relative to native membranes.[30, 52]

1.4 Objectives

Utilizing the formation and adhesion of SUVs, the Blanchard group has shown previously that robust air-stable lipid layers can be formed through the aid of zirconium-phosphate (ZP) chemistry and is dependent upon the lipid head-group used in self-assembly process.[53] The lipid adlayers formed by this approach were found to be structurally complete and nominally homogeneous monolayers. Later studies examined how the underlying metal ion identity mediated the lipid-surface interactions during the formation of the lipid-metal-phosphonate films.[54] The formation of these lipid films through the lipid-metal coordination process was found to rely upon the use of metal ions with high charge and small ionic radius. These studies showed the possibility of the formation of air stable lipid layers, and how variations in the metal ions used changed the permeability and thickness. The dynamical properties of these films were unknown.

Using the foundational work on the formation of supported and air-stable lipid layers, the work in this dissertation has focused on understanding how the physical interactions occurring at the lipid-aqueous, lipid-support, and lipid-lipid interfaces give rise to the observed dynamical properties for a given system. We used Time Correlated Single Photon Counting (TCSPC) Microscopy and Fluorescence Recovery After Photobleaching (FRAP) as measurement techniques to examine the rotational and translational behavior of probe molecules in a variety of supported lipid systems, and provide a detailed description of the measurement science in Chapter 2. In Chapter 3, we first examined the role of an aqueous overlayer on the dynamics of a perylene probe embedded within a covalently bound lipid monolayer using TCSPC and characterized the

permeability of the interface using electrochemical potential and impedance measurements. The combination of the rotational and translational diffusion properties of an alkylphosphonic acid Langmuir film is used to understand the molecular-micro scale heterogeneity, fluidity, and adhesion strength of the film at the supporting interface in Chapter 4. In Chapter 5, using FRAP and x-ray photoelectron spectroscopy (XPS), we examined the role that different alkaline earth and transition metals play in modulating the fluidity of a supported lipid film. The combination of optical techniques comparing different physical properties on different time-scales has opened the possibility to study the complex dynamic properties inherent to both supported lipid membranes and their natural plasma membrane counterpart. The ability to measure these properties allows for both the creation of films with modulated fluidity, and the ability to understand the dynamic conditions necessary to maintain fully functional transmembrane proteins within a model system.

REFERENCES

REFERENCES

1. Singer, S. J.; Nicolson, G. L., The fluid mosaic model of the structure of cell membranes. *Science* **1972,** *175* (4023), 720-31.

2. Engelman, D. M., Membranes are more mosaic than fluid. *Nature* **2005,** *438* (7068), 578-580.

3. Phillips, R.; Ursell, T.; Wiggins, P.; Sens, P., Emerging roles for lipids in shaping membrane-protein function. *Nature* **2009,** *459* (7245), 379-385.

4. Castellana, E. T.; Cremer, P. S., Solid supported lipid bilayers: From biophysical studies to sensor design. *Surface Science Reports* **2006,** *61* (10), 429-444.

5. Quehenberger, O.; Armando, A. M.; Brown, A. H.; Milne, S. B.; Myers, D. S.; Merrill, A. H.; Bandyopadhyay, S.; Jones, K. N.; Kelly, S.; Shaner, R. L.; Sullards, C. M.; Wang, E.; Murphy, R. C.; Barkley, R. M.; Leiker, T. J.; Raetz, C. R. H.; Guan, Z. Q.; Laird, G. M.; Six, D. A.; Russell, D. W.; McDonald, J. G.; Subramaniam, S.; Fahy, E.; Dennis, E. A., Lipidomics reveals a remarkable diversity of lipids in human plasma. *J Lipid Res* **2010,** *51* (11), 3299-3305.

6. Marsh, D., *CRC Handbook of Lipid Bilayers*. CRC Press: Boca Raton, Fla., 1990.

7. van Meer, G.; Voelker, D. R.; Feigenson, G. W., Membrane lipids: where they are and how they behave. *Nat Rev Mol Cell Bio* **2008,** *9* (2), 112-124.

8. Cooper, G. M., *The cell : a molecular approach*. Second edition. ed.; ASM Press ; Sinauer Associates: Washington, D.C.
Sunderland, Mass., 2000; p xxiv, 689 pages.

9. Steinman, R. M.; Mellman, I. S.; Muller, W. A.; Cohn, Z. A., Endocytosis and the Recycling of Plasma-Membrane. *J Cell Biol* **1983,** *96* (1), 1-27.

10. Gheber, L. A.; Edidin, M., A model for membrane patchiness: Lateral diffusion in the presence of barriers and vesicle traffic. *Biophys J* **1999,** *77* (6), 3163-3175.

11. Gugliuzza, A., *Smart Membranes and Sensors Synthesis, Characterization, and Applications*. John Wiley & Sons Inc: Hoboken, NJ, 2014.

12. Montal, M.; Mueller, P., Formation of bimolecular membranes from lipid monolayers and a study of their electrical properties. *Proc Natl Acad Sci U S A* **1972,** *69* (12), 3561-6.

13. Mueller, P.; Rudin, D. O.; Tien, H. T.; Wescott, W. C., Reconstitution of cell membrane structure in vitro and its transformation into an excitable system. *Nature* **1962,** *194*, 979-80.

14. Mueller, P.; Wescott, W. C.; Rudin, D. O.; Tien, H. T., Methods for Formation of Single Bimolecular Lipid Membranes in Aqueous Solution. *J Phys Chem-Us* **1963,** *67* (2), 534-535.

15. Trojanowicz, M., Miniaturized biochemical sensing devices based on planar bilayer lipid membranes. *Fresen J Anal Chem* **2001,** *371* (2), 246-260.

16. Jonsson, P.; Jonsson, M. P.; Hook, F., Sealing of Submicrometer Wells by a Shear-Driven Lipid Bilayer. *Nano Lett* **2010,** *10* (5), 1900-1906.

17. Heinemann, F.; Schwille, P., Preparation of Micrometer-Sized Free-Standing Membranes. *Chemphyschem* **2011,** *12* (14), 2568-2571.

18. Kitta, M.; Tanaka, H.; Kawai, T., Rapid fabrication of Teflon micropores for artificial lipid bilayer formation. *Biosens Bioelectron* **2009,** *25* (4), 931-934.

19. Hope, M. J.; Bally, M. B.; Mayer, L. D.; Janoff, A. S.; Cullis, P. R., Generation of Multilamellar and Unilamellar Phospholipid-Vesicles. *Chemistry and Physics of Lipids* **1986,** *40* (2-4), 89-107.

20. Hope, M. J.; Bally, M. B.; Webb, G.; Cullis, P. R., Production of Large Unilamellar Vesicles by a Rapid Extrusion Procedure - Characterization of Size Distribution, Trapped Volume and Ability to Maintain a Membrane-Potential. *Biochimica Et Biophysica Acta* **1985,** *812* (1), 55-65.

21. Mayer, L. D.; Bally, M. B.; Hope, M. J.; Cullis, P. R., Techniques for Encapsulating Bioactive Agents into Liposomes. *Chemistry and Physics of Lipids* **1986,** *40* (2-4), 333-345.

22. Mayer, L. D.; Hope, M. J.; Cullis, P. R., Vesicles of Variable Sizes Produced by a Rapid Extrusion Procedure. *Biochimica Et Biophysica Acta* **1986,** *858* (1), 161-168.

23. Samad, A.; Sultana, Y.; Aqil, M., Liposomal drug delivery systems: an update review. *Curr Drug Deliv* **2007,** *4* (4), 297-305.

24. Cornell, B. A.; Middlehurst, J.; Separovic, F., The Molecular Packing and Stability within Highly Curved Phospholipid-Bilayers. *Biochimica Et Biophysica Acta* **1980,** *598* (2), 405-410.

25. Hatzakis, N. S.; Bhatia, V. K.; Larsen, J.; Madsen, K. L.; Bolinger, P. Y.; Kunding, A. H.; Castillo, J.; Gether, U.; Hedegard, P.; Stamou, D., How curved membranes recruit amphipathic helices and protein anchoring motifs. *Nat Chem Biol* **2009,** *5* (11), 835-841.

26. Kunding, A. H.; Mortensen, M. W.; Christensen, S. M.; Stamou, D., A fluorescence-based technique to construct size distributions from single-object measurements: Application to the extrusion of lipid vesicles. *Biophys J* **2008,** *95* (3), 1176-1188.

27. Tamm, L. K.; Mcconnell, H. M., Supported Phospholipid-Bilayers. *Biophys J* **1985,** *47* (1), 105-113.

28. Dietrich, C.; Volovyk, Z. N.; Levi, M.; Thompson, N. L.; Jacobson, K., Partitioning of Thy-1, GM1, and cross-linked phospholipid analogs into lipid rafts reconstituted in supported model membrane monolayers. *P Natl Acad Sci USA* **2001,** *98* (19), 10642-10647.

29. Leonenko, Z. V.; Finot, E.; Ma, H.; Dahms, T. E. S.; Cramb, D. T., Investigation of temperature-induced phase transitions in DOPC and DPPC phospholipid bilayers using temperature-controlled scanning force microscopy. *Biophys J* **2004,** *86* (6), 3783-3793.

30. Anderson, N. A.; Richter, L. J.; Stephenson, J. C.; Briggman, K. A., Determination of lipid phase transition temperatures in hybrid bilayer membranes. *Langmuir* **2006,** *22* (20), 8333-8336.

31. Levy, D.; Briggman, K. A., Cholesterol/phospholipid interactions in hybrid bilayer membranes. *Langmuir* **2007,** *23* (13), 7155-7161.

32. Richter, R. P.; Berat, R.; Brisson, A. R., Formation of solid-supported lipid bilayers: An integrated view. *Langmuir* **2006,** *22* (8), 3497-3505.

33. Cremer, P. S.; Boxer, S. G., Formation and spreading of lipid bilayers on planar glass supports. *J Phys Chem B* **1999,** *103* (13), 2554-2559.

34. Richter, R. P.; Bérat, R.; Brisson, A. R., Formation of solid-supported lipid bilayers: An integrated view *Langmuir* **2006,** *22*, 3497-3505.

35. Beneš, M.; Billy, D.; Benda, A.; Speijer, H.; Hof, M.; Hermans, W. T., Surface-dependent transitions during self-assembly of phospholipid membranes on mica, silica, and glass. *Langmuir* **2004,** *20*, 10129-10137.

36. Starr, T. E.; Thompson, N. L., Formation and characterization of planar phospholipid bilayers supported on TiO2 and SrTiO3 single crystals. *Langmuir* **2000,** *16*, 10301-10308.

37. Xu, J.; Stevens, M. J.; Oleson, T. A.; Last, J. A.; Sahai, N., Role of Oxide Surface Chemistry and Phospholipid Phase on Adsorption and Self-Assembly: Isotherms and Atomic Force Microscopy. *J. Phys. Chem. C* **2009,** *113*, 2187-2196.

38. Liu, J., Interfacing zwitterionic liposomes with inorganic nanomaterials: Surface forces, membrane integrity, and applications. *Langmuir* **2016,** *32*, 4393-4404.

39. Blodgett, K. B., Films built by depositing successive monomolecular layers on a solid. *J. Am. Chem. Soc.* **1935,** *57* (6), 1007-1022.

40. Langmuir, I., The adsorption of gases on plane surfaces of glass, mica and platinum. *J. Am. Chem. Soc.* **1918,** *40* (9), 1361-1403.

41. Langmuir, I.; Schaefer, V. J., Salted-out protein films. *J Am Chem Soc* **1938,** *60*, 2803-2810.

42. Crane, J. M.; Kiessling, V.; Tamm, L. K., Measuring lipid asymmetry in planar supported bilayers by fluorescence interference contrast microscopy. *Langmuir* **2005,** *21* (4), 1377-1388.

43. Kiessling, V.; Wan, C.; Tamm, L. K., Domain coupling in asymmetric lipid bilayers. *Bba-Biomembranes* **2009,** *1788* (1), 64-71.

44. Cho, N.-J.; Jackman, J. A.; Liu, M.; Frank, C. W., pH-Driven Assembly of Various Supported Lipid Platforms: A Comparative Study on Silicon Oxide and Titanium Oxide. *Langmuir* **2011,** *27* (7), 3739-3748.

45. Plant, A. L., Self-Assembled Phospholipid Alkanethiol Biomimetic Bilayers on Gold. *Langmuir* **1993,** *9* (11), 2764-2767.

46. Plant, A. L., Supported hybrid bilayer membranes as rugged cell membrane mimics. *Langmuir* **1999,** *15* (15), 5128-5135.

47. Plant, A. L.; Tarlov, M., Self-Assembled Monolayers as Substrates for Planar Model Membranes. *Biophys J* **1993,** *64* (2), A298-A298.

48. Albertorio, F.; Diaz, A. J.; Yang, T. L.; Chapa, V. A.; Kataoka, S.; Castellana, E. T.; Cremer, P. S., Fluid and air-stable lipopolymer membranes for biosensor applications. *Langmuir* **2005,** *21* (16), 7476-7482.

49. Matyszewska, D.; Bilewicz, R.; Su, Z. F.; Abbasi, F.; Leitch, J. J.; Lipkowski, J., PM-IRRAS Studies of DMPC Bilayers Supported on Au(111) Electrodes Modified with Hydrophilic Monolayers of Thioglucose. *Langmuir* **2016,** *32* (7), 1791-1798.

50. Hubbard, J. B.; Silin, V.; Plant, A. L., Self assembly driven by hydrophobic interactions at alkanethiol monolayers: mechanism of formation of hybrid bilayer membranes. *Biophys Chem* **1998,** *75* (3), 163-176.

51. Steinem, C.; Janshoff, A.; Galla, H. J.; Sieber, M., Impedance analysis of ion transport through gramicidin channels incorporated in solid supported lipid bilayers. *Bioelectroch Bioener* **1997,** *42* (2), 213-220.

52. Anderson, N. A.; Richter, L. J.; Stephenson, J. C.; Briggman, K. A., Characterization and control of lipid layer fluidity in hybrid bilayer membranes. *J Am Chem Soc* **2007,** *129* (7), 2094-2100.

53. Oberts, B. P.; Blanchard, G. J., Headgroup-Dependent Lipid Self-Assembly on Zirconium Phosphate-Terminated Interfaces. *Langmuir* **2009,** *25* (24), 13918-13925.

54. Oberts, B. P.; Blanchard, G. J., Ionic Binding of Phospholipids to Interfaces: Dependence on Metal Ion Identity. *Langmuir* **2009,** *25* (22), 13025-13033.

CHAPTER 2: EXPERIMENTAL TECHNIQUES

2.1 Instrumental Methods for the Examination of Lipid Dynamics

The organization of lipids within a bilayer structure creates a dynamic environment on a variety of length and timescales. The dynamic properties of the membrane are determined by each lipid component contributing unique conformational, translational, and molecular rotation dynamics within the membrane as a whole. In addition, the possibility of collective motions of the entire membrane or individual subgroups can exist. For example, the dynamics of lipids exhibit vastly different conformational, translation, and rotation dynamics in comparison to their protein and peptide counterparts. The examination of even simple model lipid membranes remains a challenge because the unique dynamical properties cannot be simply probed by a single physical parameter. While not an exhaustive list, a variety of magnetic, optical, acoustic and scanning probe methods exist for the examination of different membrane properties. The utility and limitations of the most common and widely used methods for study of membrane dynamics will be discussed briefly below.

Magnetic Resonance Methods. Both electron paramagnetic resonance (EPR) and nuclear magnetic resonance (NMR) have been used to examine a variety of dynamical properties of membranes. Typically, these techniques are used to examine the conformational order of the lipid alkyl chain region based on spectrum splitting of a site-directed spin label (EPR) or quadrupole splitting of deuterated lipid molecules (NMR).[1-2] The use of site-directed spin labeling (SDSL), a now common EPR technique, has proved useful to examine the lipid-protein interface because the sensitivity of the measurement technique is matched to the rotational dynamics of lipids (nanoseconds).[3-4] Using deuterium labeled lipid alkyl chains of specific lipid types, researchers have been successfully using ^{2}H solid state NMR to examine gauche defects and ordering of the

tail region at the lipid-lipid and lipid-protein interface.[5-6] While both techniques provide information on the molecular details of the tail orientation and order, they are limited by a variety of factors. The measurements are an average response from the model under study, so detection of heterogeneity on a scale larger than the molecular scale is difficult.

Optical Spectroscopy Methods. Linear and non-linear optical spectroscopy techniques have been successfully used to examine a variety of dynamical properties of lipid membranes. Similar to EPR and NMR methods, different forms of IR spectroscopy have been employed to examine the structural order of the long lipid alkyl chain groups in the bilayer. Polarization modulation infrared reflection absorption spectroscopy (PM-IRRAS) is commonly coupled to a Langmuir trough allowing for the study of changes in conformation of both lipid alkyl chain and headgroups of a single monolayer at the air-water interface.[7-8] Nonlinear methods such as second harmonic generation (SHG) and sum frequency generation (SFG) have been successfully used to examine the dynamics of lipid diffusion perpendicular to the bilayer plane (lipid flip-flop or translocation) as well as changes in the conformational order of the lipid tail groups.[9-13] The most commonly employed methods for the study of translational and rotational diffusion in membranes are time resolved fluorescence techniques. Fluorescence correlation spectroscopy (FCS) has been in use since the early 1970s to examine chemical rate constants and diffusion coefficients of biomolecules in solution, however it was not until the mid-1990s that the technique overcame previous limitations of large background signals and low signal count rates.[14-17] The low concentrations of chromophores necessary for the technique are beneficial due to decreased morphological disruption of the model system. Unfortunately, FCS is also limited by the need for

low concentrations in that the inherent heterogeneity can provide poor precision in observed values or go unobserved altogether.[18]

Scanning Probe and Acoustic Methods. Both quartz crystal microbalance with dissipation monitoring (QCM-D) and atomic force microscopy (AFM) have contributed greatly to the understanding of the mechanism by which SUVs adhere and form stable supported bilayer systems.[19-22] Both methods provide unique insight into the fluid-like properties of model cell membranes, however they are limited in their ability to spatially resolve large-scale (100 μm – to – cm) heterogeneities within the supported lipid bilayers. QCM-D measures the average response from changes in frequency and dissipation energy over the size of the sample, typically 1-2 cm diameter disk, and therefore has very limited spatial resolution. The spatial resolution of AFM is unparalleled relative to the other techniques discussed within this dissertation, however the total observed area makes observations of macroscale compositional changes difficult.

2.2 Evaluating Film Morphology with Brewster Angle Microscopy (BAM)

Analytical methods for the direct observation of large scale (μm-to-cm) morphological features are often limited to the use of dyes or stains and an optical microscope. During preparation of Langmuir-Blodgett films, the addition of dyes or stains could potentially disrupt the morphological features of a monolayer film, even at relatively low concentrations. Additionally, the resolution is often limited by the depth of focus of the microscope objective at a given magnification. Brewster Angle Microscopy (BAM) was first introduced in 1991 and is currently the most informative method for the examination of relatively largescale (μm-to-cm) changes to Langmuir films under a variety of conditions.[23]

Sir David Brewster first observed when "a pencil of light is incident upon the separating surface of two media having different indices of refraction m m', it will be polarised at an angle whose tangent is equal to the quotient of the greater index of refraction divided by the lesser, or m/m'."[24] This observation is now commonly known as Brewster's law (eqn. 2-1), where θ_B is Brewster's angle, or the angle at which maximum polarization occurs, n_1 and n_2 are the indices of refraction of the two materials.

$$\tan\theta_B = \frac{n_1}{n_2} \qquad 2\text{-}1$$

While Brewster's observations were based on the refraction (transmission) of light through two optically dissimilar materials, BAM measures the presence of polarized reflected light (Fig 2-1.) For the measurement of an organic film at an air-water interface where the supporting surface is water ($n_2 \approx 1.33$) and the absence of film is air ($n_1 \approx 1.00$), the angle of incidence is set to Brewster's angle (53°), and no reflection occurs. Application of an organic film at the interface ($n \approx 1.5$), changes the ratio between the refractive indices of the air-water interface and reflection occurs.

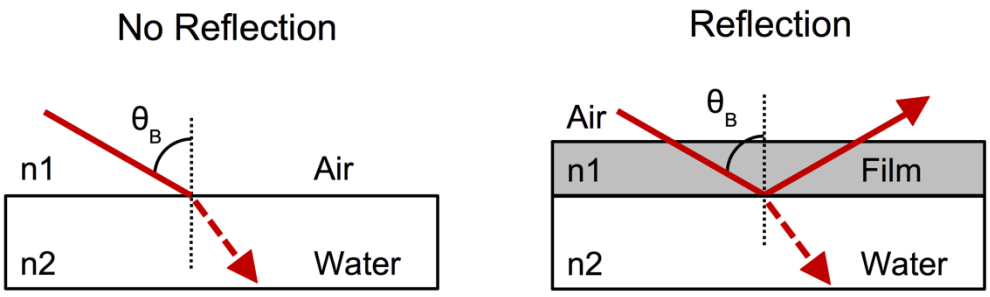

Figure 2-1: Description of the application of Brewster's law for the visualization of the formation dynamics of Langmuir monolayers at an air/water interface.

Because the incident radiation is polarized, observed contrast in the image does not necessarily imply differences in refractive indices between materials. The observed contrast could be due to changes in the reflected polarization ellipticity induced by the material at the interface as described by Fresnel.[25]

BAM Instrumentation. The instrumentation used for the collection of BAM images is comprised of a diode laser, a microscope objective, and CCD camera (Fig. 2-2). Since the refractive index for a given medium changes as a function of wavelength, the BAM relies on a 50 mW single wavelength diode laser (658 nm). The angle of incidence can be changed between 52-

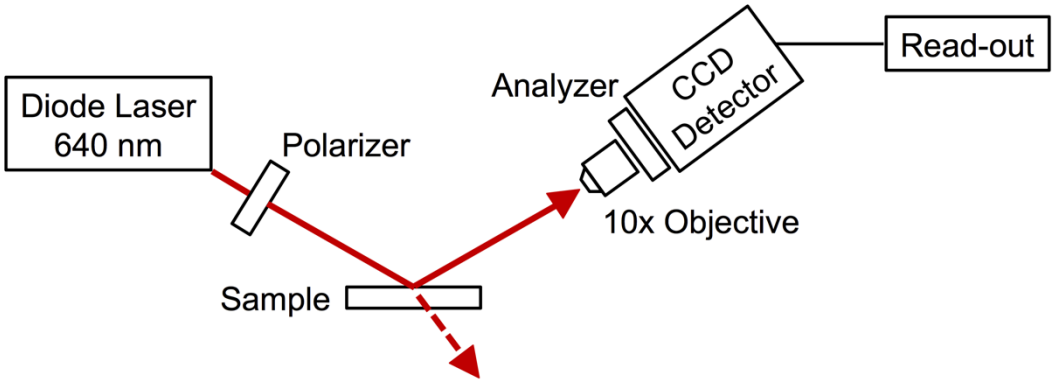

Figure 2-2: Schematic of the Brewster Angle Microscope (BAM) system.

57° with a resolution of 0.001° allowing a variety of interfaces to be examined. The polarizer is a motorized Glan-Thompson prism with a polarizing resolution of 0.001°. The motorized polarizer ensures an orthoganol plane of incidence relative to the sample surface thereby minimizing background reflection and increasing observed contrast. The detection optics are comprised of a 10x microscope objective (Olympus, LMPLANFl), analyzer and CCD camera. The microscope objective allows for a 720x400 μm field of view with an angular resolution (θ) based on the

Rayleigh criterion (eqn. 2-2), where λ is the wavelength of light (658 nm) and D is the diameter of the aperture.[26-27]

$$\theta = 1.220\frac{\lambda}{D}$$
$$\Delta l = 0.61\frac{\lambda}{NA} \qquad 2\text{-}2$$

By multiplying the radial resolution (θ) by the distance from the object being resolved, the effective lateral resolution can be described by eqn. 2-2, where NA is the numerical aperture of the objective (0.25), giving an approximate spatial resolving power of *ca.* 1.6 μm. The motorized analyzer has a resolution of 0.001° and allows for the correction of induced ellipticity of the initially p-polarized beam from reflection of the film surface. Finally, the CCD camera provides an image with 1360x1024 px resolution at a frame rate of 20-35 fps.

2.3 Measuring Diffusion: Time-Resolved Fluorescence Spectroscopy

There are a variety of spectroscopic techniques currently used to measure the diffusional properties of both intact cellular membranes and supported bilayer systems. The most widely employed methods rely on the use of a fluorescent probe molecule. In this section, information on the fluorescence microscopy techniques used to examine the diffusion behavior of a chromophore in a model cell membrane is provided. A brief explanation of the theory behind both the rotational and translational diffusion measurement techniques is described. The associated instrumental design and analysis of the observed data is described in detail.

Rotational Diffusion using Fluorescence Anisotropy Decay Imaging (FADI). The measurement of steady-state and, specifically, time resolved anisotropy offers the possibility to study the chemical processes that affect molecular scale reorientation behavior. The process for

measuring fluorescence anisotropy relies on photoselective excitation of the chromophores by polarized light. Photoselective excitation is the preferential excitation of chromophores with transition moments (electronic dipole) aligned parallel to the electric vectors of the exciting photons. The transition moment of a chromophore occurs at a defined orientation with respect to the molecular axis coordinate system. In a fully isotropic solution the transition moments of the chromophores are oriented randomly. Upon excitation, only the chromophores with absorption transition moments in the same plane as the polarization of the incoming light are excited. Emission of light also occurs at a polarization that is fixed relative to the molecular coordinate system. By measuring the intensity of fluorescence transients both parallel $I_{||}(t)$ and perpendicular $I_{\perp}(t)$ to the initial excitation polarization over time, the anisotropy of the chromophore can be measured (eqn. 2-3). The relative angle between the absorption transition moment and emission moment determines the maximum anisotropy (r_0).

$$R(t) = \frac{I_{||}(t) - I_{\perp}(t)}{I_{||}(t) + 2I_{\perp}(t)} \qquad 2\text{-}3$$

There are a variety of physical phenomena that can contribute to an observed anisotropy decay. The most common causes for an observed anisotropy decay are due to rotational diffusion and resonant energy transfer.[28-34] Because of the sensitivity of the FADI instrument, and the low concentration of chromophore used, the anisotropy decay signal is dominated by the rotational diffusion of the fluorescent probe molecule. Measuring the change in anisotropy from the time of the absorption event to the time of the chromophore emission event provides information on the average relative angular displacement of the fluorescent probes. In typical fluids, over the timespan of 50-100 ps, most chromophore ensembles have exhibited rotational motion and the population of the excited chromophores is closer to being randomized relative to the time of initial excitation. The anisotropy decay time (τ_{OR}) is inversely related to the diffusion constant (D).

Randomization due to rotational diffusion by Brownian motion, is dependent on the temperature (T), viscosity (η), and volume (V) of the rotating molecule and described by the Debye-Stokes-Einstein (DSE) equation (eqn. 2-4).[35-40] The model was originally derived for spherical molecules in a homogenous continuum solvent system. The addition of an adjustment for the shape factor of a nonspherical molecule (S), and the consideration of frictional interactions between solvent and solute (f) brings the DSE model into good agreement with experimental observations for a reasonably broad range of experimental systems.[41-43]

$$\tau_{OR} = \frac{1}{6D} = \frac{\eta V f}{k_B T S} \qquad 2\text{-}4$$

The functional form of the anisotropy decay is dependent upon the specific type of fluorophore under investigation. Below, we describe expected functional forms for an ellipsoidal rotor free to rotate about all axes, then discuss the case of a tethered rotor with rotation limited about two axes.

For a free rotor in solution, the anisotropy decay function R(t) can contain up to five exponential decays, but for most systems, 1-2 decays are observed.[29] By referencing a molecules' Cartesian coordinate system, Chuang and Eisenthal have related R(t) to the Cartesian components of the rotational diffusion constant (D_x,D_y,D_z).[29] The rotational diffusion constants are based on the rotation of an ellipse where rotation about the major axis (prolate spheroid) is defined by $D_x > D_y = D_z$ and rotation about the minor axis (oblate spheroid) is defined by $D_z > D_x = D_y$. By defining the conjugated fluorophore π-system as the x-y plane, and the absorption transition moment as the x-axis, a transition from the ground to first excited singlet state ($S_0 \rightarrow S_1$) yields excitation and emission transition moments nominally parallel to one another. By modeling the molecule as an ellipsoid and defining the Cartesian coordinates in the previously described manner, the anisotropy decay function can be described by eqns. 2-5 and 2-6.[29]

$$R(t) = 0.1e^{(-(2D_x+4D_z)t)} + 0.3e^{(-6D_z t)} \quad \text{(oblate)} \tag{2-5}$$

$$R(t) = 0.4e^{(-6D_z t)} \quad \text{(prolate)} \tag{2-6}$$

For cases when diffusional motion of the rotor is limited about less than the three independent axis, the rotor is said to be hindered, and the hindered rotor model applies. The model is most commonly used for systems in which the fluorescent probe is chemically bound to either the headgroup or alkyl chain of the lipid molecule. The anisotropy decay function for the hindered rotor model is described by eqn. 2-7.[28, 44]

$$R(t) = R(\infty) + (R(0) - R(\infty))exp(^{-t}/_{\tau_{HR}}) \tag{2-7}$$

In this formalism, the rotor movement is constrained to move within a cone of confinement with a semi-angle defined as θ_0. The rotation of the chromophore about the tethering bond within the cone gives the probe a characteristic wobbling diffusion constant (D_W). The relationship between the anisotropy decay time (τ_{HR}), the wobbling diffusion constant and cone angle is given by eqn. 2-8.

$$\tau_{HR} = \frac{7\theta_0^2}{24D_W} \tag{2-8}$$

The cone angle (θ_0) can be determined from the infinite-time anisotropy $R(\infty)$ and zero-time anisotropy $R(0)$ according to eqn. 2-9.[44]

$$\frac{R(\infty)}{R(0)} = \left\langle P_2\left(cos\theta\right)\right\rangle^2 = \left[\frac{1}{2}cos\theta_0\left(1+cos\theta_0\right)\right]^2 \tag{2-9}$$

Fluorescence depolarization is an interaction that is described by the second-order Legendre polynomial. For any condition where the angle θ_0 is zero, the interaction vanishes eqn. 2-10.[45]

$$P_2\left(cos\theta\right) = 0 \tag{2-10}$$

The so called “magic angle” corresponding to this relationship for linear spectroscopy is therefore defined as 54.7°. For fluorescence depolarization measurements, observation of a cone angle with a value of the magic angle, therefore corresponds to complete randomization of the chromophore about the tethered bond.

FADI Instrumentation. The instrument used to acquire fluorescence anisotropy decay images (FADI) is based on the combination of a time correlated single photon counting (TCSPC) laser system coupled to an inverted confocal laser scanning microscope (CLSM) (Nikon Eclipse Ti-U), shown in Fig. 2-3. The light source for this instrument is a synchronously pumped cavity dumped dye laser (Coherent 702) excited by the output of a passively mode locked Nd:YVO_4 laser (Spectra Physics Vanguard). The laser produces both 355 nm and 532 nm light with 13 ps pulses at a repetition rate of 80 MHz and 2.5 W average power. The mode locked laser pumps a pair of dye lasers synchronously which can be tuned from 430 nm to 850 nm. The dye lasers are cavity dumped to control the repetition rate. The output of the dye laser is characterized by a repetition rate of 80 kHz – 80 MHz and ~ 5 ps pulses at an average power at the sample of less than 0.5 mW. For the work presented in this dissertation, the dye laser output is tuned to the excitation maximum of the chromophore in use. The pulsed excitation light is then passed through a polarizer selected to an angle of 0 degrees, next through a set of high-pass filters, and finally into the CLSM.

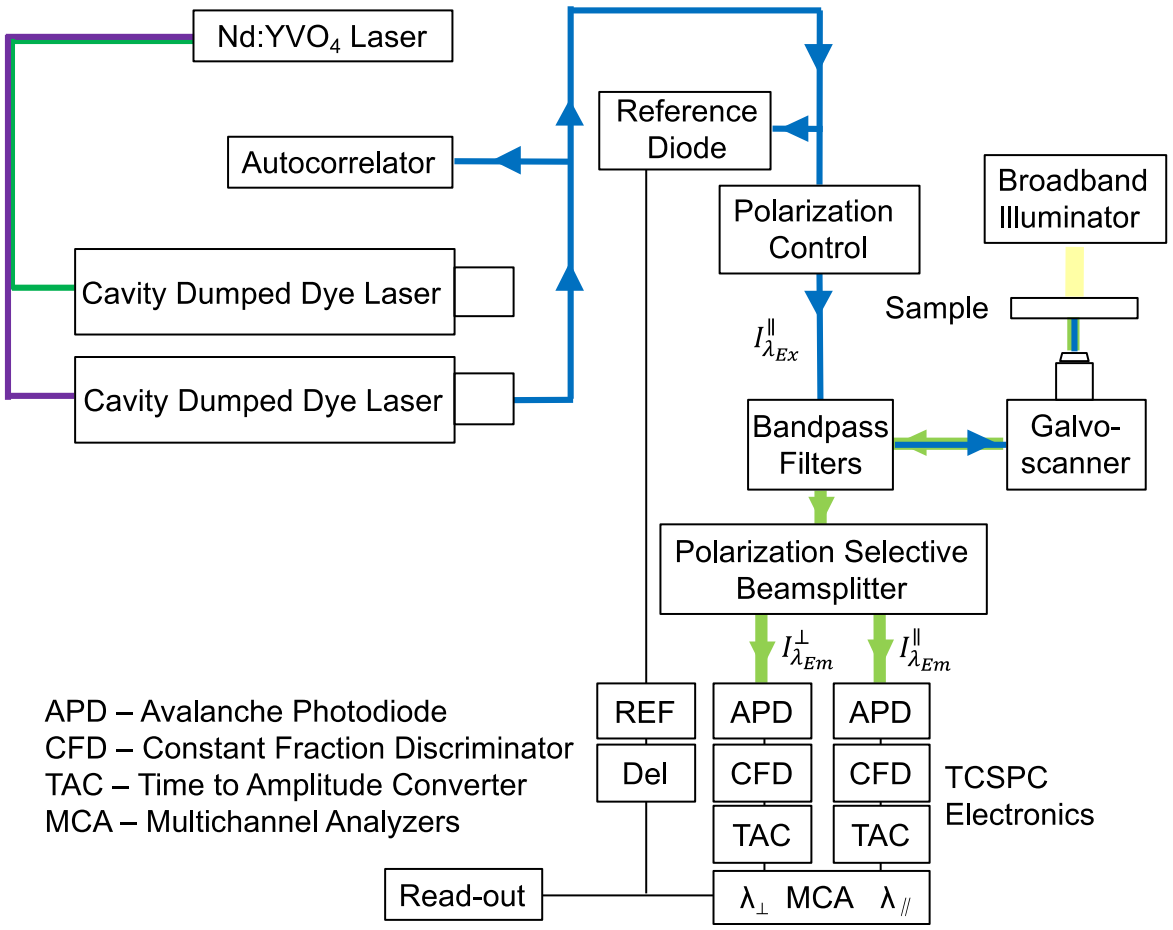

Figure 2-3: Schematic for the Fluorescence Anisotropy Decay Imaging (FADI) instrument.

The CLSM combines high resolution optical imaging with depth selectivity. The CSLM is based on a typical optical microscope, which uses a laser source instead of the often used broadband lamp. The laser is focused on the sample, and the image is acquired pixel-by-pixel by collecting the emitted photons. Detection of time-resolved data is achieved with a polarized dual channel confocal scanning instrument (Becker & Hickl DCS-120) attached to an output port of the microscope and controlled by a galvo-drive unit (Becker & Hickl GDA-120). The confocal scanner is equipped with a polarizing beam splitter and two avalanche photodiode detectors (APD) (ID-Quantique ID100) for the acquisition of fluorescence lifetime and anisotropy decay images.

Polarized fluorescence transients are recorded using time-correlated single photon counting (TCSPC) detection electronics (Becker & Hickl SPC-152, PHD-400N reference diode).

The TCSPC detection electronics are comprised of two constant fraction discriminators (CFD), and electrical delay (DEL), Time-to-Amplitude Converters (TAC), an amplifier between the TAC and the Analogue to digital converter (ADC), and finally to the system memory. The principle of TCSPC is the detection of the arrival time difference between the emission photons from the sample with respect to the reference signal from the source (Fig 2-4).

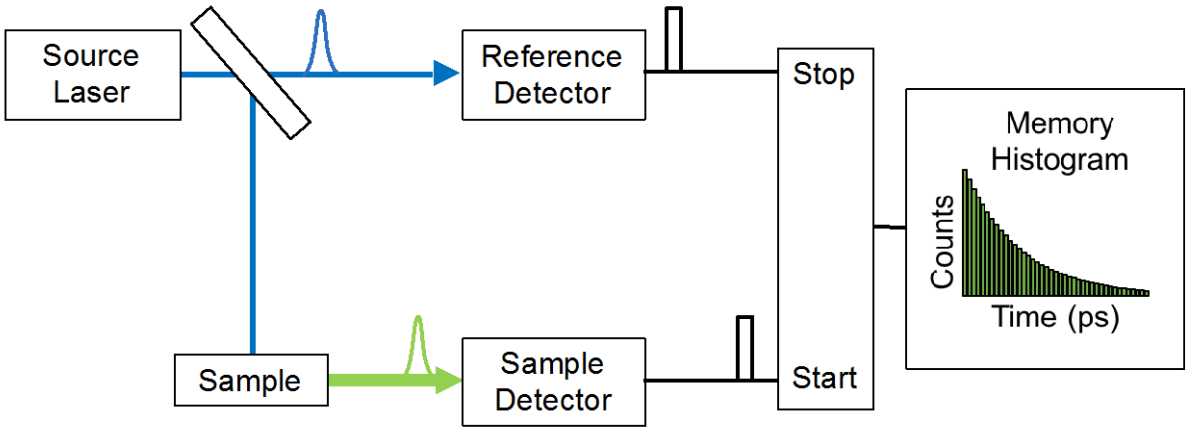

Figure 2-4: Visual representation of the photon counting scheme for time correlated single photon counting (TCSPC)

The system electronics can be compared to a stopwatch, where the time difference between the START signal (from the emission photon) and STOP signal (from the excitation pulse) is measured as an increase in the memory value of a count vs. time difference histogram. For anisotropy measurements, both parallel and perpendicular transients are measured simultaneously on separate sets of TCSPC electronics. The combination of the pulsed dye laser source and TCSPC electronics gives this system an instrument response function of less than 100 ps FWHM.

Translational Diffusion by Fluorescence Recovery After Photobleaching (FRAP). Fluorescence recovery after photobleaching (FRAP) was introduced initially as a means to measure the translational behavior of fluorescent probe molecules in cellular membranes.[46] In a typical FRAP experiment, the fluorescence of a probe molecule is initially measured over a period of time (seconds) to obtain a baseline fluorescence intensity. A brief, high intensity, light source is used to photo-bleach a confocal region of interest containing a subset of the fluorescently labeled probe molecules. The laser is quickly attenuated and used to measure the fluorescence recovery as the unbleached molecules diffuse into the region of interest, and the photobleached molecules diffuse out. The recovery of the fluorescence intensity is strongly dependent upon the translational behavior of the mobile probe molecules. For a system where the probe molecule is free to diffuse and does not undergo binding events, the probe is in a purely diffusion limited regime. We first describe the fitting of the FRAP response curve to a system absent of any binding interactions (pure diffusion), then describe the fitting and extrapolation of both diffusion and binding information from a single FRAP response curve.

A recovery curve for a free chromophore (perylene) in a supported lipid (DMPC) bilayer on a phosphorylated glass surface is shown in figure 2-5. Recovery curves are typically normalized by the Phair double normalization method to account for acquisition bleaching (eqn. 2-11).[47]

$$I_{norm}(t) = \frac{I_{ref-pre}}{I_{ref} - I_{background}} \cdot \frac{I_{frap}(t) - I_{background}}{I_{frap-pre}} \qquad 2\text{-}11$$

For images gathered on supported lipid membranes, the field of view consists of fluorescence from the chromophores of interest and the background signal cannot be measured ($I_{Background}$). The reference is determined as the region over the entire field of view (I_{ref}). The FRAP signal from the region of interest (I_{frap}) are normalized to both the initial (pre-bleach) signals of the region of interest ($I_{frap\text{-}pre}$) and reference ($I_{ref\text{-}pre}$) to force values between 0 and 1.

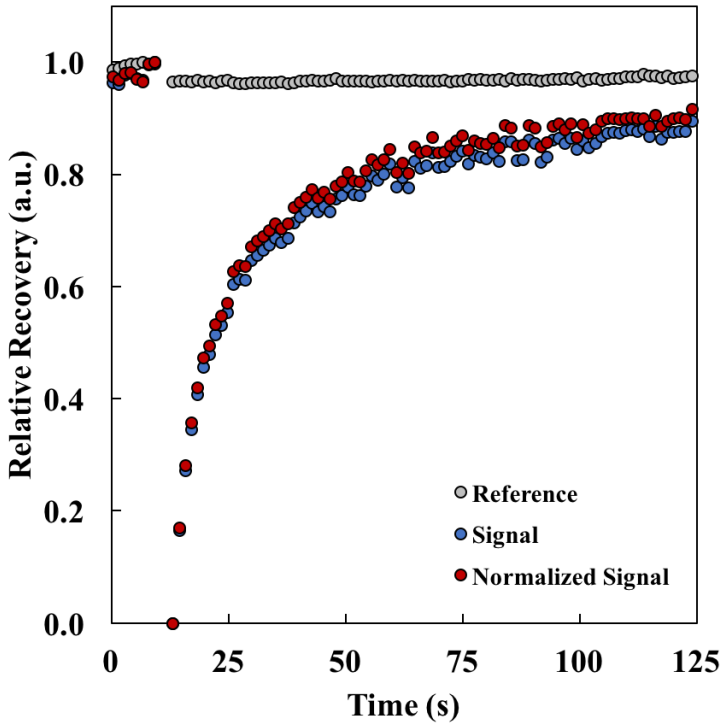

Figure 2-5: Reference, signal, and normalized response FRAP curve of perylene in a solid supported DMPC bilayer.

While acquisition bleaching is often unavoidable, the contribution can be minimized by keeping the attenuated laser intensity low. The time to recover to half of the maximum is termed the characteristic "diffusion time" (τ_D) and is directly proportional to the area during the bleaching event. If the process is diffusion limited, the diffusion time can be related to the translational diffusion constant (D_T) and bleaching radius (ω) by eqn. 2-12.

$$\tau_D = \frac{\omega^2}{4D_T} \qquad 2\text{-}12$$

The functional form of the FRAP curve in the diffusion limited regime is described by the Soumpasis function (eqn. 2-13).[48]

$$I(t) = e^{\left(\frac{-2\tau_D}{t}\right)}\left[I_0\left(\frac{-2\tau_D}{t}\right) + I_1\left(\frac{-2\tau_D}{t}\right)\right] \qquad 2\text{-}13$$

where I_0 and I_1 are the modified Bessel functions of the first kind to the zeroth and first order, respectively.[48] Changes to the functional form for a variety of diffusion constants and bleaching radii (spot sizes) in comparison to the fit raw data (figure 2-5) are shown in figure 2-6. The convenience of this function is that the translational diffusion constant can be determined by fitting a single parameter (τ_D).

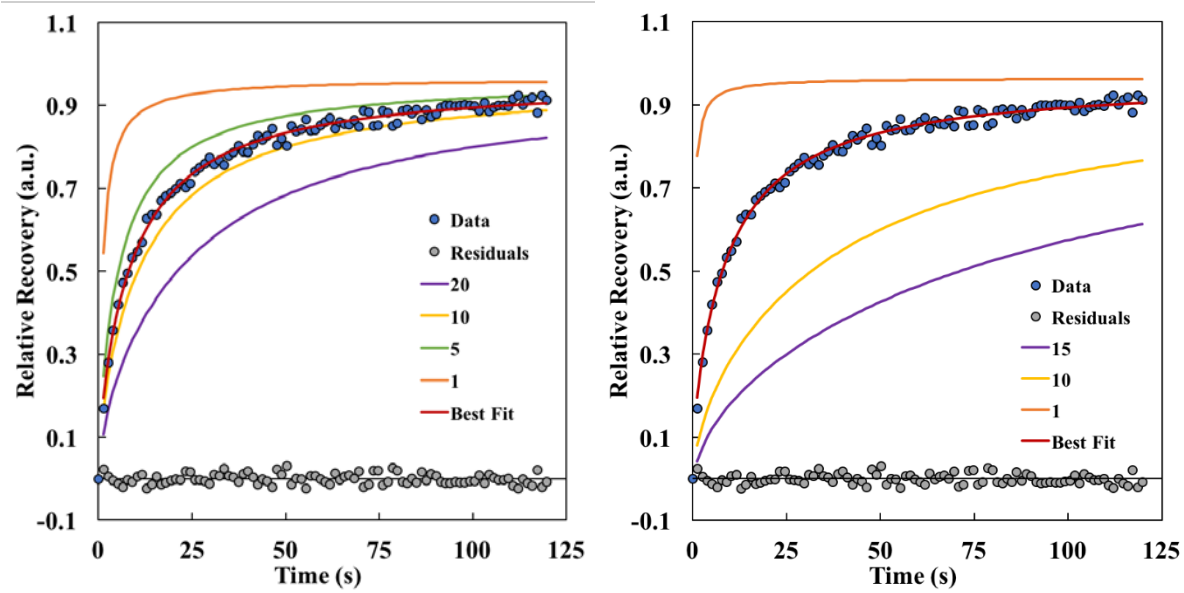

Figure 2-6: Functional form for FRAP curves based on the Soumpasis model for various diffusion times "τ_D" (s) (left) and spot sizes (μm) (right). The best fit for a recovery curve of perylene in a solid supported DMPC bilayer is shown with the residuals below.

For probe molecules that undergo interactions with the surrounding medium or supporting surface, care must be taken to properly fit the acquired data to the proper model. We begin by describing the equations used to analytically solve the diffusion constant for a single binding reaction. A general model for a single binding reaction is given by eqn. 2-14.

$$F + M \underset{k_{off}}{\overset{k_{on}}{\rightleftarrows}} B \qquad 2\text{-}14$$

where $F = [f]$ represents the concentration of free diffusing molecule, $M = [m]$ represents the concentration of an available binding site, such as a phosphonate on the supporting surface, and $B = [b]$ represents the concentration of bound complex between the chromophore and the binding site. Assuming the system has reached equilibrium prior to the bleaching event, and that the binding sites are immobile, the recovery can be described by a set of coupled reaction-diffusion equations[49] eqn. 2-15:

$$\frac{\partial f}{\partial t} = D_t \nabla^2 f - k_{on}^* f + k_{off} b$$
$$\frac{\partial b}{\partial t} = k_{on}^* f + k_{off} b \qquad \text{2-15}$$

where D_t is the diffusion constant of the chromophore, $k^*_{on} = k^*_{on}[m]$ is the pseudo first-order rate constant derived by assuming that the $M = [m]$ is constant, and ∇^2 is the Laplacian operator. For the assumptions to hold, it is important to allow time for the supported film to achieve equilibrium both prior to, and during, imaging. Confirmation of an equilibrium state can be achieved by measuring changes in the fluorescence intensity prior to the bleaching event. Given a system at equilibrium at the start of the FRAP experiment both F and B are at equilibrium:

$$\frac{df}{dt} = \frac{db}{dt} = 0$$
$$k_{on}^* F_{eq} = k_{off} B_{eq} \qquad \text{2-16}$$

Assuming normalization of the FRAP curves between 0 and 1, the final recovery of the free and bound species is equal to:

$$F_{eq} + B_{eq} = 1$$
$$F_{eq} = \frac{k_{off}}{k_{on}^* + k_{off}}, B_{eq} = \frac{k_{on}^*}{k_{on}^* + k_{off}} \qquad \text{2-17}$$

For a system in a reaction-dominant regime, where diffusion is very fast compared to binding and the timescale of the FRAP measurement ($k_{on}^* w^2 / D_T << 1$) the recovery can be fit to a

simple exponential form. Bulinski et al. initially solved a general solution relating the dissociation rate constant (k_{off}) to the functional form of the FRAP curve and Sprague et al. have further related the recovery to both k_{off} and k_{on}^{*} (eqn. 2-18).[49-50]

$$I_{norm}(t) = 1 - B_{eq} e^{-k_{off} t} \qquad 2\text{-}18$$

One important consideration concerning this function is the lack of dependence on the bleaching spot size. Given the change of the functional form for a variety of spot sizes with the same diffusion constant, additional experiments must be done to determine whether the system is in a fast diffusion vs. binding regime. The dissociation rate constant (k_{off}) is inversely related to the square of the bleaching radius. Thus, by plotting the determined k_{off} rate vs. a variety of spot sizes a linear response is expected. A nonlinear response suggests that the system is not in a reaction-dominant regime and will be better fit and described by the full reaction-diffusion model.

Sprague et al. have shown one way to analytically solve the reaction-diffusion differential equations. The inverse Laplace transform of the differential diffusion equations can be performed using the matlab function *invlap.m* on the analytical equation:

$$I_{norm}(t) = \mathcal{L}^{-1}\left\{\frac{1}{p} - \frac{F_{eq}}{p}\cdot\left[1 - 2K_1(q\omega)I_1(q\omega)\right]\cdot\left(1 + \frac{k_{on}^{*}}{p + k_{off}}\right) - \left(\frac{B_{eq}}{p + k_{off}}\right)\right\} \qquad 2\text{-}19$$

where $I_{norm}(t)$ is recovered by taking the inverse Laplace transform, F_{eq} and B_{eq} are related to k^{*}_{on} and k_{off} by eqn. 2-17, K_1 and I_1 are the modified bessel functions, ω is the radius of the bleaching spot and q is described by eqn. 2-20.[51]

$$q = \sqrt{\left(\frac{p}{D_f}\right)\left(1 + \frac{k_{on}^{*}}{p + k_{off}}\right)} \qquad 2\text{-}20$$

While eqn. 2-20 provides solutions for k^{*}_{on} and k_{off} and the translational diffusion constant (D_f), initial parameters for the fit are underdetermined. To estimate the initial parameters, the

recovery curve is fit to both the Soumpasis function (eqn.2-13) and the reaction dominant model (eqn.2-18). The full reaction-diffusion model is best used as a model for a tethered chromophore where the assumptions of the reaction-dominant and Soumpasis models do not hold.

FRAP Instrumentation. The instrument used to perform FRAP measurements is based on an inverted confocal laser scanning microscope (CLSM) (Nikon C2+ system) equipped with a four diode laser bank (Nikon LU-N4, 405 nm, 488 nm, 561 nm, 640 nm). The microscope is equipped with a LED illuminator for the collection of steady state images, a motorized sample stage, and a 3 PMT detector (400-700 nm) (Fig. 2-7).

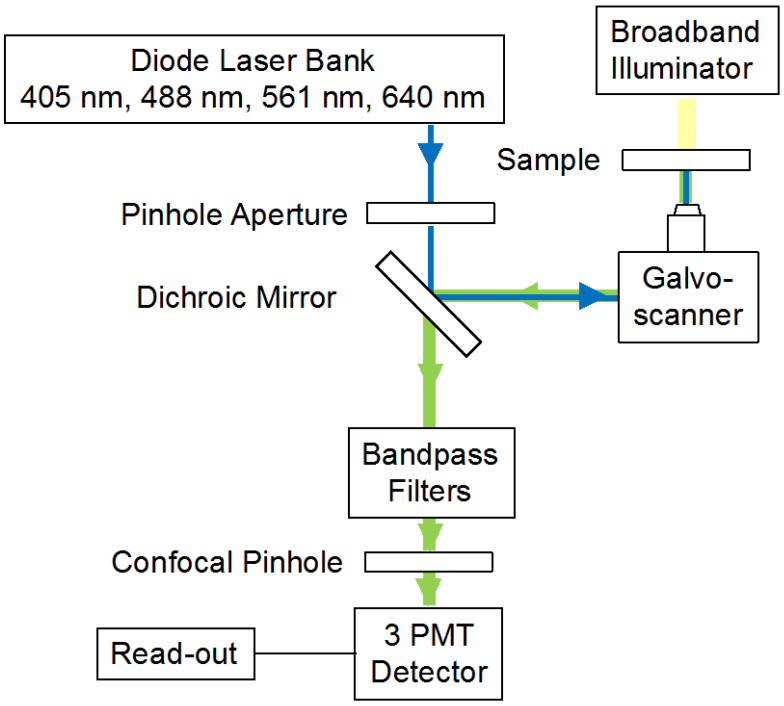

Figure 2-7: Schematic for the Fluorescence Recovery After Photobleaching (FRAP) instrument.

Data obtained from the combination of BAM, FRAP, and FADI instruments are used in subsequent chapters of this dissertation to understand how the fluidity, adhesion, and heterogeneity of supported lipid membranes are influenced by a variety of exogenous factors.

REFERENCES

REFERENCES

1. Seelig, A.; Seelig, J., Dynamic Structure of Fatty Acyl Chains in a Phospholipid Bilayer Measured by Deuterium Magnetic-Resonance. *Biochemistry* **1974,** *13* (23), 4839-4845.

2. Schreier, S.; Polnaszek, C. F.; Smith, I. C. P., Spin Labels in Membranes Problems in Practice. *Biochimica Et Biophysica Acta* **1978,** *515* (4), 375-436.

3. Moser, M.; Marsh, D.; Meier, P.; Wassmer, K. H.; Kothe, G., Chain Configuration and Flexibility Gradient in Phospholipid-Membranes - Comparison between Spin-Label Electron-Spin Resonance and Deuteron Nuclear Magnetic-Resonance, and Identification of New Conformations. *Biophys J* **1989,** *55* (1), 111-123.

4. Lange, A.; Marsh, D.; Wassmer, K. H.; Meier, P.; Kothe, G., Electron-Spin Resonance Study of Phospholipid-Membranes Employing a Comprehensive Line-Shape Model. *Biochemistry* **1985,** *24* (16), 4383-4392.

5. Smith, R. L.; Oldfield, E., Dynamic Structure of Membranes by Deuterium Nmr. *Science* **1984,** *225* (4659), 280-288.

6. Davis, J. H., The Description of Membrane Lipid Conformation, Order and Dynamics by H-2-Nmr. *Biochimica Et Biophysica Acta* **1983,** *737* (1), 117-171.

7. Dicko, A.; Bourque, H.; Pezolet, M., Study by infrared spectroscopy of the conformation of dipalmitoylphosphatidylglycerol monolayers at the air-water interface and transferred on solid substrates. *Chemistry and Physics of Lipids* **1998,** *96* (1-2), 125-139.

8. Desmeules, P.; Penney, S. E.; Desbat, B.; Salesse, C., Determination of the contribution of the myristoyl group and hydrophobic amino acids of recoverin on its dynamics of binding to lipid monolayers. *Biophys J* **2007,** *93* (6), 2069-2082.

9. Brown, K. L.; Conboy, J. C., Phosphatidylglycerol Flip-Flop Suppression due to Headgroup Charge Repulsion. *J Phys Chem B* **2015,** *119* (32), 10252-10260.

10. Brown, K. L.; Conboy, J. C., Lipid Flip-Flop in Binary Membranes Composed of Phosphatidylserine and Phosphatidylcholine. *J Phys Chem B* **2013,** *117* (48), 15041-15050.

11. Brown, K. L.; Conboy, J. C., Influence of Divalent Cations on Phosphatidylserine Lipid Flip-Flop. *Biophys J* **2013,** *104* (2), 241a-241a.

12. Anderson, N. A.; Richter, L. J.; Stephenson, J. C.; Briggman, K. A., Determination of lipid phase transition temperatures in hybrid bilayer membranes. *Langmuir* **2006,** *22* (20), 8333-8336.

13. Levy, D.; Briggman, K. A., Cholesterol/phospholipid interactions in hybrid bilayer membranes. *Langmuir* **2007,** *23* (13), 7155-7161.

14. Magde, D.; Webb, W. W.; Elson, E., Thermodynamic Fluctuations in a Reacting System - Measurement by Fluorescence Correlation Spectroscopy. *Phys Rev Lett* **1972,** *29* (11), 705-706.

15. Eigen, M.; Rigler, R., Sorting Single Molecules - Application to Diagnostics and Evolutionary Biotechnology. *P Natl Acad Sci USA* **1994,** *91* (13), 5740-5747.

16. Rigler, R., Fluorescence Correlations, Single-Molecule Detection and Large Number Screening - Applications in Biotechnology. *J Biotechnol* **1995,** *41* (2-3), 177-186.

17. Rigler, R.; Mets, U.; Widengren, J.; Kask, P., Fluorescence Correlation Spectroscopy with High Count Rate and Low-Background - Analysis of Translational Diffusion. *Eur Biophys J Biophy* **1993,** *22* (3), 169-175.

18. Widengren, J.; Thyberg, P., FCS cell surface measurements - Photophysical limitations and consequences on molecular ensembles with heterogenic mobilities. *Cytom Part A* **2005,** *68a* (2), 101-112.

19. Richter, R. P.; Berat, R.; Brisson, A. R., Formation of solid-supported lipid bilayers: An integrated view. *Langmuir* **2006,** *22* (8), 3497-3505.

20. Reimhult, E.; Hook, F.; Kasemo, B., Intact vesicle adsorption and supported biomembrane formation from vesicles in solution: Influence of surface chemistry, vesicle size, temperature, and osmotic pressure. *Langmuir* **2003,** *19* (5), 1681-1691.

21. Jing, Y. J.; Trefna, H.; Persson, M.; Kasemo, B.; Svedhem, S., Formation of supported lipid bilayers on silica: relation to lipid phase transition temperature and liposome size. *Soft Matter* **2014,** *10* (1), 187-195.

22. Wikstrom, A.; Svedhem, S.; Sivignon, M.; Kasemo, B., Real-Time QCM-D Monitoring of Electrostatically Driven Lipid Transfer between Two Lipid Bilayer Membranes. *J Phys Chem B* **2008,** *112* (44), 14069-14074.

23. Honig, D.; Mobius, D., Direct Visualization of Monolayers at the Air-Water-Interface by Brewster-Angle Microscopy. *J Phys Chem-Us* **1991,** *95* (12), 4590-4592.

24. Brewster, D., On the Laws Which Regulate the Polarisation of Light by Reflexion from Transparent Bodies. *Philosophical Transactions of the Royal Society of London* **1815,** *105*, 125-129.

25. Fresnel, A., *Œuvres Complètes d'Augustin Fresnel* Imprimerie impériale: Paris, 1866-1870.

26. Lord Rayleigh, F. R. S., On the manufacture and theory of diffraction-gratings. *Philosophical Magazine Series 4* **1874,** *47* (310), 81-93.

27. Lord Rayleigh, F. R. S., Investigations in optics, with special reference to the spectroscope. *Philosophical Magazine Series 5* **1879,** *8* (49), 261-274.

28. Szabo, A., Theory of fluorescence depolarization in macromolecules and membranes. *The Journal of Chemical Physics* **1984,** *81*, 17.

29. Chuang, T. J.; Eisenthal, K. B., Theory of Fluorescence Depolarization by Anisotropic Rotational Diffusion. *J Chem Phys* **1972,** *57* (12), 5094-+.

30. Baumann, J.; Fayer, M. D., Excitation Transfer in Disordered Two-Dimensional and Anisotropic 3-Dimensional Systems - Effects of Spatial Geometry on Time-Resolved Observables. *J Chem Phys* **1986,** *85* (7), 4087-4107.

31. Ediger, M. D.; Domingue, R. P.; Fayer, M. D., Picosecond Studies of Excitation Transport in a Finite Volume - the Clustered Transport-System Octadecyl Rhodamine-B in Triton X-100 Micelles. *J Chem Phys* **1984,** *80* (3), 1246-1253.

32. Ediger, M. D.; Fayer, M. D., Electronic Excited-State Transport among Molecules Distributed Randomly in a Finite Volume. *J Chem Phys* **1983,** *78* (5), 2518-2524.

33. Gochanour, C. R.; Fayer, M. D., Electronic Excited-State Transport in Random-Systems - Time-Resolved Fluorescence Depolarization Measurements. *J Phys Chem-Us* **1981,** *85* (14), 1989-1994.

34. Suhling, K.; French, P. M. W.; Phillips, D., Time-resolved fluorescence microscopy. *Photoch Photobio Sci* **2005,** *4* (1), 13-22.

35. Debye, P., *Polar Molecules*. Dover: New York, 1929.

36. Stokes, G. G., On the Effect of the Internal Friction of Fluids on the Motion of Pendulums. *Transactions of the Cambridge Philosophical Society* **1856,** *9*.

37. Stokes, G. G., On the Theories of the Internal Friction of Fluids in Motion and of the Equilibrium and Motion of Elastic Solids. *Transactions of the Cambridge Philosophical Society* **1849,** *8*.

38. Einstein, A., Über die von der molekularkinetischen Theorie der Wärme geforderte Bewegung von in ruhenden Flüssigkeiten suspendierten Teilchen. *Annalen der Physik* **1905,** *322* (8), 11.

39. Einstein, A., Zur Theorie der Brownschen Bewegung. *Annalen der Physik* **1906,** *324* (2), 10.

40. Edward, J. T., Molecular Volumes and Stokes-Einstein Equation. *J Chem Educ* **1970,** *47* (4), 261-&.

41. Perrin, F., The Brownien movement of an ellipsoide. - The dielectric dispersion of ellipsoidal molecules. *J Phys-Paris* **1934,** *5*, 497-511.

42. Perrin, F., Brownian movement of an ellipsoid (II). - Free rotation and depolarisation of fluourescences. - Translation and diffusion of ellipsoidal molecules. *J Phys-Paris* **1936,** *7*, 1-11.

43. Hu, C. M.; Zwanzig, R., Rotational Friction Coefficients for Spheroids with Slipping Boundary-Condition. *J Chem Phys* **1974,** *60* (11), 4354-4357.

44. Lipari, G.; Szabo, A., Effect of Librational Motion on Fluorescence Depolarization and Nuclear Magnetic-Resonance Relaxation in Macromolecules and Membranes. *Biophys J* **1980,** *30* (3), 489-506.

45. Fleming, G., *Chemical Applications of Ultrafast Spectroscopy*. Oxford University Press: New York, NY, 1986.

46. Axelrod, D.; Koppel, D. E.; Schlessinger, J.; Elson, E.; Webb, W. W., Mobility Measurement by Analysis of Fluorescence Photobleaching Recovery Kinetics. *Biophys J* **1976,** *16* (9), 1055-1069.

47. Phair, R. D.; Gorski, S. A.; Misteli, T., Measurement of dynamic protein binding to chromatin in vivo, using photobleaching microscopy. *Method Enzymol* **2004,** *375*, 393-414.

48. Soumpasis, D. M., Theoretical-Analysis of Fluorescence Photobleaching Recovery Experiments. *Biophys J* **1983,** *41* (1), 95-97.

49. Sprague, B. L.; Pego, R. L.; Stavreva, D. A.; McNally, J. G., Analysis of binding reactions by fluorescence recovery after photobleaching. *Biophys J* **2004,** *86* (6), 3473-3495.

50. Bulinski, J. C.; Odde, D. J.; Howell, B. J.; Salmon, T. D.; Waterman-Storer, C. M., Rapid dynamics of the microtubule binding of ensconsin in vivo. *J Cell Sci* **2001,** *114* (21), 3885-3897.

51. Hollenbeck, K. J. *INVLAP.M: A matlab function for numerical inversion of Laplace transforms by the de Hoog algorithm*, 1998.

CHAPTER 3: LIPID ADLAYER ORGANIZATION MEDIATED BY A LIQUID OVERLAYER

Adapted with permission from:

S. M. Baumler and G. J. Blanchard; Lipid adlayer organization mediated by a liquid overlayer. Spectrochimica Acta Part A: Molecular and Biomolecular Spectroscopy 98 (2012) 429–435.

3.1 Abstract

Formation of a chemically bound 1,2-dimyristoyl-*sn*-glycero-3-phosphocholine (DMPC) monolayer on modified gold and silica surfaces, and changes in the organization of the interfacial lipid layer associated with immersion in aqueous solution were examined. The interface was studied using steady state and time resolved fluorescence spectroscopy, water contact angle, optical ellipsometry measurements, and electrochemical methods. The DMPC adlayer in contact with air forms a relatively well organized interface that mediates the rotational motion of perylene. In the presence of an aqueous overlayer, perylene reorientation becomes more rapid, consistent with a reduction in the organization of the interfacial lipid adlayer. One implication of this finding is that the interfacial adlayer is less than a uniform monolayer, which is confirmed by electrochemical impedance data. These findings underscore the importance of water in mediating the organization of interfacial lipid adlayers.

3.2 Introduction

The development of chemical sensing strategies has relied heavily on the ability to modify interfaces to impart chemical selectivity. Among the most important aspects of chemical surface modification has been the effort to create biomimetic interfaces. The creation of such interfaces is critical to the development of selective sensors that employ biomolecules such as transmembrane proteins and certain enzymes. For these reasons, there has been much effort invested in the creation of supported lipid adlayer structures. Lipid membrane composition and organization are central to the function of transmembrane proteins, with many important cellular activities requiring a specific lipid membrane micro-domain in order to allow the transmembrane protein to function.

Membrane fluidity, which is inextricably tied to membrane composition, also plays an important role in allowing processes such as cell adhesion, ion channeling, and cell signaling to operate.[1-3]

For a biomimetic interface to be useful for sensing or other applications, the interface must be supported on a solid substrate for chemical signal transduction by electrochemical, spectroscopic or gravimetric means, and for other applications the presence of a solid substrate is required to impart the requisite physical robustness to the interface. There have been a number of strategies put forth for attaching biomimetic interfaces to surfaces.[4-6] Simple physisorption processes such as those responsible for the formation of Langmuir-Blodgett films on solid supports are typically not robust enough to provide the properties needed for most biomimetic interfaces. Several strategies offer abundant chemical and physical integrity, but the issue of adlayer fluidity remains to be addressed fully for such systems.[7-14]

Extensive attention has been paid to the preparation of air stable supported membrane interfaces because of the fragility of typical bilayer systems and the potential utility of biomimetic systems able to withstand direct exposure to the ambient environment.[15-16] Preparing a robust system would have use in bio-electronics and would allow for a stable model to investigate functional proteins. Because of the requirement of a robust system and the intended applications for such a system, three common attributes are sought when preparing bound interfacial systems. The systems should be physically robust, easily and reproducibly prepared, and be sufficiently uniform to allow subsequent processing for specific applications.

When lipid adlayers are deposited onto, or bound to an interface in a layer-by-layer manner, there is at least one step in the process that necessarily presents a non-polar interface for subsequent processing. It is this step in the formation of a biomimetic interface that we are concerned with in this work. Specifically, the creation of a non-polar interface may proceed with substantial order.

Due to the processing of such interfaces in the laboratory environment, it is often impossible to prevent the exposure of the interface to adventitious water, and sometimes aqueous solutions are used in the deposition of subsequent layers. The interaction(s) between the nonpolar region of the interfacial layer and water could, in principle, alter the organization of the nonpolar region of the layer prior to or during subsequent adlayer deposition steps. We have formed a phospholipid adlayer on polar surfaces to produce an interface with its non-polar region being exposed to the environment. Examination of the non-polar region of the interface as a function of its exposure to the ambient environment and aqueous solution demonstrates that the organization of the interface is indeed sensitive to the presence of bulk water. Ionically bound phospholipids are capable of exhibiting significant organization and have been shown to withstand ambient environmental conditions without loss of structural integrity.[14, 17-19] The presence of bulk water, however, has a substantial effect on the organization of the adlayer. The motional dynamics of a non-polar chromophore sequestered within the lipid adlayer reveal a change in acyl chain organization that gives rise to increased motional freedom when the interface is exposed to water.

3.3 Experiment

Materials. Acetonitrile, chloroform, ethanol (100%), toluene, Tris® buffer, 2,4,6-collidine, (3-aminopropyl) dimethylethoxysilane (APDMES), 6-mercapto-1-hexanol, phosphorus oxychloride, potassium ferrocyanide trihydrate, potassium chloride, perylene, and zirconyl chloride octahydrate were obtained from Sigma Aldrich in the highest purity grade available and were used as received. The phospholipid 1,2-dimyristoyl-*sn*-phosphatidylcholine (14:0 DMPC) was purchased from Avanti Polar Lipids, Inc., and used without further purification. Water (18 MΩ) was obtained from a Milli-Q Plus water purification system and used for all experiments.

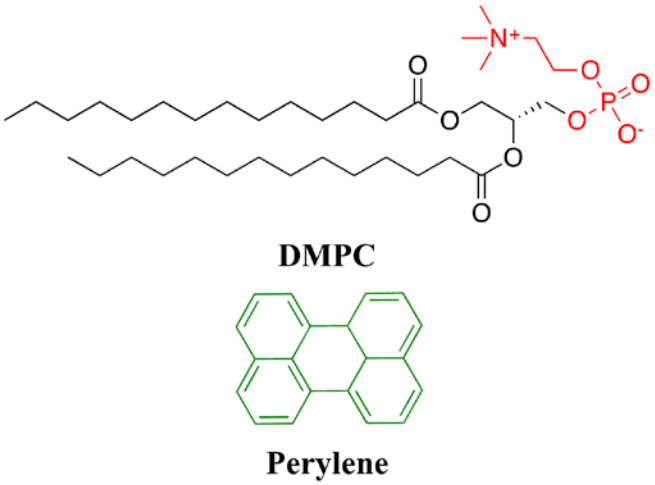

Figure 3-1: Chemical Structures of 1,2-dimyristoyl-*sn*-phosphatidylcholine (DMPC) and Perylene.

Metal-Phosphate Monolayer Synthesis. Silica and gold substrates were prepared by a procedure described elsewhere.[20-22] Silica substrates were immersed in piranha solution ($1H_2O_2$:$3H_2SO_4$, *Caution! Strong oxidizer!*) for 20 min., rinsed with distilled water, then ethanol and dried under a $N_2(g)$ stream. The silica substrates were then immersed in a 0.5% v/v solution of (3-aminopropyl)dimethylethoxysilane in dry toluene for *ca*. 12 hrs. Gold substrates (*ca*. 200 nm Au vapor-deposited on Si(100) with a 20 nm Ti adhesion layer) were treated with 10 mM 6-mercapto-1-hexanol in ethanol for *ca*. 12 hrs. Following the reactions, both substrates were rinsed with ethanol and dried under a $N_2(g)$ stream. The APDMES adlayers on silica and gold substrates were then exposed to $POCl_3$ (0.4 mL) in dry acetonitrile (10 mL), catalyzed with 2,4,6-collidine (0.4 mL) for 3 hrs. at 20°C. The gold substrates were then rinsed with ethanol and distilled water and the silica substrates were rinsed with acetonitrile. Both substrates were dried with a $N_2(g)$ stream. Zirconation of the phosphate-terminated silica and gold substrates was achieved by immersion in 5 mM $ZrOCl_2$ in 60:40 ethanol/water solution for 12 hrs. The resulting zirconated

substrates were rinsed with water and dried under a $N_2(g)$ stream, and reacted with a solution containing unilamellar phospholipid vesicles.

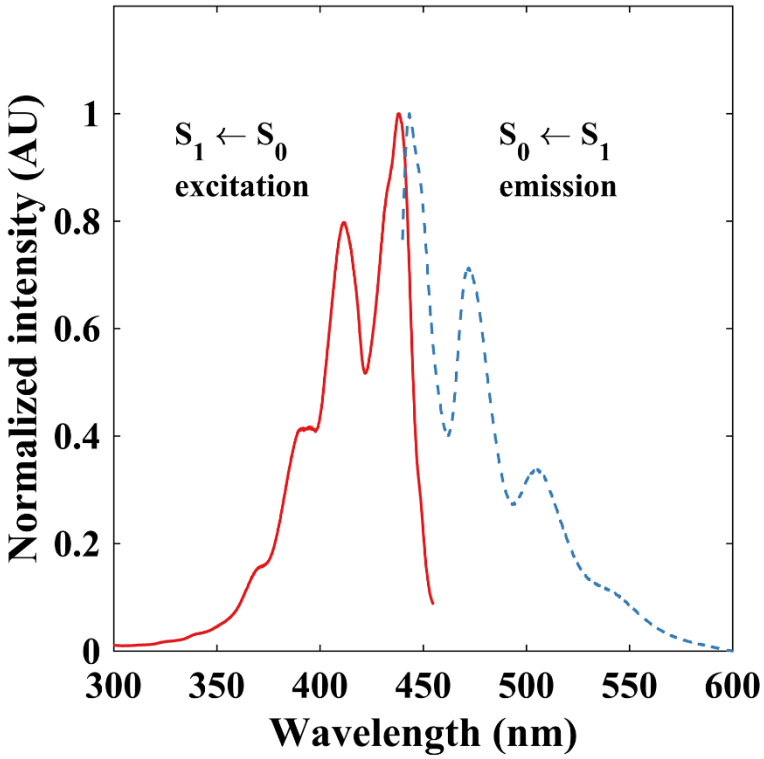

Figure 3-2: Steady state excitation ($S_1 \leftarrow S_0$, solid line) and emission ($S_0 \leftarrow S_1$, dashed line) of perylene in DMPC vesicles prior to formation of the lipid monolayer.

Vesicle Preparation. For each substrate, 10 mg of the phospholipid 14:0 DMPC was mixed with 50 µg of perylene (0.5 wt%) (Fig. 3-1). The chloroform was then evaporated and the resulting solid mixture dried *in vacuo*. Tris® buffer (10 mM, pH 7.5) was prepared with 18 MΩ water and added to the sample to make the final lipid concentration 1 mg/mL and a perylene concentration of 20 µM. The lipid and chromophore mixture was processed through five freeze-thaw-vortex cycles to ensure thorough mixing.[15] Each cycle consisted of a 5 min. freeze by immersion in $N_2(l)$, 5 min. thaw in a 60°C water bath, and a 2 min. vortex. After five such cycles, the samples were extruded eleven times through a Nucleopore® polycarbonate membrane (Whatman) with 400 nm

diameter pores using a mini-extruder apparatus (Avanti Polar Lipids, Inc.) to produce unilamellar vesicles.[16-17] Figure 3-2 contains the normalized steady state excitation and emission spectra of perylene contained in the extruded vesicles. Previous work has shown that the steady state spectra of perylene are insensitive to the phase or structural format (*i.e.* vesicle, supported bilayer) of the lipid bilayer medium.[23-24] Time resolved spectroscopic data provide more environmental information for this chromophore.

Lipid Adlayer Formation. Phospholipid adlayers were formed by spontaneous fusion of unilamellar lipid vesicles onto the zirconated substrate surfaces (Fig. 3-3).[25] A Teflon® flow cell constructed in-house was used to ensure consistent contact between the substrate and vesicle solution during the phospholipid adlayer formation process.[17] The substrate was conditioned with a Tris® buffer solution introduced at a rate of *ca*. 5 mL/min. The vesicle-containing solution was introduced at the same rate until the buffer was displaced by *ca*. 4 mL of solution. The flow cell inlet and outlet were then sealed and the system was allowed to react for 2 hrs. Water (18 MΩ) was subsequently flowed through the cell to rinse the substrates, which were then removed from the flow cell and mounted vertically in a loosely capped vial to dry.

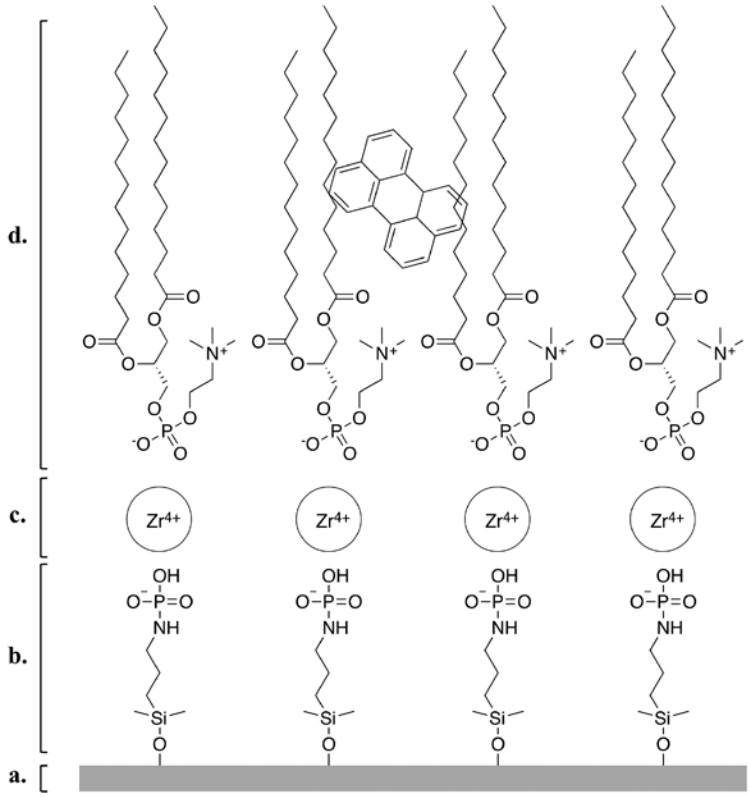

Figure 3-3: Idealized diagram of the prepared supported lipid layer. The films are composed of the (a.) gold or silicon support, (b.) phosphorylated APDMES (c.) zirconation layer, and (d.) DMPC layer.

Steady State Fluorescence Measurements. Excitation and emission spectra were recorded for our samples (Jobin Yvon Fluorolog-3) to verify the presence and band positions of the incorporated perylene chromophore. Spectral resolution was set to 3 nm for both the excitation and emission monochromators.

Time Resolved Fluorescence Measurements. Fluorescence lifetime and anisotropy measurements were performed using an instrument that has been described in detail in Chapter 2 and we recap its salient features below. The light source for the system is a CW passively mode-

locked Nd:YVO_4 laser (Spectra Physics Vanguard) that produces 13 ps pulses at 1064 nm at a repetition rate of 80 MHz. The third harmonic output of this laser excites a cavity-dumped dye laser (Coherent 702-2). The output of the dye laser is typically 5 ps fwhm pulses at a repetition rate of 4 MHz, determined by the cavity dumping electronics (Gooch and Housego). Stilbene 420 dye (Exciton) used to excite the samples at 440 nm. The pulses from the dye laser are divided, with approximately one half going to a reference diode (Becker and Hickl PHD-400-N), and the other half going to the sample. The sample is excited with the vertically polarized light pulses and emission is collected at polarizations parallel and perpendicular to the excitation polarization. The polarized emission data are collected simultaneously using subtractive double monochromators (Spectral Products CM-112) equipped with micro-channel plate PMT detectors (Hamamatsu R3809U-50) detectors. Detection electronics resolve the parallel and perpendicular signals separately (Becker and Hickl SPC-132). Collection wavelength, data acquisition, and detector bias are all controlled using a program written in-house (National Instruments LabVIEW®).

Electrochemical measurements. Data were acquired using a CH Instruments 650 electrochemical bench. The solution used to characterize the interfaces was 0.1 M KCl. Cyclic voltammograms (CV) were recorded with 3 independent scans cycled two times each at a scan rate of 0.1 V/s. The substrates were scanned from -0.1 V to 0.4 V vs. Ag/AgCl using a Pt counter electrode. Impedance measurements were collected using the same probe, and counter and reference electrodes. A frequency range of 0.1 Hz to 10^5 Hz was used at an AC amplitude of 5 mV. The center voltage was set as E_0, determined by the individual CV scans (0.26 V vs Ag/AgCl).

3.4 Results and Discussion

The design and demonstration of physically and chemically robust biomimetic interfaces has generated substantial research interest for both fundamental and applied reasons. One aspect of this work has been the chemical binding of interfacial adlayers, with an ultimate goal of utilizing such systems for chemical sensing applications. Because of the amphiphilic nature of lipids, the details of how a supported lipid bilayer is formed can have a substantial impact on the organization and properties of the interface. Specifically, for systems formed one lipid layer at a time with the acyl chains exposed, the lipid layer is at some point exposed to a polar (aqueous) liquid overlayer. We are interested in this work in determining the consequences of this exposure on the organization of that layer. We consider the thickness, uniformity and permeability of an interfacial lipid monolayer as well as its intralayer organization.

Interfacial thickness and hydrophobicity. Optical ellipsometry and contact angle measurements were performed to confirm phospholipid adlayer formation and to determine the monolayer or bilayer status of the substrate. Adlayers formed on the gold substrates were determined to have a thickness of 48 ± 10 Å, and water contact angles of 84° ± 9. The silica substrates exhibit the same contact angle (95° ± 5) to within the uncertainty of the measurements. The ellipsometric and contact angle data are consistent with the formation of a DMPC monolayer on both support materials.[17] We note that the ellipsometric thickness appears to be somewhat thicker than a hydrated DMPC layer, but the value of 48 ± 10 Å also contains the thickness of the phosphate and zirconated APDMES adlayer (*ca.* 15 Å). The data that we report for each technique represent an average of at least three determinations per substrate. Each substrate was measured at least three times at different locations, and the results were averaged. The contact angle

measurements follow the same procedure and were measured after allowing the droplet to 'settle' for *ca.* 30 sec. before the measurement was taken.

Chromophore motion within the lipid layer. We have measured the fluorescence anisotropy decay of perylene imbedded in the bound DMPC adlayer when it is exposed to air and immersed in water. Anisotropy decay measurements contain information on the motional freedom of the chromophore. The orientational anisotropy decay function, *R(t)* eqn. 3-1, is the normalized difference between polarized emission transients $I_{||}(t)$ and $I_{\perp}(t)$, where the polarizations are relative to the vertically polarized excitation pulse.

$$R(t) = \frac{I_{||}(t) - I_{\perp}(t)}{I_{||}(t) + 2I_{\perp}(t)} \qquad 3\text{-}1$$

The functional form of *R(t)* is related to the chemical information contained in these data. Chuang and Eisenthal have derived the relationship between the polarized emission transients, the orientations of the chromophore absorbing and emitting transition moments, and the Cartesian components of the rotational diffusion coefficient, *D* eqn. 3-2.[27]

$$D = \tfrac{1}{3}\left(D_x + D_y + D_z\right) \qquad 3\text{-}2$$

In their model, the volume swept out by the reorienting molecule is described as a prolate or oblate ellipsoidal shape, with control over the aspect ratio of the ellipsoid of rotation. While the Chuang and Eisenthal equations provide for up to five exponential decay components in *R(t)*, either one or two decay components are observed experimentally. Depending on the number of decay components and the relative orientations of the excited and emitting transition moments, prolate and oblate ellipsoidal rotor shapes give rise to different functional forms of *R(t)*. The $S_1 \leftarrow S_0$ transition dipole moment of perylene lies in the long in-plane axis of the chromophore, which

we designate the x-axis. For perylene the y-axis is the short in-plane axis, and the z-axis is perpendicular to the π-system plane. For rotation as a prolate rotor with x-axis rotation being dominant ($D_x > D_y = D_z$), R(t) is given by eqn. 3-3,

$$R(t) = 0.4\exp(-6D_z t) \qquad 3\text{-}3$$

For rotation as an oblate (z-axis dominant) rotor ($D_z > D_x = D_y$), a two-component exponential decay of *R(t)* is expected (eqn. 3-4),

$$R(t) = 0.1\exp(-(2D_x + 4D_z)t) + 0.3\exp(-6D_x t) \qquad 3\text{-}4$$

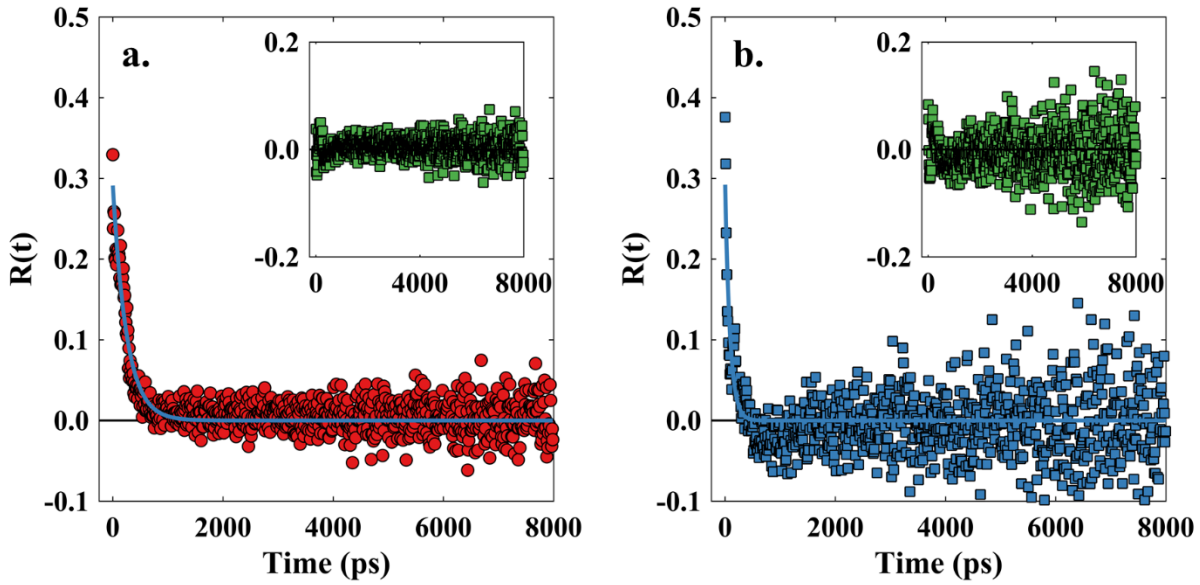

Figure 3-4: Induced orientational anisotropy decay data for perylene in DMPC monolayer on SiO_x substrates, (a.) exposed to air and (b.) exposed to an aqueous overlayer. The solid lines are the best fit, single exponential decay function. Insets represent residuals of fit.

We observe a single exponential anisotropy decay for the measurements we report here, consistent with perylene reorienting as a prolate rotor (eqn. 3-3, Fig. 3-4). It is useful to place this result in context. Perylene is capable of reorienting either as a prolate rotor or as an oblate rotor, depending on its local environment.[24, 28] In *n*-alkanes, perylene reorients as a prolate rotor[28] and in other

environments, such as within a lipid bilayer, perylene has been shown to reorient as an oblate rotor.[24] The fact that we observe a single exponential decay in this work underscores the difference between the characteristic organization within a lipid monolayer and that within a lipid bilayer structure.

The data presented in Table 3-1 reveal a statistically discernible difference between the reorientation dynamics of perylene in lipid monolayers that are in contact with air and those immersed in water. Specifically, the reorientation time constant of perylene in bound lipid adlayers in contact with air is *ca*. 40% *slower* than when the monolayer is immersed in water. This finding indicates that the lipid monolayer in contact with air is better able to form organized structure(s) within its nonpolar region. We assert that bulk water in contact with the nonpolar acyl chains of the lipid adlayer disrupts the organization of the lipid acyl chain region. It is important to recognize that, regardless of whether we have a full or partial lipid adlayer, the perylene chromophore will reside in the most non-polar portion of the interface, which is the acyl chain region of the lipid adlayer. Our rotational diffusion data thus indicate that exposure of the interface to water decreases the order that exists within the phospholipid acyl chain region(s) of the interface. We will consider the implications of this finding after discussing the chromophore reorientation data in detail.

Table 3-1: Reorientation time (τ_{OR}), Rotational Diffusion Constant (D), and Calculated Local Viscosity (η) determined by Local Environment for DMPC Bound to a Modified Silica Substrate.

	Ambient Adlayer			Aqueous Adlayer		
Substrate	**τ_{OR} (ps)**	**D (MHz)**	**η (cP)**	**τ_{OR} (ps)**	**D (MHz)**	**η (cP)**
S1	351 ± 72	487 ± 90	4.5 ± 0.9	101 ± 6	1651 ± 103	1.3 ± 0.1
S2	281 ± 11	594 ± 22	3.6 ± 0.1	183 ± 34	932 ± 156	2.3 ± 0.4
S3	288 ± 77	604 ± 132	3.7 ± 1.0	105 ± 32	1733 ± 632	1.3 ± 0.4
Average	**307 ± 39**	**562 ± 82**	**3.9 ± 0.5**	**130 ± 46**	**1439 ± 297**	**1.7 ± 0.6**

Errors are ± 1σ for at least 3 individual determinations, on each substrate, and in each environment.

In addition to the shape of the volume swept out by the rotating chromophore, it is also useful to relate the experimental data to physico-chemical properties of the local environment. The modified Debye-Stokes-Einstein (DSE) equation (eqn. 3-5) provides a means of relating the rotational diffusion constant, D (eqn. 3-2), to the local viscosity of the medium.[29-32]

$$D = \frac{k_B T S}{6\eta V f} \qquad 3\text{-}5$$

This model is well established for a variety of solution phase systems, where η is the viscosity of the medium surrounding the rotating chromophore, V is the chromophore hydrodynamic volume (225 Å^3),[33] S is a shape factor relating to the ellipsoidal shape of the chromophore ($S = 0.69$)[31-32] and f is a term to account for frictional contributions to the interaction between the chromophore and its surroundings ($0 \leq f \leq 1$).[30] This model was derived for reorientation of dipolar species in a continuum medium, and a direct comparison between a chemically-bound DMPC adlayer on a planar substrate and a bulk liquid solvent requires some caution. It is nonetheless useful to examine the bound lipid layer using the DSE model because of the fluid nature of the adlayer acyl chain region. The experimental data demonstrate that perylene is able to execute rotational motion within the acyl chain environment, but comparison of the "viscosity" of the adlayer to that of a bulk liquid is tenuous because of the quasi two-dimensional nature of the adlayer and the fact that it is bound to the interface. Given this caveat, the rotational motion of perylene in the adlayer acyl chain region exhibits an apparent viscosity that is similar to that seen for alkanes that are similar in length to the acyl chains (Table 3-1). The viscosity of tridecane, tetradecane, and hexadecane are 1.7 cP, 2.1 cP, and 3.0 cP, respectively, at 25°C.[34]

What is most significant about these data is, however, that the immersion of the surface-bound adlayer into water gives rise to a substantial *decrease* in the perylene reorientation time constant. This substantial change in the rotational diffusion constant of the chromophore is

consistent with a loss of organization in the acyl chain region of the adlayer. It is unfortunately not possible to elucidate possible changes in the aspect ratio of the ellipsoid of rotation that describes perylene reorientation in this adlayer, but such a determination is not possible when only a single exponential anisotropy decay is recovered (eqn. 3-3). The fact that the chromophore experiences more motional freedom within the adlayer when it is immersed it water invites speculation on the cause of this effect. Electrochemical data can provide some insight into possible explanations for this finding.

Interfacial thickness and heterogeneity characterization. Determining the thickness and extent of surface coverage of a surface-bound adlayer can be challenging. We have measured the thickness of our APDMES+ZP+DMPC adlayers on Au ellipsometrically to be 48 ± 10 Å, but this thickness value does not address heterogeneity of the adlayer. We use electrochemical methods for this purpose. We recognize that the process of vesicle fusion is complex and system-specific, and in general, that it is not possible to compare lipid adlayers formed on silica and Au surfaces directly.[4-6] The work presented here, however, is somewhat different than most other studies of surface-bound lipid adlayers. In this work we functionalize both the silica and Au surfaces to form terminal phosphate moieties, followed by treating those surfaces with Zr^{4+} prior to exposure to the phospholipid. While there will certainly be differences, in detail, between the silica and Au surfaces, the fact that both are terminated with the same chemical functionality provides a greater correspondence between these surfaces than would be found if no surface modification had been applied.

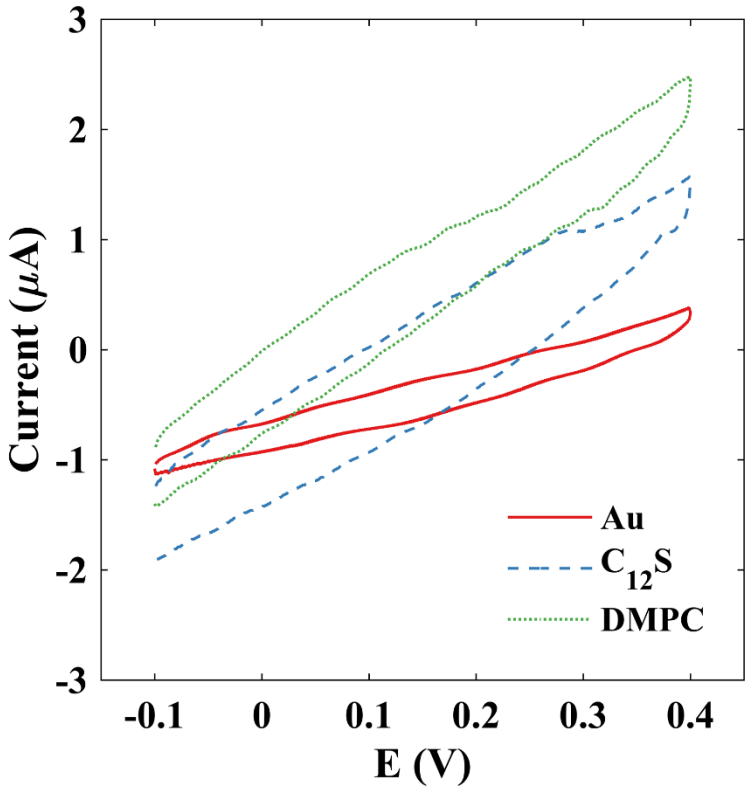

Figure 3-5: Cyclic voltammograms of a blank Au surface (—), a C_{12} thiol monolayer (---) and a DMPC adlayer bound to Au (·····). All CVs were taken in 0.1M KCl (aq) solution at a scan rate of 100 mV/s.

The fractional coverage of the surface can be estimated through the capacitance of the interface. For a uniform adlayer, the capacitance is related to the adlayer thickness through (eqn. 3-6),

$$C = \frac{\varepsilon_0 \varepsilon A}{\ell} \qquad 3\text{-}6$$

where ε is the dielectric constant of the interface, ε_0 is the permittivity of free space ($\varepsilon_0 = 8.854 \times 10^{-12}$ F/m), A is the area of the electrode and ℓ is the thickness of the interfacial adlayer. For a heterogeneous structure, however, such a relationship does not hold directly and the total capacitance measured by cyclic voltammetry (Fig. 3-5) is modeled as distinct contributions from the covered and bare regions of the interface. The equivalent circuit for such a heterogeneous

surface is two capacitors in parallel, with one being related to the adlayer-coated regions and the other being related to the bare regions (eqn. 3-7),[35]

$$C_{tot} = \theta C_{ml} + (1-\theta)C_{dl} \qquad 3\text{-}7$$

where θ is the fractional surface coverage by the adlayer, C_{ml} is the capacitance of the coated regions and C_{dl} is the double layer capacitance, characteristic of the bare electrode regions.

Because two quantities in eqn. 3-7 are measurable, C_{tot} and C_{dl}, it is not possible using cyclic voltammetry alone to determine uniquely θ and C_{ml}. For this reason, we have chosen to use AC impedance measurements to extract information on interfacial coverage and heterogeneity. AC impedance data is presented in the form of Nyquist plots (Fig. 3-6),[36] where the real and imaginary parts of the measured impedance are plotted against one another as a function of frequency. For both the DMPC (Fig. 3-6) and the $C_{12}SH$ self-assembled monolayer (SAM, Fig. 3-6), the bare gold substrate (open dots) produces Nyquist plots consistent with a diffusion-limited reaction. For the $C_{12}SH$ and DMPC adlayers, the Nyquist plots are consistent with partial monolayer films. The relationship between θ, the fractional surface coverage, and R_{ct} is given by eqn. 3-8.[35]

$$\theta = 1 - \frac{R_{ct}^{0}}{R_{ct}} \qquad 3\text{-}8$$

where R_{ct}^{0} is the charge transfer resistance for a bare substrate and R_{ct} is the charge transfer resistance for the adlayer-containing interface. We obtain a value of R_{ct}^{0} = 50 Ω from modeling of the complex impedance data using a Randles equivalent circuit (Fig. 3-6 inset).[37-40] Cyclic voltammetry measurements give values of C_{dl} = 22 μF for the C_{12} SAM and 19.5 μF for the DMPC adlayer, and using these values we obtain R_{ct} = 545 Ω for the C_{12} SAM and R_{ct} = 105 Ω for the DMPC adlayer. These data yield θ = 0.91 for the $C_{12}SH$ adlayer and θ = 0.52 for the DMPC

adlayer. With the quantity θ, one can determine C_{ml} (eqn. 3-7), which allows estimation of ℓ (eqn. 3-6).

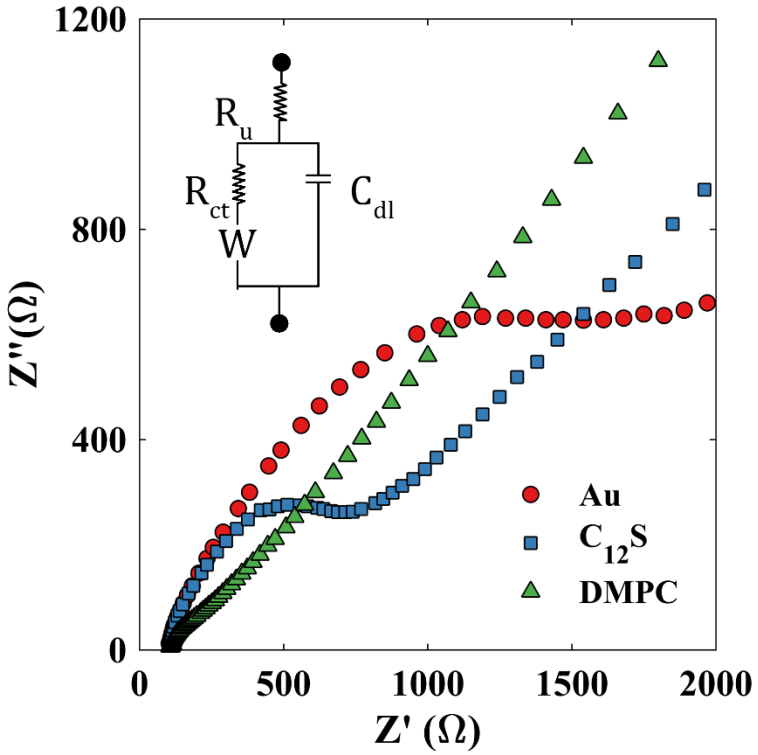

Figure 3-6: AC impedance for a blank Au surface (●), a C_{12} thiol SAM on Au (■), and a DMPC adlayer bound to Au (▲). Inset: Equivalent circuit used to extract R_{ct} values from these data: R_u = uncompensated resistance, R_{ct} = charge transfer resistance, C_{dl} = double layer capacitance.

The lower double layer capacitance and lower charge transfer resistance indicate less complete coverage for the DMPC adlayers than for the C_{12} SAM. Using eqn. 3-6 to estimate the thickness, however, leads to values that are too small by a factor of *ca*. 10. Using eqn. 3-6 and a dielectric constant of ε = 5,[41] a value somewhat in excess of what is usually assumed,[42] we obtain thicknesses of 5 Å for the C_{12}SH SAM and 2 Å for the DMPC adlayer. The low electrochemical estimate for the adlayer thickness is not surprising given that the dielectric response of the adlayer is an estimate at best and there is some inherent uncertainty in the determination of both *C* and *A*.

We take the ellipsometric values of thickness to be better approximations of the true coverage of the surfaces.

Adlayer morphology. The central issue to be considered is the correct physical and chemical interpretation of the perylene reorientation data, where faster reorientation is observed for perylene imbedded in DMPC interfaces when those interfaces are immersed in water relative to the behavior when the interfaces are exposed to air. There are several possible explanations for these findings. For perylene in the DMPC interface in contact with air, we measure a reorientation time of τ_{OR} = 307±39 ps, consistent with a local viscosity η = 3.9 ± 0.5 cP (Table 3-1). Given that the reorientation of perylene in a lipid *bilayer* is consistent with a local viscosity of *ca*. 10 cP below the gel to fluid phase transition (24°C) and *ca*. 7 cP above the phase transition,[23] our observation of *ca*. 4 cP for perylene in a (sub)monolayer indicates that the DMPC moieties bound to the interface are relatively close in spatial proximity to one another. This finding is consistent with the 52% coverage determined electrochemically.

For the same interfacial assembly immersed in water, we recover a perylene reorientation time constant of τ_{OR} = 130 ± 46 ps, corresponding to η = 1.7 ± 0.6 cP (Table 3-1). The fact that perylene reorients faster in the same interface when it is immersed in water indicates either that the DMPC-rich regions on the interface are experiencing a significant organizational disruption or that perylene is being solvated in some manner by water. We believe the latter explanation to be unlikely given the exceedingly low solubility of perylene in water (~10^{-8} M). If, as is the case for the mixing of water and alkanes, a phase boundary exists at the interface of the water and lipid acyl chains, the question is how the water overlayer alters the lipid acyl chain organization to increase local free volume. If the thickness of the adlayer is decreased, then the lateral area of the

adlayer must be able to compensate for this loss of thickness. It has been shown previously that the combination of certain substrates and priming chemistry give rise to the formation of island-like features on the surface of silica substrates.[20] Because the DMPC adlayer formation on the substrates is dependent upon the priming chemistry,[17-18] it is likely that the DMPC monolayer is aggregated, and a surface coverage of 52% would leave space for inter-island regions. The presence of a water overlayer could, in principle, compress the adlayer, as is suggested by the ellipsometry data (Table 3-2), and depending on the extent of the compression, such a change could either increase or decrease the available free volume within the structure.

Table 3-2: Adlayer ellipsometric thickness and electrochemical coverage.

Substrate	Ellipsometric Thickness (Å)	Electrochemical Coverage (%)
C_{12} SAM	25 ± 6	91
DMPC/Au	48 ± 10	52

Measurements were performed for two different C_{12} thiol/Au SAMs and five different APDMES+ZP+DMPC terminated interfaces on modified gold substrates.

What is not clear from these data is the extent to which the interfacial organization can be controlled by the composition of the overlayer. There is limited experimental latitude in altering the identity of the overlayer because of the solubility of perylene in a number of polar and nonpolar non-aqueous solvents (*e.g.* methanol, cyclohexane). We have added NaCl (several different concentrations) to the aqueous solution in which the interface has been immersed and we find no measurable effect on the reorientation dynamics of perylene. This finding indicates that direct interactions between the chromophore and liquid overlayer are not responsible for our findings. Rather, it is the alteration of the DMPC acyl chain organization by the presence of the water overlayer that mediates the perylene reorientation dynamics. Further, the extent to which the aqueous phase overlayer influences the organization of the lipid acyl chain region is limited because the presence of salt in this solution does not lead to organization in the acyl chain region that is discernibly different than it is for a water overlayer.

We are limited in terms of the information that can be extracted from the reorientation data because we recover single exponential anisotropy decays in all cases. The prolate rotor shape that produces this decay functionality is related to only one Cartesian component of D and the measurement is insensitive to changes in the aspect ratio of the ellipsoidal rotor as a function of local environment. We do consider that the magnitude of the changes we measure in D_z implies significant disruption is associated with immersion of this interface in water. It is not likely that the infiltration of even a significant amount of water into the adlayer would give rise to the observed decrease in effective viscosity. In comparison, the addition of up to 1.6 M ethanol to aqueous solutions containing 100 nm diameter DMPC vesicles produced only modest changes in the viscosity of the lipid acyl chain region and essentially no change in the effective rotor shape of the perylene contained within the bilayer structure.[43] Further experimentation will be required to elucidate in more detail the changes in acyl chain organization that result from exposing bound lipid monolayers to a water overlayer.

3.5 Conclusions

We have investigated the rotational diffusion dynamics of perylene contained within a tethered lipid monolayer. The data show relatively restricted chromophore motion in the lipid adlayer exposed to air and substantially increased motional freedom when the adlayer is immersed in aqueous solution. The central question is how the water overlayer can interact with the lipid monolayer to produce a less restrictive local environment for perylene. The dynamics of the chromophore when the adlayer is immersed in aqueous solution are the same whether sodium chloride is present in the water or not. The decrease in rotational diffusion time constant of perylene in the immersed interface is likely associated with a decrease in the extent of organization

within the (bound) lipid acyl chains. Such a situation would require a net reduction in local density of the acyl chains, and this is feasible in light of electrochemical data that indicate *ca*. 52% coverage of the lipid monolayer. A more detailed understanding of lipid monolayer morphology for both air- and water-exposed systems is required. Ellipsometric and contact angle data suggest a spatially heterogeneous, largely nonpolar interface, but little information is available on the characteristic length scale(s) of any organized regions on the surface. It is possible that future studies using more rigid chromophores with different aspect ratios (*e.g.* DPH)[44] may shed light on the nature of the acyl chain organization in the lipid adlayer, and fluorescence lifetime and anisotropy imaging data may shed light on the characteristic domain sizes seen for these systems.

REFERENCES

REFERENCES

1. Janmey, P. A.; Kinnunen, P. K. J., Biophysical properties of lipids and dynamic membranes. *Trends Cell Bio.* **2006,** *16* (10), 538-546.

2. Klausner, R. D.; Fishman, M. C.; Karnovsky, M. J., Ionophore A23187 disrupts membrane structure by modifying protein-lipid interactions. *Nature* **1979,** *281*, 82-83.

3. Simons, K.; Ikonen, E., Functional rafts in cell membranes. *Nature* **1997,** *387*, 569-572.

4. Kycia, A. H.; Wang, J.; Merrill, A. R.; Lipkowski, J., Atomic force microscopy studies of a floating-bilayer lipid membrane on a Au(111) surface modified with a hydrophilic monolayer. *Langmuir* **2011,** *27*, 10867-10877.

5. Lipkowski, J., Building biomimetic membrane at a gold electrode surface. *Phys. Chem. Chem. Phys.* **2010,** *12*, 13874-13887.

6. Richter, R. P.; Berat, R.; Brisson, A. R., Formation of solid-supported lipid bilayers: An integrated view. *Langmuir* **2006,** *22*, 3497-3505.

7. Kiessling, V.; Tamm, L. K., Measuring distances in supported bilayers by fluorescence interference-contrast microscopy: Polymer supports and SNARE proteins. *Biophys. J.* **2003,** *84*, 408-418.

8. Knoll, W.; Frank, C. W.; Heibel, C.; Naumann, R.; Offenhausser, A.; Ruhe, J.; Schmidt, E. K.; Shen, W. W.; Sinner, A., Functional tethered lipid bilayers. *Rev. Mol. Biotech.* **2000,** *74*, 137-158.

9. Naumann, C. A.; Prucker, O.; Lehmann, T.; Ruhe, J.; Knoll, W.; Frank, C. W., The polymer-supported phospholipid bilayer: Tethering as a new approach to substrate-membrane stabilization. *Biomacromol.* **2002,** *3*, 27-35.

10. Raguse, B.; Braach-Maksvytis, V.; Cornell, B. A.; King, L. G.; Osman, P. D. J.; Pace, R. J.; Wieczorek, L., Tethered lipid bilayer membranes: Formation and ionic reservoir characterization. *Langmuir* **1998,** *14*, 648-659.

11. Seitz, M.; Ter-Ovanesyan, E.; Hausch, M.; Park, C. K.; Zasadzinski, J. A.; Zentel, R.; Israelachvili, J. N., Formation of tethered supported bilayers by vesicle fusion onto lipopolymer monolayers promoted by osmotic stress. *Langmuir* **2000,** *16*, 6067-6070.

12. Seitz, M.; Wong, J. Y.; Park, C. K.; Alcantar, N. A.; Israelachvili, J. N., Formation of tethered supported bilayers via membrane-inserting reactive lipids. *Thin Solid Films* **1998,** *327-329*, 767-771.

13. Wagner, M. L.; Tamm, L. K., Tethered polymer-supported planar lipid bilayers for reconstitution of integral membrane proteins: Silane-polyethyleneglycol-lipid as a cushion and covalent linker. *Biophys. J.* **2000,** *79*, 1400-1414.

14. Fabre, R. M.; Talham, D. R., Stable supported lipid bilayers on zirconium phosphonate surfaces. *Langmuir* **2009,** *25*, 12644-12652.

15. Mayer, L. D.; Hope, M. J.; Cullis, P. R., Vesicles of variable sizes produced by a rapid extrusion procedure. *Biochim. Biophys. Acta* **1986,** *858*, 161-168.

16. Moscho, A.; Orwar, O.; Chiu, D. T.; Modi, B. P.; Zare, R. N., Rapid preparation of giant unilamellar vesicles. *Proc. Nat. Acad. Sci.* **1996,** *93*, 11443-11447.

17. Oberts, B. P.; Blanchard, G. J., Formation of air-stable supported lipid monolayers and bilayers. *Langmuir* **2009,** *25*, 2962-2970.

18. Oberts, B. P.; Blanchard, G. J., Strategies for the growth of self-assembled phospholipid adlayers. *Bioelectrochem.* **2010,** *80*, 10-16.

19. Brzozowska, M.; Oberts, B. P.; Blanchard, G. J.; Majewski, J.; Krysinski, P., Design and characterization of a nocel tether layer for coupling of a bilayer lipid membrane to a surface of gold. *Langmuir* **2009,** *25*, 9337-9345.

20. Horne, J. C.; Blanchard, G. J., Dynamics Within a Single Molecular Layer: Aggregation, Relaxation and the Absence of Motion. *J. Am. Chem. Soc.* **1996,** *118*, 12788-12795.

21. Horne, J. C.; Huang, Y.; Liu, G.-Y.; Blanchard, G. J., The Correspondence Between Layer Morphology and Intralayer Excitation Transport in Zirconium-Phosphonate Monolayers. *J. Am. Chem. Soc.* **1999,** *121*, 4419-4426.

22. Mazur, M.; Krysinski, P.; Blanchard, G. J., Using zirconium-phosphate-carbonate (ZPC) chemistry to immobilize polycyclic aromatic hydrocarbons on boron doped diamond. *Langmuir* **2005,** *21*, 8802-8808.

23. Koan, M. M.; Blanchard, G. J., Gauging the Effect of Impurities on Lipid Bilayer Phase Transition Temperature. *J. Phys. Chem. B* **2006,** *110*, 16584-16590.

24. Lapinski, M. M.; Blanchard, G. J., Interrogating the Role of Liposome Size in Mediating the Dynamics of a Chromophore in the Acyl Chain Region of a Phospholipid Bilayer. *Chem. Phys. Lipids* **2008,** *153* (2), 130-137.

25. Groves, J. T.; Ulman, N.; Cremer, P. S.; Boxer, S. G., Substrate-Membrane Interactions: Mechanisms for Imposing Patterns on a Fluid Bilayer Membrane. *Langmuir* **1998,** *14*, 3347-3350.

26. Hay, C.; Marken, F.; Blanchard, G. J., The Effects of Electrolyte Concentration on the Rotational Dynamics of Resorufin. *J. Phys. Chem. A* **2010,** *114*, 12875-12880.

27. Chuang, T. J.; Eisenthal, K. B., Theory of Fluorescence Depolarization by Anisotropic Rotational Diffusion. *J Chem Phys* **1972,** *57* (12), 5094-+.

28. Jiang, Y.; Blanchard, G. J., Rotational diffusion dynamics of perylene in n-alkanes. Observation of a solvent length-dependent change of boundary condition. *J. Phys. Chem.* **1994,** *98*, 6436-6440.

29. Debye, P., *Polar Molecules* Chemical Catalog Co.: New York 1929; p 84.

30. Hu, C.-M.; Zwanzig, R., Rotational friction coefficients for spheroids with the slipping boundary condition. *J. Chem. Phys.* **1974,** *60* (11), 4354-4357.

31. Perrin, F., Mouvement brownien d'un ellipsoide (I). Dispersion dielectrique pour les molecules ellipsoidale. *J. Phys. Radium* **1934,** *5*, 497.

32. Perrin, F., Mouvement Brownien d'un ellipsoide (II). Rotation libre et depolarisation des fluorescences. Translation et diffusion de molecules ellipsoidales. *J. Phys. Radium* **1936** *7*,1-11.

33. Edward, J. T., Molecular volumes and the Stokes-Einstein equation. *J. Chem. Ed.* **1970,** *47* (4), 261-270.

34. Lide, D. R., *CRC Handbook of Chemistry and Physics*. CRC Press, Inc.: Boca Raton, FL, 1990-1991; Vol. 71, p 8-39.

35. Garcia-Raya, D.; Madueno, R.; Sevilla, J. M.; Blazquez, M.; Pineda, T., Electrochemical characterization of a 1,8-octanedithiol self-assembled monolayer (ODT-SAM) on a Au(111) single crystal electrode. *Electrochim. Acta* **2008,** *53*, 8026-8033.

36. Pletcher, D., *A First Course in Electrode Processes, 2nd Edition*. The Royal Society of Chemistry: Cambridge, UK, 2009.

37. Randles, J. E. B., Kinetics of Rapid Electrode Reactions. *Disc. Faraday Soc.* **1947,** *1*, 11-19.

38. Randles, J. E. B., Kinetics of rapid electrode reactions. Part 2. - Rate constants and activation energies of electrode reactions. *Trans. Faraday Soc.* **1952,** *48*, 828-832.

39. Randles, J. E. B.; Somerton, K. W., Kinetics of rapid electrode reactions. Part 3. - Electron exchange reactions. *Trans. Faraday Soc.* **1952,** *48*, 937-950.

40. Randles, J. E. B.; Somerton, K. W., Kinetics of rapid electrode reactions. Part 4. - Metal ion exchange reaction at amalgam electrodes. *Trans. Faraday Soc.* **1952,** *48*, 951-955.

41. Natan, A.; Kuritz, N.; Kronik, L., Polarizability, susceptibility and dielectric constant of nanometer-scale molecular films. A microscopic view. *Adv. Funct. Mat.* **2010,** *20*, 2077-2084.

42. Akkerman, H. B.; Naber, R. C. G.; Jongbloed, B.; van Hal, P. A.; Blom, P. W.; de Leeuw, D. M., Electron tunneling through alkanedithiol self-assembled monolayers in large-area molecular junctions. *Proc. Nat. Acad. Sci.* **2007,** *104*, 11161-11166.

43. Pillman, H. A.; Blanchard, G. J., Molecular Consequences of Ethanol Incorporation into Phospholipid Bilayers. *J. Phys. Chem. B* **2010,** *114*, 3840-3846.

44. Mitchell, D. C.; Litman, B. J., Effect of Cholesterol on Molecular Order and Dynamics in Highly Polyunsaturated Phospholipid Bilayers. *Biophys. J.* **1998,** *75*, 896-908.

CHAPTER 4: USING DIFFUSIONAL MOTION TO GAUGE INTERFACIAL ADHESION OF SUPPORTED ALKYL PHOSPHONATE MONOLAYERS

Adapted with permission from:

S. M. Baumler, Thomas M. Reidy, and G. J. Blanchard; Diffusional motion as a gauge of fluidity and interfacial adhesion. Supported alkylphosphonate monolayers. Journal of Colloid and Interface Science (2016) 145–155.

4.1 Abstract

Diffusion measurements were used to gauge the fluidity and surface binding properties of a molecular monolayer. The monolayer film consists of octadecyl-1-phosphonic acid (ODPA) and controlled amounts of a lyso-phosphatidic acid tagged with the fluorescent probe BODIPY (BLPA). The monolayer films were formed using a Langmuir-Blodgett (LB) trough and deposited onto a glass slide. Monolayer morphology was characterized during film formation using Brewster angle microscopy (BAM). Fluorescence Recovery After Photobleaching (FRAP) microscopy was used to measure translational diffusion of BLPA and Fluorescence Anisotropy Decay Imaging (FADI) was used to measure rotational diffusion of the BLPA chromophore. These results provide information on the motional freedom of the probe and, importantly, on the strength of interaction between the probe and the support. Compositional variations in the monolayer give rise to changes in constituent dynamics that reflect intermolecular interactions.

4.2 Introduction

Monolayer films have been examined extensively over the past half-century because of their ability to alter the properties of an interface for a desired purpose. A single layer of molecules can be used to change the polarity of a surface, or to mediate electron transfer, for example. With technology requiring ever smaller dimensions, it is important to gain molecular-level control over not only the chemical identity of interfacial layers, but also to be able to control their physical properties.[1] We have undertaken the examination of a representative interfacial monolayer with the aim of quantitating the fluidity and adhesion of the adlayer to the interface. Understanding interfacial dynamics is a prerequisite to controlling these properties.

One family of monolayer films that has received extensive research attention is self-assembled monolayers (SAMs) of alkanethiols on gold.[2-13] That work has demonstrated the delicate balance of forces required to produce a monolayer and at the same time many practical applications have stemmed from this chemical system, including patterned interfaces for lithographic and other applications.[14-17] In addition to the alkanethiol SAMs, Langmuir-Blodgett (LB) films have enjoyed wide use.[18-21] The interactions between the amphiphilic film constituents and the supporting surface are fundamentally different for the two systems, with physical robustness favoring alkanethiol SAMs.[12-13] LB films, however, allow for greater control over composition and ordering, and also produce films that exhibit controllable mobility.[22] This latter feature is important especially in cases where films benefit from defect mitigation or the ability to adapt to interfacial features. Both approaches to monolayer film formation allow complex molecules to form well-ordered two-dimensional assemblies. For both systems, an understanding of the interrelationship between the nanoscale heterogeneities at the support surface and defects within the film itself, and their effect(s) on the long-range order of the films, remains to be developed fully.

Previous work by the Talham group has shown that films of considerable ordering and structure can be prepared using LB methodology using organophosphonic acids with divalent metals at the appropriate subphase pH.[23-24] We are concerned with the introduction of structural heterogeneities into an amphiphilic monolayer structure, and how the film dynamics and organization change with the amount of "defect" species present. We use octadecylphosphonic acid (ODPA) as the amphiphile for the formation of the LB film and a fluorophore-tagged lysophospholipid (BLPA) as the dissimilar defect molecule. Because BLPA contains the BODIPY chromophore, it also serves as the optical probe in this work. We have chosen to use phosphonate

LB films in this work because, ultimately, there is greater structural versatility and range of dynamics available with phosphonates than the corresponding carboxylates.[23-29]

The BLPA probe has been used to measure the diffusional properties on both short (molecular) and long (μm) length scales using rotational- and translational-diffusion measurements, respectively. Comparison of these two physical quantities affords quantitative information on the role of the defect molecule in mediating organization within the film and on the strength of interaction between the film and the support. While the study of dynamics in LB and related films is not new,[22, 30-34] our approach to comparing diffusional processes across a range of length scales is both novel and information-rich. The forces binding the adlayer to the interface were found to exceed those expected for simple physisorption, and more closely approximate the strength of hydrogen bond enthalpies in water. The ability to quantitate such interactions opens the door to better understanding how to control the properties of supported monolayer films and, simultaneously, provides direct information on the molecular motion that characterizes these interfaces.

4.3 Experimental

Materials. Octadecylphosphonic acid (ODPA) ($C_{18}H_{39}O_3P$, 97% purity) (Fig. 4-1), barium chloride dihydrate ($BaCl_2 \cdot 2H_2O$, Reagent Grade), and tetrahydrofuran (THF, 99.9%) were obtained from Sigma Aldrich and used as received. The chromophore used in these studies was 1-(12-[4-(dipyrromethene boron difluoride) butanoyl] amino) dodecanoyl-2-hydroxy-*sn*-glycero-3-phosphate (ammonium salt) (BLPA) (TopFluor Lyso PA, >99%, Avanti Polar Lipids) (Fig. 4-1). Water (18 MΩ-cm) was obtained from a Milli-Q Plus water purification system and used for all experiments.

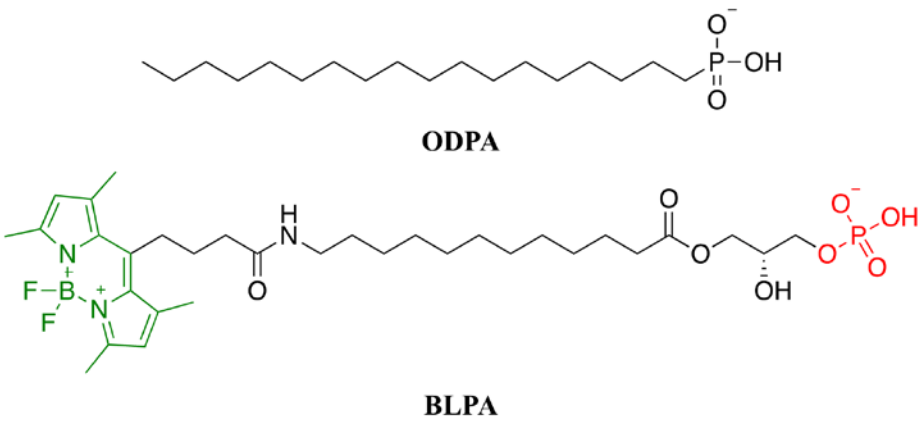

BLPA

Figure 4-1: Chemical structures of the components used in the formation of the LB film. Octadecylphosphonic acid (ODPA), and 1-(12-[4-(dipyrromethene boron difluoride) butanoyl] amino) dodecanoyl-2-hydroxy-*sn*-glycero-3-phosphate (ammonium salt) (BLPA).

Langmuir Monolayer Preparation and LB Film Deposition. The barium ODPA (Ba-ODPA) LB films were prepared by the Langmuir-Blodgett technique.[18-20] We used a large Teflon® Langmuir trough (KSV Nima) equipped with a dipping mechanism and a platinum Wilhelmy plate attached to a balance with an automated feedback system to maintain a constant surface pressure during film transfer. Herein, we use the term 'Langmuir monolayer' to refer to a monolayer at the air-water interface and LB film to refer to the monolayer transferred to the solid support.

The glass substrates were standard microscope slides (1 mm × 25 mm × 75 mm, Globe Scientific) and were placed in a piranha solution ($1H_2O_2$:$3H_2SO_4$, *Caution! Strong oxidizer!*) for 30 min prior to transfer to the LB-trough for dipping. After cleaning, the substrates were rinsed with water and placed in a covered beaker containing water until they were used for deposition. To produce stable monolayers the subphase was a 5 mM $BaCl_2$ aqueous solution. The subphase pH was measured to be 5.4. The temperature of the subphase was maintained at 23° ± 0.1° C using a circulating water bath (Fisher) attached to the trough. For each dipping experiment 150 μL of a 1 mg/mL ODPA in THF solution was used for monolayer spreading.

Solutions containing 5 mol% BLPA (BLPA-5) and 10 mol% BLPA (BLPA-10) were prepared by mixing appropriate amounts of the ODPA solution and 1 mg/mL BLPA in THF solution and mixing for 30 sec by hand. The amount of solution spread on the surface was calculated to give an initial surface pressure π below 1 mN/m. During spreading, care was taken to prevent the spreading needle from touching the surface as well as preventing the surface pressure π from rising above 0.5 mN/m in order to ensure complete spreading. After spreading, the monolayer was allowed to equilibrate for 30 min to ensure solvent evaporation and monolayer relaxation, before the barriers were moved inward at 5 mm/min (mean molecular area compression of <1 $Å^2$/min) to compress the surface monolayer to the pressure used for dipping (30 mN/m). The compressed monolayer was allowed to equilibrate for 15 minutes before it was transferred onto the glass slide. The monolayer was transferred (upstroke) at a dipping speed of 5 mm/min while keeping the pressure constant, covering a total area of 35mm x 25mm on each side of the glass slide. The coated slides were dried in air for at least 1 hr. before FRAP and FADI measurements were made.

Brewster angle microscopy. We characterize the morphology of the monolayers formed on the LB-trough using a Brewster angle microscope (BAM, Accurion UltraBAM). This instrument is characterized by 2 μm spatial resolution and an adjustable angle of incidence. The laser wavelength used for BAM measurements is 653 nm (diode laser) and the instrument is operated using software supplied by the manufacturer.

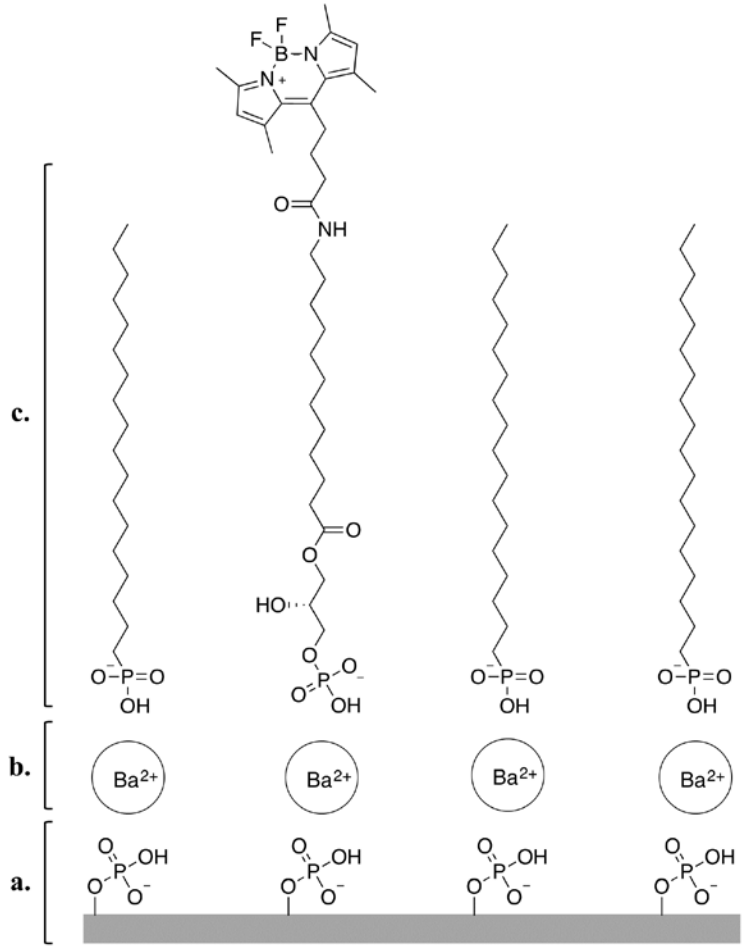

Figure 4-2: Idealized diagram of the prepared ODPA/BLPA Langmuir film. The films are composed of the (a.) phosphorylated silica support, (b.) barium ion layer, and (c.) ODPA/BLPA layer.

Steady State Fluorescence Measurements. Excitation and emission spectra of the BLPA chromophore in THF was collected using a Jobin Yvon Spex Fluorolog-3 spectrometer. Emission spectra were collected for BLPA in THF as well as the 5 mol% and 10 mol% samples to verify the presence and band positions of the incorporated BLPA chromophore. Spectral resolution was set to 1 nm for both the excitation and emission monochromators for all measurements.

Optical ellipsometry. Optical ellipsometry measurements were performed to determine LB film thickness using a J. A. Woollam Co., Inc. model EC270 spectroscopic ellipsometer with a fixed angle (75°) and wavelength range of 400-1100 nm. The EC270 is equipped with 75W Xenon lamp source and diode array detector to simultaneously detect 44 wavelengths. The LB films were prepared on single crystal (100) silicon wafers (University Wafer, Boston, MA). The fitting for the ODPA layer thickness was accomplished by modeling the silicon substrate as adlayers of silicon dioxide with fixed thickness and refractive index of 1.46, and a generic organic film layer with a refractive index of 1.5. The silicon dioxide adlayer was determined on a freshly cleaned substrate and measured to be 17 ± 1 Å.

Fluorescence Recovery After Photobleaching (FRAP) Measurements. FRAP measurements were conducted on a Nikon $C2^+$ confocal laser scanning microscopy system consisting of a Nikon Eclipse Ti-E inverted microscope with a confocal scanning system (Nikon Ti-S-CON). The BLPA was excited with the 488 nm line of an Ar^+ laser (Nikon Lu-N4), and emission was detected at 525 nm using a standard PMT detector (Nikon C2-DU3). A 10x objective lens was used for the LB films. Initial intensities (I_0) were measured for a minimum of 10 s. The bleaching time was set to 5 s, and the recovery signal after photobleaching was collected over a minimum of 6 min. The recovery signals, $I_{frap}(t)$, were normalized using eqn. 4-1, where I_{bleach} is the intensity immediately following photobleaching, I_0 is the maximum intensity during the 15 s prior to photobleaching, and $I_{norm}(t)$ is the calculated normalized intensity.

$$I_{norm}(t) = \frac{I_{frap}(t) - I_{bleach}}{I_0 - I_{bleach}} \qquad 4\text{-}1$$

A freshly prepared LB film was placed above the objective and approximately 100 μL of milliQ water was added to a random location of the film. Five measurements were made within the water

overlayer on each side of a slide, representing a total of 10 measurements per slide, over 6 slides. The translational diffusion constant (D_T) and percent mobility were obtained by fitting the normalized data to the Ellenberg equation (eqn. 4-2),[35]

$$I(t) = I_{final}\left[1-\left(\frac{w^2}{w^2+4\pi D_T t}\right)^{1/2}\right] \qquad 4\text{-}2$$

I_{final} represents the fluorescence intensity in the photobleached region at times greater than 5 min, w is the diameter of the photobleached spot (10 μm), and D_T is the translational diffusion constant ($\mu m^2/s$). Due to normalization method (eqn. 4-1), I_{final} is the fractional mobility of BLPA in the LB film. The recovery time for the photobleach ($\tau_{1/2}$) is defined as the time it takes for the depletion recovery to reach 50% of the final intensity (eqn. 4-3),

$$\tau_{1/2} = \frac{0.75w^2}{\pi D_T} \qquad 4\text{-}3$$

Fluorescence Anisotropy Decay Imaging (FADI) Measurements. The instrument used to acquire fluorescence anisotropy decay images has been described previously.[36] Briefly, the instrument is based on an inverted microscope optical configuration (Nikon Eclipse Ti−U). All images were collected using a 10x microscope objective. Time-resolved data collection is achieved using the confocal scanning unit (Becker & Hickl DCS-120) attached to an output port of the microscope and is controlled by a galvo-scanning drive unit (Becker & Hickl GDA- 120). The confocal scanning unit (DSC-120) is equipped with a polarizing beam splitter and two avalanche photodiode detectors (ID-Quantique ID100). Polarized fluorescence transients are acquired using time-correlated single photon counting (TCSPC) detection electronics (Becker & Hickl SPC-152, PHD-400N reference diode) and were used to determine the induced orientational anisotropy decay function (eqn. 4-4).

The light source for these experiments was a synchronously pumped cavity dumped dye laser (Coherent 702) excited by the output of a passively mode locked Nd:YVO_4 laser (Spectra Physics Vanguard). The dye laser is cavity dumped (Gooch and Housego 64389.5-SYN-9.5−1 cavity dumper driver) to control the repetition rate. The dye laser output is characterized by *ca.* 5 ps pulses at a repetition rate of 4 MHz (250 ns interpulse spacing). For this work the dye laser output was set to 490 nm using Stilbene 420 dye (Exciton) and the emission collection window was 535 ± 30 nm, determined by a band pass filter in the confocal scanning unit. These wavelengths were selected based on the excitation and emission spectra of the BLPA chromophore (Fig. 4-6, A.).

Supported LB films were placed above the microscope objective and approximately 100 μL of Milli-Q water was added to a random location of the film. Two measurements were made within the hydrated region on each side of the slide, representing a total of 4 measurements per slide over 4 slides. Each measurement produced a 256x256 pixel^2 image with 256 time points from both the parallel and perpendicular channels. The images were binned to average the data over a 4 pixel x 4 pixel region. Anisotropy decay time constants were obtained by fitting the induced anisotropy decay equation, which is calculated from the averaged polarized transients (eqn. 4-4):

$$R(t) = \frac{I_{\parallel}(t) - I_{\perp}(t)}{I_{\parallel}(t) + 2I_{\perp}(t)} \qquad 4\text{-}4$$

The anisotropy decay time constant (τ_{HR}) or can be determined by fitting *R(t)* to eqn. 4-5, which is derived from the hindered rotor model.[37-38]

$$R(t) = R(\infty) + \left(R(0) - R(\infty)\right)\exp\left(-t/\tau_{HR}\right) \qquad 4\text{-}5$$

The terms $R(0)$ and $R(\infty)$ are the zero- and infinite-time anisotropies, respectively, and the term τ_{HR} is the anisotropy decay time constant. We consider the physical significance of these data below.

4.4 Results and Discussion

We are concerned with the fundamental properties of LB films. These include the stability and fluidity of the film as a function of how it was formed, and the role that probe molecules may play in mediating film organization and dynamics. We use Langmuir isotherms (π/A) to examine changes in the monolayer density as a function of applied pressure, ionic strength of the subphase, and the addition of selected amounts of BLPA. We use a suite of optical techniques to evaluate the morphology (BAM) and dynamics (FADI, FRAP) of the LB films as a function of system conditions. We consider the information content of these data below, focusing first on the role of subphase composition on Langmuir monolayer properties.

Effect of subphase ionic strength on ODPA Langmuir monolayer morphology. Surface-pressure vs. area isotherms (π/A-isotherms) have been acquired for monolayers prepared over an aqueous subphase containing no ionic constituents and a subphase containing 5 mM $BaCl_2$ (Fig. 4-3, above). BAM images were collected at 5mN/m surface pressure increments for each sample. The isotherm for the monolayer formed on the water subphase consists of a sharp increase in pressure at a mean molecular area of 21 $Å^2$ and a characteristic collapse of the monolayer at *ca.* 62 mN/m. For the subphase containing 5 mM $BaCl_2$, the π/A-isotherm takes a different form. The isotherm does not begin to exhibit a significant increase in pressure until *ca.* 18 $Å^2$/molecule, has a mean molecular area of 13 $Å^2$, and the slope is more shallow (11 mN/m/$Å^2$) compared to the

isotherm of the monolayer formed on the water subphase (16 mN/m/Å^2). Additionally, the Ba^{2+}-containing monolayer does not exhibit a collapse at high pressure similar to the monolayer formed on the water subphase. Rather, the monolayer formed on the $BaCl_2$-containing subphase maintains a constant pressure at *ca.* 60 mN/m with decreasing surface area. BAM images of the two monolayers reveal differences beginning at formation, before any compression occurs (Figs. 4-3 A, D). The monolayer formed on the water surface exhibits fluid regions with small domain ordering present as the white elliptical/circular regions with smaller holes throughout. The monolayer formed with $BaCl_2$ in the subphase exhibits larger island-like regions with dark domain boundaries. Upon compression of the monolayer on the water subphase, the images appear uniform with small darker lines throughout, up to the point of collapse, when bright lines and cracks begin to appear (Figs. 4-3, C, F). The monolayer formed on the subphase containing $BaCl_2$ exhibits scattered bright islands, which do not appear to change in size and/or shape upon compression; these island regions appear to reorganize to fill in the liquid regions with increasing pressure. The Talham group has shown previously that the formation of crystalline Ba/ODPA monolayers is highly pH dependent, and can be formed around pH 8-9.[23] We attribute much of the heterogeneity within these BAM images to be due the subphase pH being lower than the optimal pH for deposition. Ellipsometric thickness measurements after deposition onto the glass slides confirm thicknesses consistent with a monolayer (27 ± 1 Å).[29]

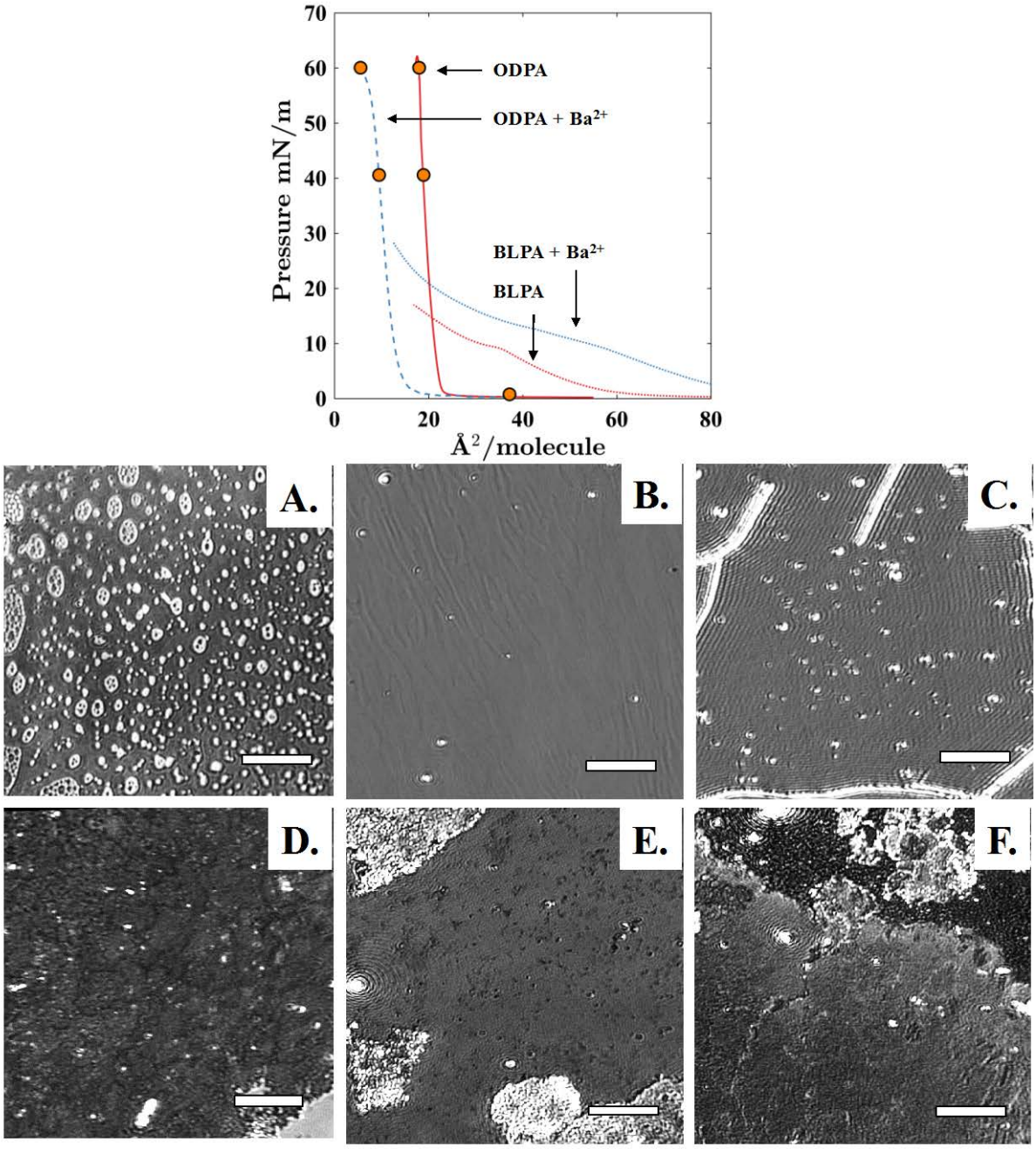

Figure 4-3: Above: π/A-isotherm of ODPA on an aqueous subphase (red solid) and with a 5 mM Ba^{2+} subphase (blue dash). π /A-isotherm of BLPA on an aqueous subphase (red dot) and with a 5 mM Ba^{2+} subphase (blue dot). The temperature for the subphase was 23 °C and pH = 5.4. The monolayers were compressed at a rate of 0.8 Å²/min. Orange circles represent pressures at which BAM images (A–F) were taken. Below: Images A-C are of ODPA on an aqueous subphase. Images D-F are of ODPA on an aqueous subphase containing 5 mM $BaCl_2$. Scale bars represent 100 μm.

The introduction of ionic character into the subphase allows for two phenomena to occur. Increasing ionic strength is known to stabilize the condensed phase allowing for the crystal structure of the long-chain aliphatic acids to be maintained during transfer to the glass support.[39] Through charge compensation, the Ba^{2+} cation would allow the negatively charged polar phosphonic acid headgroups to pack more closely than they would in water at a pH above the pK_a(s) of the headgroup. Due to the change in the headgroup spacing, it is expected that the tilt angle of the aliphatic chains will be different for deposition on the two subphases,[40] and our experimental findings are consistent with this expectation.

Effect of Increasing BLPA Concentration on ODPA Langmuir monolayer Morphology. π/A-isotherms have also been acquired for monolayers prepared over an aqueous subphase containing 5 mM $BaCl_2$ at two different BLPA concentrations (Fig. 4-4, Above). BLPA-5 increases the mean molecular area of pure ODPA from 13 $Å^2$ to 25 $Å^2$. For BLPA-10 the mean molecular area decreases from 25 $Å^2$ for BLPA-5 to 17 $Å^2$. The slopes of the isotherm curves increase with increasing BLPA concentration, from 11 mN/m/$Å^2$ for pure ODPA, to 13 mN/m/$Å^2$ for BLPA-5, and 20 mN/m/$Å^2$ for BLPA-10. The decrease in mean molecular area and increase in slope correlated with the increase in BLPA concentration can be explained in the context of an increased packing density of the BLPA through phase segregation.

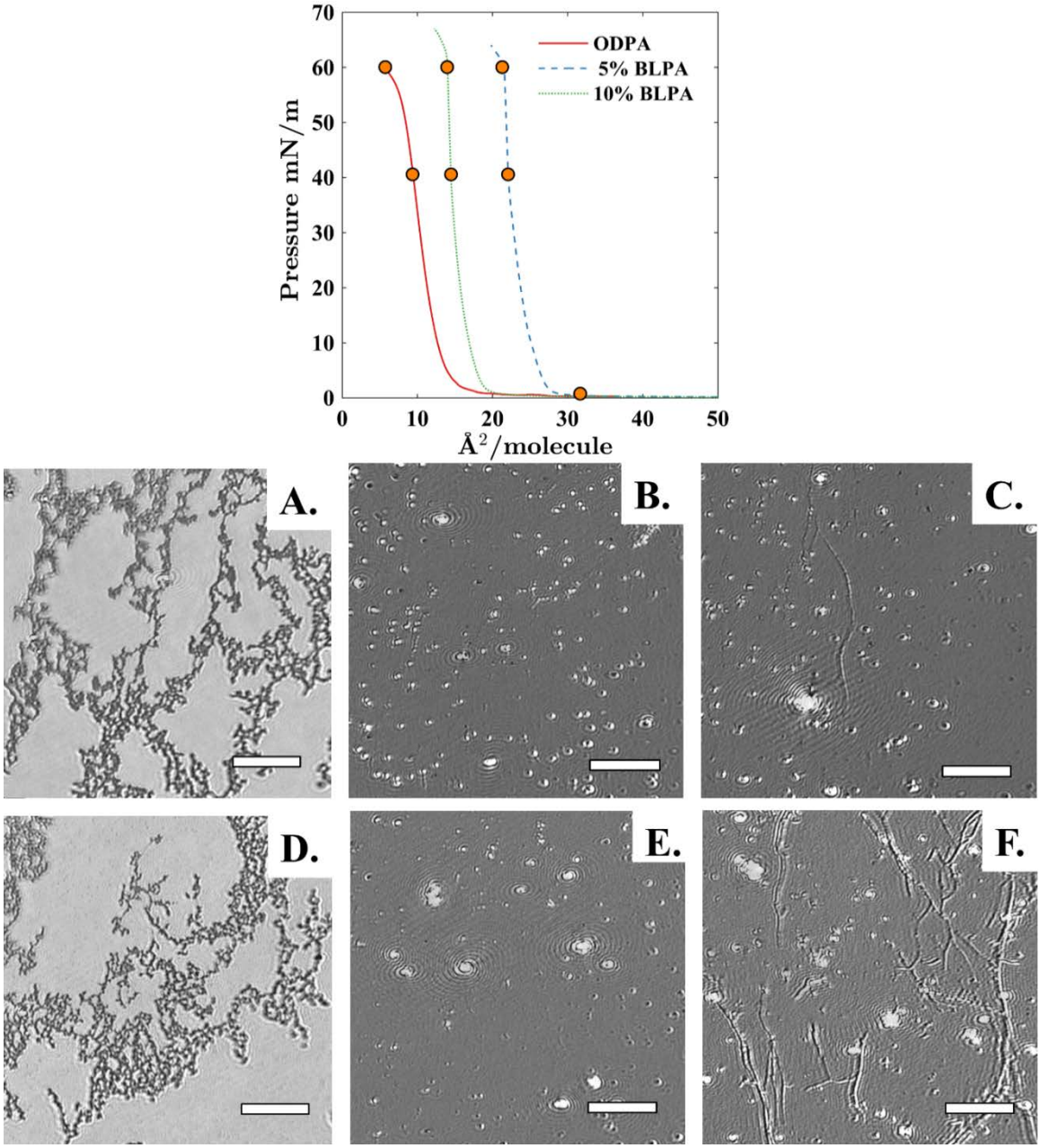

Figure 4-4: Above: π/A-isotherm of the two component monolayers containing ODPA and BLPA on an aqueous subphase with a Ba^{2+} concentration of 5 mM, and 0 mol% BLPA (red solid), 5 mol% (blue dash), and 10 mol% (green dot). The temperature for the subphase was 23 °C and pH = 5.4. The monolayers were compressed at a rate of 0.8 Å²/min. Orange circles represent pressures at which BAM images (A-F) were taken. Below: Images A-C contain ODPA and 5 mol% BLPA, images D-F contain ODPA and 10 mol% BLPA. Images at 0 mol% BLPA are presented in Fig. 4-3 (D-F). Scale bars represent 100 μm.

The mean molecular areas derived from the data shown in Fig. 4-3 were found to be lower than those reported previously.[23] We attribute the rise of the isotherms at values lower than expected to several possible causes. The first is due to the solvent system used during application of the monolayer. ODPA was found to dissolve in THF at concentrations as high as 1 mg/mL and BLPA also exhibited the requisite solubility in this solvent. As a consequence of this solvent choice, the miscibility of the subphase with THF gave rise to the loss of a finite amount of material at the subphase surface during deposition, leading to lower than expected mean molecular areas (Fig. 4-5).

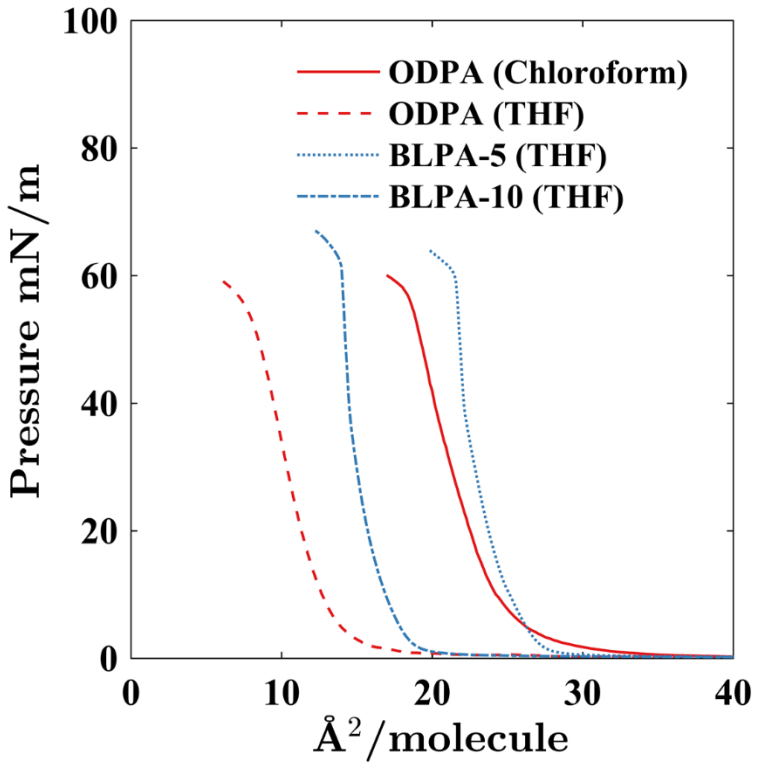

Figure 4-5: π/A-isotherm of the two component monolayers containing ODPA and BLPA on an aqueous subphase with a Ba^{2+} concentration of 5 mM, and 0 mol% BLPA (100% ODPA) (red dash), 5 mol% (blue dot), and 10 mol% (blue dash-dot) dissolved in THF when applied to trough. The application of ODPA when dissolved in chloroform at 0.2 mg/mL and added under similar conditions is shown (red solid).

The second possible reason is due to the solubility of the BLPA chromophore in the subphase at increasing pressures (Fig. 4-3). When comparing the pure BLPA on water to pure BLPA on the barium chloride sub-phase, the addition of ionic character improves the formation of a stable monolayer slightly, likely by decreasing the solubility of the BLPA (Fig. 4-3).

BAM images of the monolayer without BLPA formed with $BaCl_2$ in the subphase are shown in Fig. 4-4. The addition of 5% BLPA creates two distinct regions (Figs. 4-4, A, D). Upon compression, both BLPA-5 and BLPA-10 exhibit bright cracks at the collapse pressure (Figs. 4-4, C, F). BLPA-5 contains *ca*. 50% more bright regions than BLPA-10, and the bright regions of the BLPA-5 are, on average, *ca*. 20% smaller than those in BLPA-10. We believe these bright spots are aggregates of BLPA dispersed throughout the monolayer and the differences in quantity of bright regions correlates well with the two-fold increase in amount of BLPA present.

Formation of Aggregates at Higher BLPA Concentrations. The steady state absorbance and emission spectra of BLPA in THF, as well as the emission for BLPA-5 and BLPA-10 LB films are shown in Fig. 4-6, A. Increasing the concentration of BLPA in the LB films causes a bathochromic shift of the emission spectrum of ~6 nm. The difference in band shift between the BLPA-5 and BLPA-10 films is ~4 nm.

The BODIPY chromophore is known to form either H- or J- aggregates,[41-44] depending on the environment and functionalities attached to the BODIPY chromophore.[45-48] We attribute the slight bathochromic shift to the formation of J-aggregates in these films. The peak shift, whether bathochromic or hypsochromic, depends on the angle between the constituent chromophore transition dipole moments (Fig. 4-6, B). J-aggregation is characterized by the angle between the constituent transition moments, $\gamma \leq 54.7°$. As the angle between the BODIPY transition moments

approaches zero, the J-aggregates are characterized by a head-to-tail orientation, while H-aggregates are characterized by a transition moment angle $\gamma > 54.7°$, where the transition dipole moments are stacked face-to-face or there is considerable π-π stacking in the aggregate. We attribute the observed spectral shift to aggregation, with the increased disorder induced by the BLPA-10 films decreasing the angle between the two chromophores and allowing for a more head-to-tail configuration.

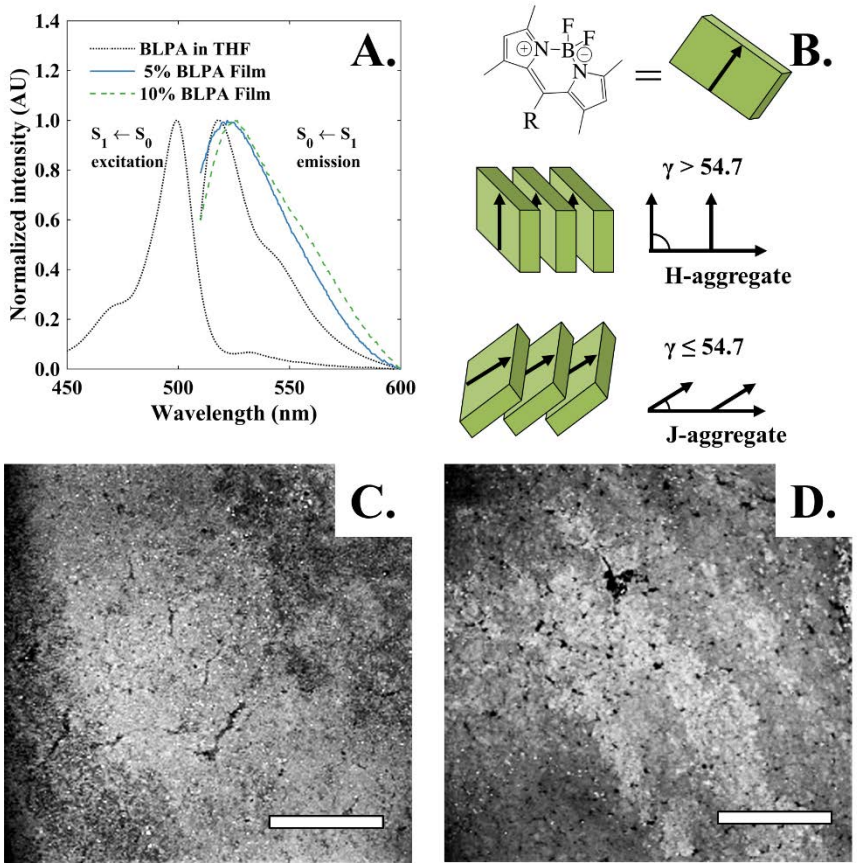

Figure 4-6: (A.) Emission spectra of the two component LB films. BLPA-5 (blue solid), and BLPA-10 (green dash). Absorbance and emission spectra of BLPA in THF (black dot). All spectra were normalized to unity. Schematic representation of a structural description of H- and J-aggregates of the BODIPY chromophore (B.) Steady state fluorescence images of BLPA-5 are shown in (C.) and BLPA-10 in (D.). Scale bars represent 500 µm.

Steady state fluorescence images of BLPA-5 and BLPA-10 are shown in figure 4-6, C and 4-6, D, respectively. Increasing the concentration of BLPA in the LB films reveals an increase in

pinhole defects and increased heterogeneity, evidenced by the bright striped regions the BLPA-10 image (Fig. 4-6, D). The BLPA-5 image shows a considerable number of bright regions throughout the image. We attribute these bright spots to regions of BLPA aggregation. There is considerably less intense spotting in the BLPA-10 image. We attribute the decrease in spotting intensity to be due to two main factors. First, at higher concentrations the contrast between the BLPA aggregates and the larger film area decreases due to the overall increased presence of BLPA chromophore. Second, BLPA-5 shows larger regions of uniform intensity compared to BLPA-10 with alternating regions of high and low intensity (striping). This observation suggests not only that more BLPA is present, but BLPA may phase segregate into regions where the film exhibits different domain organization.

Translational Diffusion Slowed by Aggregation at Increased BLPA Concentrations. Macroscopic translational diffusion of the ODPA/BLPA LB films was measured using FRAP. FRAP is sensitive to the organization of the LB film. FRAP data for both BLPA-5 and BLPA-10 films are shown in Fig. 4-7 and Table 4-1.

Table 4-1: Translational diffusion constants (D_T), Mobile fraction %, and Recovery speed ($\tau_{1/2}$) determined for the 5 mol% and 10 mol% substrates from FRAP measurements.

Molar % BLPA	Mobile Fraction (%)	D_T^{eff} ($\mu m^2/s$)	$\tau_{1/2}$ (s)
5%	16 ± 4	0.26 ± 0.09	90 ± 30
10%	23 ± 4	0.09 ± 0.02	250 ± 50

Errors are ± 1σ for a minimum of 5 individual determinations on each substrate, over a minimum of 6 substrates. 5% and 10% values were determined to be significantly different to 95% confidence.

The average translational diffusion constant of the BLPA-5 film is 0.26±0.09 $\mu m^2/s$ with a mobile fraction of 16±4 %. The BLPA-10 film gives D_T = 0.09±0.02 $\mu m^2/s$ with a mobile fraction of 23±4 %. The time constant for recovery of the BLPA-5 film is 90±30 s and for the BLPA-10 film

τ = 250±50 s. These data were determined from the raw time-scans by fitting to Eqs. 4-2 and 4-3 . The three-fold decrease in both D_T and τ indicate that translational motion of BLPA-10 is more hindered, and we assert that the reason for this is the aggregation of chromophores (*vide infra*). We consider the energetic implications of these findings below.

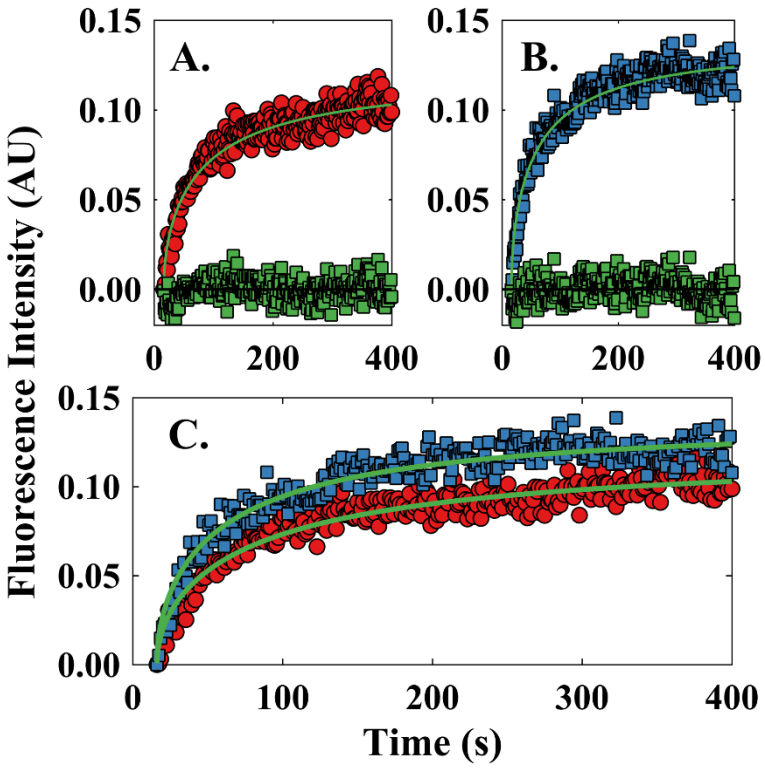

Figure 4-7: FRAP recovery of the BLPA chromophore in (A.) BLPA-5 (red) and (B.) BLPA-10 (blue). The green lines represent best-fit lines using the Ellenberg equation with residuals plotted below. (C.) Comparison between the BLPA-5 and BLPA-10 curves is shown. All FRAP curves were normalized prior to fit.

Rotational Diffusion and Information Content. FADI measurements have been performed for both BLPA-5 and BLPA-10 LB films (Table 4-2). Typical fluorescence anisotropy decays for the films are shown in Fig. 4-8. To gain greater insight into the effect of increased BLPA concentration on the surface structure and dynamics, we

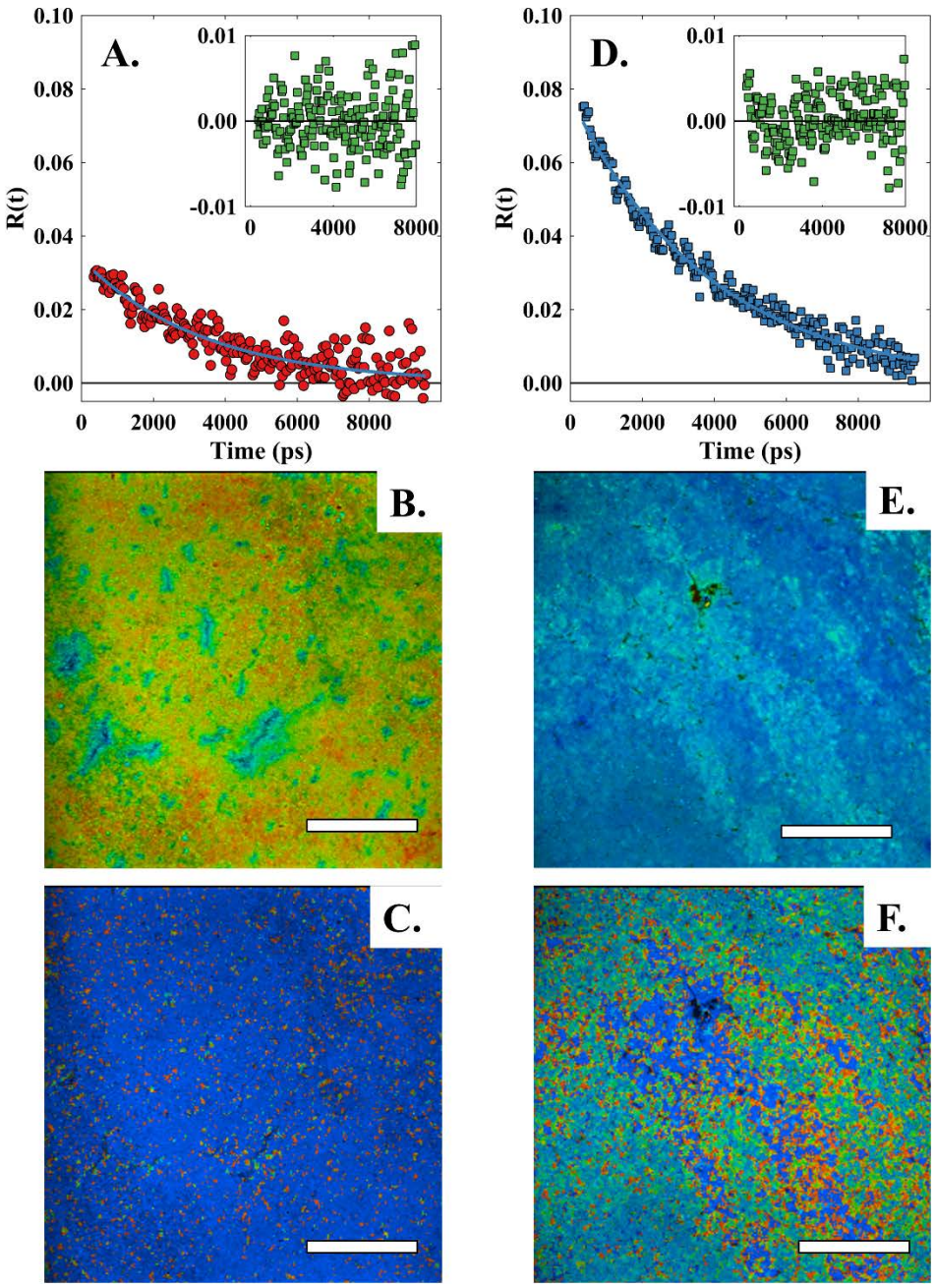

Figure 4-8: Typical experimental anisotropy decay functions for the BLPA-5 (A.) and BLPA-10 (D.) LB films with residuals of best fit inset are shown. Fluorescence transients were fit to determine the fluorescence lifetime shown in (B., BLPA-5) and (E., BLPA-10). The colors shown represent the lifetime value at a given pixel, with blue being short lifetimes and red being longer lifetimes. Fluorescence anisotropy decay time constant images are shown in (C., BLPA-5) and (F. BLPA-10). The colors shown are set by the imaging software, with blue being short decay time constants and red being longer decay time constants. All images were acquired using a 10x microscope objective. Scale bars represent 500 μm.

have acquired 256x256 pixel images of the fluorescence lifetime and anisotropy decay of the films (Figs. 4-8, B-C, E-F). These data provide qualitative insight into how structural heterogeneity is induced at higher BLPA concentrations. BLPA-10 films have characteristically shorter average fluorescence lifetimes and longer anisotropy decay time constants. The shorter chromophore lifetime for the BLPA-10 films suggests quenching. We assert that the fluorescence quenching is due to the formation of BODIPY aggregates, consistent with the steady-state emission shift reported for these films (*vide supra*). The anisotropy decay images for the BLPA-10 films show both a broader distribution and longer anisotropy decay time constants than are seen for the BLPA-5 films. These data are consistent with chromophore aggregation at higher concentration.

Table 4-2: Reorientation time (τ_{HR}), rotational diffusion constant (D_{ROT}), and rotational wobbling constant (D_W) determined by the local Environment of BLPA in a Ba-ODPA LB film.

Molar % BLPA	τ_{HR} (ps)	D_{ROT} (MHz)	D_w (MHz)
5%	3,400 ± 220	49.0 ± 3.1	30.9 ± 2.0
10%	4,000 ± 200	41.8 ± 2.1	26.5 ± 1.3

Errors are ± 1σ for a minimum of 2 individual scans over an area of μm^2 on each substrate, over a minimum of 4 substrates. 5% and 10% rotational values were determined to be significantly different to 90% confidence.

To obtain quantitative information on the chromophore local environment, the images were analyzed as described above to obtain the average anisotropy decay time constant by fitting the collected fluorescence anisotropy decay transients to eqn. 4-5. The reorientation times for the films were τ_{HR} = 3,400 ± 220 ps and 4,000 ± 200 ps for the BLPA-5 and BLPA-10 films, respectively. The LB film under investigation here contains a tethered chromophore, so the hindered rotor model is appropriate (Eqs. 4-5 and 4-6).[37-38]

$$\tau_{HR} = \frac{7\theta_0^2}{24 D_W}$$

$$\theta_0 = \cos^{-1}\left(0.5\left[8\left(\frac{R(\infty)}{R(0)} \right)^{1/2} + 1 \right]^{1/2} - 0.5 \right) \qquad 4\text{-}6$$

In this model, the (fast) chromophore motion is constrained by the medium surrounding it and its tether to the support surface. Rotational motion can be described as occurring in a cone of semi-angle θ_0, and there will be a diffusive "wobbling" of the chromophore about its tethering bond. This motion is characterized by the quantity D_w. The relationship between D_w and D_{ROT} can be estimated by the approximation that the experimental $\tau \sim \tau_{OR} \sim \tau_{HR}$,

$$\tau \approx \tau_{OR} \approx \tau_{HR} = \frac{1}{6D_{ROT}} = \frac{7\theta_0^2}{24D_W}$$
$$D_{ROT} = \left(\frac{4}{7\theta_0^2}\right) D_W \qquad \text{4-7}$$

The rotational diffusion constants were determined to be D_{ROT} = 49.0 ± 3.1 MHz and D_{ROT} = 41.8 ± 2.1 MHz for the BLPA-5 and BLPA-10 films, respectively (eqn. 4-7). The slower time constant in BLPA-10 is consistent with aggregation of the chromophores.

As can be seen in eqn. 4-7, the relationship between D_{ROT} and D_w depends on the angle of the confining cone (Fig. 4-9, A.). For θ_0 = 0, the relationship is undefined, and this situation corresponds physically to the probe being immobile and unable to exhibit diffusional motion. For physically realistic angles, between *ca.* 30° and 90°, the coefficient ($4/7\theta_0^2$) varies between 2.08

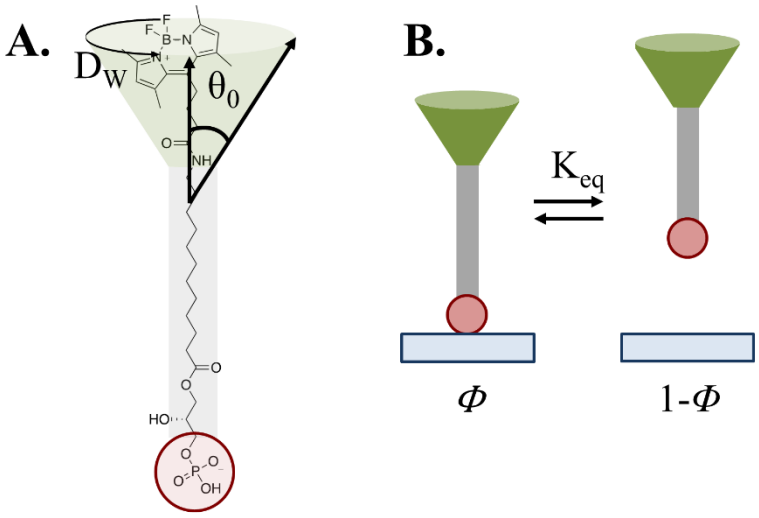

Figure 4-9: Schematic of equilibrium system under consideration.

and 0.23, for θ_0 = 54.7°, the magic angle, 0.63, and for θ_0 = 43.4°, $D_{ROT} = D_w$. Owing to the heterogeneity in both the BLPA-5 and BLPA-10 films, the BLPA probe population is likely characterized by a random orientational distribution. For such a distribution the confining cone semi-angle distribution averages to 54.7°,[37-38] yielding a value of $D_{ROT} = 0.63D_w$ = 30.9 ± 2.0 MHz for BLPA-5, and 26.5 ± 1.3 MHz for BLPA-10.

Implications of the Ba-ODPA/BLPA system thermodynamics on the diffusional dynamics. Comparing rotational diffusion and translational diffusion data on the same system can provide substantial insight into the properties of the system, with the detailed information content depending on the system. As noted above, chromophore motion is described in the context of the hindered rotor model,[37-38] and it is the relationship of the wobbling diffusion constant, D_w, for chromophore motion about its tethering bond that we must relate to the rotational diffusion constant, D_{ROT}. Longer range, translational diffusion of the same chromophore within the LB film will be mediated by interactions between the amphiphile phosphonate headgroups and the support surface, and both of these issues have to be taken into account in extracting information from these data.

The relationship between rotational diffusion and translational diffusion is understood for a spherical particle is a uniform medium, where the rotational diffusion constant is given by the Debye-Stokes-Einstein equation (eqn. 4-8) and the translational diffusion constant is given by the Stokes-Einstein-Sutherland equation (eqn. 4-9).

$$D_{ROT} = \frac{k_B T}{8\pi\eta r^3} \qquad 4\text{-}8$$

$$D_{ROT} = \frac{k_B T}{6\pi\eta r} \qquad 4\text{-}9$$

where η is the viscosity of the medium, r is the radius of the diffusing particle and k_BT is the thermal energy term. There are well-established correction factors for eqn. 4-8 to account for the boundary condition between the particle and the medium in which it is immersed, as well as for the non-spherical shape of the particle, but those correction factors yield only small changes from eqn. 4-8 for the systems of interest, and their inclusion does not bear on the fundamental relationship between D_{ROT} and D_T (eqn. 4-10).

$$D_T = \left(\frac{4r^2}{3} \right) D_{ROT} \qquad 4\text{-}10$$

Eqn. 4-10 is frequently not obtained experimentally because of the specific physical and chemical conditions of the system under investigation.

For the LB films reported here the amphiphile constituents interact with the solid support and it is possible to estimate the energy of that interaction. Experimentally, the value of D_T recovered, D_T^{eff}, is less than that expected if the adlayer were not interacting with the support (eqn. 4-9). There are a variety of ways to interpret a value of D_T^{eff} less than that predicted by eqn. 4-9. While heterogeneities in the films certainly exist, including pinholes, regions of disproportionate ODPA:BLPA concentrations due to aggregation, or the potential formation of multilayer islands, the D_T and D_{ROT} values are acquired as average values over tens of microns of film surface. For a heterogeneous system such anomalous diffusion is considered to result from frustrated chromophore motion.[49-51] The film under consideration here contains only one amphiphile in addition to the chromophore, therefore the notion of anomalous diffusion does not apply. For a system where there is an equilibrium between the free and surface-bound amphiphile, the value of D_T^{eff} reflects the fraction of time the chromophores are free to diffuse, i.e. not bound to the support. In this treatment we focus on the dynamic rather than the steady state (mobile fraction) contribution to the FRAP data. The steady state contributions to these data appear to be the same for the two

chromophore concentrations to within the experimental uncertainty (Table 4-1), and the normalization of the experimental FRAP data can, in principle, influence the recovered value for the mobile fraction, where time-domain data are not affected by normalization.

We model this equilibrium according to eqn. 4-11, with the diffusion constant of the bound species being zero.

$$\begin{aligned} D_T^{eff} &= A_{free} D_T + A_{bound} D_T^{bound} = A_{free} D_T \\ A_{free} + A_{bound} &= 1 \\ D_T^{bound} &= 0 \end{aligned} \qquad 4\text{-}11$$

The free fraction, A_{free}, is related to the equilibrium constant for this system (Fig. 4-9, B.). If the bound amphiphiles have a surface coverage ϕ, then the free sites are given by 1-ϕ, which is equal to A_{free}, and the equilibrium constant for this system is

$$K_{eq} = \frac{k_{free}}{k_{bound}} = \frac{(1-\phi)^2}{\phi} \qquad 4\text{-}12$$

The fraction of free sites, A_{free}, is related to K_{eq} by

$$A_{free} = 1 - \left(\frac{(2 + K_{eq}) - \sqrt{K_{eq}^2 + 4K_{eq}}}{2} \right) \qquad 4\text{-}13$$

Thus determination of A_{free} from the experimentally-derived quantities D_w, θ_0 and D_T^{eff} provides K_{eq}.

We calculate the hydrodynamic volume of BLPA to be 602 Å^3, corresponding to r = 5.2 Å for a spherical diffusing species. Using eqn. 4-10 we calculate D_T = 11.1 ± 0.7 μm^2/s for BLPA-5 and D_T = 9.6 ± 0.5 μm^2/s for BLPA-10 using D_{ROT} values derived from the experimental FADI data.

The experimental values of D_T^{eff} for BLPA, determined by FRAP, are 0.26 ± 0.09 $\mu m^2/s$ for BLPA-5 and 0.09 ± 0.02 $\mu m^2/s$ for BLPA-10. Using eqn. 4-11 we determine A_{free} = 0.022 ± 0.009 for BLPA-5 and 0.009 ± 0.002 for BLPA-10. From A_{free} = 1-ϕ, we determine K_{eq} = 5.0 (+4.9,-3.2) $x10^{-4}$ for BLPA-5 and 8.2 (+4,-3.3) $x10^{-5}$ for BLPA-10. As the equilibrium constant for this system is cast as a dissociation constant, we can calculate the free energy of dissociation for the film constituents (Table 4-3).

Table 4-3: Calculated Diffusion constant (D_T), Unbound free fraction (A_{free}), Dissociation equilibrium constant (K_{eq}), and Free energy for dissociation (ΔG_{dis}) for the BLPA in a Ba-ODPA LB film.

Mole% BLPA	D_T^0 ($\mu m^2/s$)	Unbound fraction (A_{free})	K_{eq} ($x10^{-4}$)	ΔG_{dis} (kJ/mol)
5%	11.1 ± 0.7	0.023 ± 0.009	5.0 (+4.9,-3.2)	18.5 (+2.6,-1.7)
10%	9.6 ± 0.5	0.009 ± 0.002	0.8 (+0.4,-0.3)	22.9 (+1.3, -0.9)

$$\Delta G_{dis} = -RT \ln K_{eq} \qquad 4\text{-}14$$

For BLPA-5 we find ΔG_{dis} = 18.5 (+2.6,-1.7) kJ/mol and for BLPA-10, ΔG_{dis} = 22.9 (+1.3, -0.9) kJ/mol. There are several important pieces of information contained in these data. The first important point to note is that (dipolar) aggregation is more prominent for BLPA-10 than for BLPA-5, and the effective change in the net driving force for adlayer formation due to an unknown amount of aggregation is energetically favorable by *ca*. 4 kJ/mol. The second is that the strength of interaction between the phosphate amphiphile and the Ba/SiO_x surface is very similar to that of the hydrogen bond enthalpies of water (*ca.* 23 kJ/mol),[52] and consistent with previous results,[53] but somewhat larger than that reported for water in proximity of nonpolar species.[54] We attribute much of the observed interactions to be due to intermolecular hydrogen bonding between ODPA molecules or ODPA and the hydroxylated silica surface. The metal ions that were carried from the LB trough subphase may be facilitating interactions between the amphiphile and the support but these interactions cannot be considered complexation in any sense.[55-57] In fact, it is not likely

that much interaction occurs between the Ba^{2+} and ODPA due to the sub-optimal pH during transfer to the support, a condition that reduces transfer of the metal ion to the support.[23]

4.5 Conclusions

We have investigated the dynamics of a tethered BODIPY chromophore contained in a LB film. Our goal in this work was to quantitate the fluidity and adhesion of the adlayer to the interface. By examining the diffusional behavior of this tethered chromophore over length scales ranging from molecular through macroscopic, we have demonstrated a direct and novel means for the evaluation of adlayer binding strength on a support surface. This is the first report that we are aware of that utilizes complementary molecular diffusion measurements for this purpose. Simultaneously, we are able to ascertain the motional freedom that is characteristic of this chromophore and the effect of chromophore aggregation on molecular motion. These data provide insight into the binding strength of a barium phosphonate species to a silica surface and, by extension, provide an estimate of the binding strength for related interfaces. The value obtained for ΔG_{dis}, *ca*. 20 kJ/mol, is entirely consistent with interactions dominated by H-bonding[58] and there is also a chromophore concentration dependence that suggests some information on the interaction energy of aggregated chromophores.

We note that the strength of interaction for our monolayer with a silica support is very similar to the binding interactions responsible for the formation of alkanethiol monolayers on gold and mercury.[12-13, 59] This is an important comparison to make because the spectroscopic evaluation of chromophore dynamics in an alkanethiol/gold SAM is limited by chromophore quenching,[60] and these data offer a way to at least estimate the expected dynamics for this family of systems.

The next step in this work is to evaluate the role of chemical modification of the support as a means of controlling binding strength.

REFERENCES

REFERENCES

1. Ratner, M., A brief history of molecular electronics. *Nature Nanotech.* **2013,** *8*, 378-381.

2. Bain, C. D.; Troughton, E. B.; Tao, Y. T.; Evall, J.; Whitesides, G. M.; Nuzzo, R. G., Formation of Monolayer Films By the Spontaneous Assembly of Organic Thiols From Solution Onto Gold. *J. Am. Chem. Soc.* **1989,** *111* (1), 321-335.

3. Camillone, N.; Chidsey, C. E. D.; Eisenberger, P.; Fenter, P.; Li, J.; Liang, K. S.; Liu, G. Y.; Scoles, G., Structural Defects in Self-Assembled Organic Monolayers Via Combined Atomic-Beam and X-Ray-Diffraction. *J. Chem. Phys.* **1993,** *99* (1), 744-747.

4. Camillone, N.; Chidsey, C. E. D.; Liu, G. Y.; Putvinski, T. M.; Scoles, G., Surface-Structure and Thermal Motion of Normal-Alkane Thiols Self-Assembled On Au(111) Studied By Low-Energy Helium Diffraction. *J. Chem. Phys.* **1991,** *94* (12), 8493-8502.

5. Camillone, N.; Chidsey, C. E. D.; Liu, G. Y.; Scoles, G., Superlattice Structure At the Surface of a Monolayer of Octadecanethiol Self-Assembled On Au(111). *J. Chem. Phys.* **1993,** *98* (4), 3503-3511.

6. Chidsey, C. E. D.; Liu, G. Y.; Rowntree, P.; Scoles, G., Molecular Order At the Surface of an Organic Monolayer Studied By Low-Energy Helium Diffraction. *J. Chem. Phys.* **1989,** *91* (7), 4421-4423.

7. Chidsey, C. E. D.; Liu, G. Y.; Scoles, G.; Wang, J., Helium Diffraction From Overlayers Physisorbed On a Self- Assembled Organic Monolayer. *Langmuir* **1990,** *6* (12), 1804-1806.

8. Chidsey, C. E. D.; Porter, M. D.; Allara, D. L., Electrochemical Characterization of N-Alkyl Thiol, Sulfide, and Disulfide Monolayers On Gold. *J. Electrochem. Soc.* **1986,** *133* (3), C130-C130.

9. Dubois, L. H.; Zegarski, B. R.; Nuzzo, R. G., The Chemisorption of Organosulfur Compounds On Gold Surfaces - Construction of Well-Defined Organic-Solids. *J. Vac. Sci. Technol. A-Vac. Surf. Films* **1987,** *5* (4), 634-635.

10. Dubois, L. H.; Zegarski, B. R.; Nuzzo, R. G., Molecular Ordering of Organosulfur Compounds On Au(111) and Au(100) - Adsorption From Solution and in Ultrahigh-Vacuum. *J. Chem. Phys.* **1993,** *98* (1), 678-688.

11. Ulman, A., Formation and structure of self-assembled monolayers. *Chem. Rev.* **1996,** *96* (4), 1533-1554.

12. Karpovich, D. S.; Blanchard, G. J., Direct Measurement of the Adsorption Kinetics of Alkanethiolate Self-Assembled Monolayers on a Microcrystalline Gold Surface. *Langmuir* **1994,** *10* (9), 3315-22.

13. Schessler, H. M.; Karpovich, D. S.; Blanchard, G. J., Quantitating the Balance between Enthalpic and Entropic Forces in Alkanethiol/Gold Monolayer Self Assembly. *J. Am. Chem. Soc.* **1996,** *118* (40), 9645-9651.

14. Ryan, D.; Parviz, B. A.; Linder, V.; Semetey, V.; Sia, S. K.; Su, J.; Mrksich, M.; Whitesides, G. M., Patterning multiple aligned seld-assembled monolayers using light. *Langmuir* **2004,** *20* (21), 9080-9088.

15. Rampi, M. A.; Schueller, O. J. A.; Whitesides, G. M., Alkanethiol self-assembled monolayers as the dielectric of capacitors with nanoscale thickness. *Appl. Phys. Lett.* **1998,** *72*, 1781-1783.

16. Zhang, H.; Chung, S.-W.; Mirkin, C. A., Fabrication of sub-50-nm solid-state nanostructures on the basis of dip-pen nanolithography. *Nano Lett.* **2003,** *3* (1), 43-45.

17. Lee, K.-B.; Kim, E.-Y.; Mirkin, C. A.; Wolinsky, S. M., The use of nanoarrays for highly sensitive and selective detection of human immunodeficiency virus type 1 in plasma. *Nano Lett.* **2004,** *4* (10), 1869-1872.

18. Langmuir, I., The constitution and fundamental properties of solids and liquids. II. Liquids. *J. Am. Chem. Soc.* **1917,** *39* (9), 1848-1906.

19. Blodgett, K. B.; Langmuir, I., Built-up films of barium stearate and their optical properties. *Phys. Rev.* **1937,** *51*, 964-982.

20. Blodgett, K. B., Films built by depositing successive monomolecular layers on a solid surface. *J. Am. Chem. Soc.* **1935,** *57*, 1007-1022.

21. Ariga, K.; Yamauchi, Y.; Mori, T.; Hill, J. P., What can be done with the Langmuir-Blodgett method? Recent developments and its critical role in materials science. *Adv. Mat.* **2013,** *25*, 6477-6512.

22. Shimomura, M.; Song, K.; Rabolt, J. F., Spectroscopic determination of diffusion in Langmuir-Blodgett films. 1. Interlayer diffusion of cadmium arachidate and its deuterated analogue through a polymer interface. *Langmuir* **1992,** *8*, 887-893.

23. Fanucci, G. E.; Seip, C. T.; Petruska, M. A.; Nixon, C. M.; Ravaine, S.; Talham, D. R., Organic/inorganic Langmuir-Blodgett films based on known layered solids: Divalent and trivalent metal phosphonates. *Thin Solid Films* **1998,** *327-329*, 331-335.

24. Fanucci, G. E.; Talham, D. R., Langmuir-Blodgett films based on known layered solids: Lanthanide(III) octadecylphosphonate LB films. *Langmuir* **1999,** *15*, 3289-3295.

25. Talham, D. R., Conducting and magnetic Langmuir-Blodgett films. *Chem. Rev.* **2004,** *104*, 5479-5501.

26. Byrd, H.; Pike, J. K.; Talham, D. R., Inorganic monolayers formed at an organic template: A Langmuir-Blodgett route to monolayer and multilayer films of zirconium octadecylphosphonate. *Chem. Mater.* **1993,** *5*, 709-715.

27. Petruska, M. A.; Talham, D. R., Organic/inorganic Langmuir-Blodgett films based on metal phosphonates. 3. An azobenzene-derivatized phosphonic acid forms continuous lattice layers with divalent, trivalent, and tetravalent metal ions. *Chem. Mater.* **1998,** *10* (11), 3672-3682.

28. Trabelsi, S.; Zhang, S.; Zhang, Z.; Lee, T. R.; Schwartz, D. K., Semi-fluorinated phosphonic acids form stable nanoscale clusters in Langmuir-Blodgett and self-assembled monolayers. *Soft Matter* **2009,** *5*, 750-758.

29. Seip, C. T.; Granroth, G. E.; Meisel, M. W.; Talham, D. R., Langmuir-Blodgett films of known layered solids: Preparation and structural properties of octadecylphosphonate bilayers with divalent metals and characterization of a magnetic Langmuir-Blodgett film. *J. Am. Chem. Soc.* **1997,** *119*, 7084-7094.

30. Forstner, M. B.; Kas, J.; Martin, D., Single lipid diffusion in Langmuir Monolayers. *Langmuir* **2001,** *17* (3), 567-570.

31. Bertoncello, P.; Ciani, I.; Li, F.; Unwin, P. R., Measurement of apparent diffusion coefficients within ultrathin Nafion Langmuir-Schaefer films: Comparison of a novel scanning electrochemical microscopy approach with cyclic voltammetry. *Langmuir* **2006,** *22* (25), 10380-10388.

32. Wright, L. L.; Palmer, A. G. I.; Thompson, N. L., Inhomogeneous translational diffusion of monoclonal antibodies on phospholipid Langmuir-Blodgett films. *Biophys. J.* **1988,** *54* (3), 463-470.

33. Selle, C.; Ruckerl, F.; Martin, D. S.; Forstner, M. B.; Kas, J., Measurement of diffusion in Langmuir monolayers by single particle tracking. *Phys. Chem. Chem. Phys.* **2004,** *6*, 5535-5542.

34. Sickert, M.; Rondolez, F., Shear viscosity of Langmuir monolayers in the low-density limit. *Phys. Rev. Letters* **2003,** *90* (12), 126104-1-4.

35. Ellenberg, J.; Siggia, E. D.; Moriera, J. E.; Smith, C. L. P., J. F.; Worman, H. J.; Lippincott-Schwartz, J., Nuclear membrane dynamics and reassembly in living cells: Targeting of an inner nuclear membrane protein in interphase and mitosis. *J. Cell Biol.* **1997,** *138* (6), 1193-1206.

36. Setiawan, I.; Blanchard, G. J., Ethanol induced perturbations to planar lipid bilayer structures. *J. Phys. Chem. B* **2014,** *118*, 537-546.

37. Lipari, G.; Szabo, A., Effect of Librational Motion on Fluorescence Depolarization and Nuclear Magnetic Resonance Relaxation in Macromolecules and Membranes. *Biophys. J.* **1980,** *30*, 489-506.

38. Szabo, A., Theory of fluorescence depolarization in macromolecules and membranes. *J. Chem. Phys.* **1984,** *81* (1), 150-167.

39. *Langmuir-Blodgett Films*. Springer Science: New York, 1990.

40. Rabolt, J. F.; Burns, C. F.; Schlotter, N. E.; Swalen, J. D., Anisotropic orientation in molecular monolayers by infrared spectroscopy. *J. Chem. Phys.* **1983,** *78*, 946-952.

41. Sherstneva, T. A.; Birin, K. P.; Arslanov, V. V., The aggregation behavior of amphiphilic pyrene chromophore in solutions and langmuir monolayers. *Fizikokhimiya Poverkhnosti i Zashchita Materialov* **2013,** *49* (1), 72-87.

42. Varughese, S., Non-covalent routes to tune the optical properties of molecular materials. *J. Mater. Chem. C* **2014,** *2*, 3499-3516.

43. Pescitelli, G.; DiBari, L.; Berova, N., Application of electronic circular dichroism in the study of supramolecular systems. *Chem. Soc. Rev.* **2014,** *43* (5211-5233).

44. Spano, F. C.; Silva, C., H- and J-Aggregate behavior in polymeric semiconductors. *Annu. Rev. Phys. Chem.* **2014,** *65*, 477-500.

45. Lu, H.; Xue, Z.; Mack, J.; Shen, Z.; You, X.; Kobayashi, N., Specific Cu^{2+}-induced J-aggregation and Hg^{2+}-induced fluorescence enhancement based on BODIPY. *Chem. Commun.* **2010,** *46*, 3565-3567.

46. Choi, S.; Bouffard, J.; Kim, Y., Aggregation-induced emission enhancement of a meso-trifluoromethyl BODIPY via J-aggregation. *Chem. Sci.* **2014,** *5*, 751-755.

47. Tokoro, Y.; Nagai, A.; Chujo, Y., Nanoparticles via H-aggregation of amphiphilic BODIPY dyes. *Tet. Letters* **2010,** *51* (26), 3451-3454.

48. Olivier, J.-H.; Widmaier, J.; Ziessel, R., Near-infrared fluorescent nanoparticles formed by self-assembly of lipidic (Bodipy) dyes. *Chem. Eur. J.* **2011,** *17*, 11709-11714.

49. Metzler, R.; Klafter, J., The random walk's guide to anomalous diffusion: A fractional dynamics approach. In *Physics Reports*, Elsevier: Amsterdam, 2000; Vol. 339, pp 1-77.

50. Palombo, M.; Gabrielli, A.; Servedio, V. D. P.; Ruocco, G.; Capuani, S., Structural disorder and anomalous diffusion in random packing of spheres. *Sci. Rep.* **2013,** *3* (2361), 1-7.

51. Novikov, D. S.; Fieremans, E.; Jensen, J. H.; Helpern, J. A., Random walks with barriers. *Nature Phys.* **2011,** *7*, 508-514.

52. Suresh, S. J.; Naik, V. M., Hydrogen bond thermodynamic properties of water from dielectric constant data. *J. Chem. Phys.* **2000,** *113* (21), 9727-9732.

53. Nie, H. Y., Revealing different bonding modes of self-assembled octadecylphosphonic acid monolayers on oxides by time-of-flight secondary ion mass spectrometry: Silicon vs Aluminum. *Anal. Chem.* **2010,** *82*, 3371-3376.

54. Silverstein, K. A. T.; Haymet, A. D. J.; Dill, K. A., The strength of hydrogen bonds in liquid water and around nonpolar solutes. *J. Am. Chem. Soc.* **2000,** *122*, 8037-8041.

55. Rizkalla, E. N.; Zaki, M. T. M., Metal chelates of phosphonate-containing ligands 1. Stability of some N,N,N',N'-ethylenediaminetetra(methylenephosphonic) acid metal chelates. *Talanta* **1979,** *26*, 507-510.

56. Rizkalla, E. N.; Zaki, M. T. M., Metal chelates of phosphonate-containing ligands VI. Complexes of ethylenediaminetetra(methylenephosphonic) acid with Cd, Mg, Ca and Ba. *Talanta* **1980,** *27*, 769-770.

57. Barouda, E.; Demadis, K. D.; Freeman, S. R.; Jones, F.; Ogden, M. I., Barium sulface crystallization in the presence of variable chain length aminomethylenetetraphosphonates and cations (Na^+ or Zn^{2+}). *Crystal Growth Des.* **2007,** *7* (2), 321-327.

58. Blanchard, G. J., A study of the state-dependent reorientation dynamics of oxazine 725 in primary normal aliphatic alcohols. *Journal of Physical Chemistry* **1988,** *92* (22), 6303-6307.

59. Blomgren, E.; Bockris, J. O. M.; Jesch, C., The adsorption of butyl, phenyl and naphthyl compounds at the interface mercury-aqueous acid solution. *J. Phys. Chem.* **1961,** *65* (11), 2000-2010.

60. Karpovich, D. S.; Blanchard, G. J., Dynamics of a tethered chromophore imbedded in a self-assembled monolayer. *Langmuir* **1996,** *12* (23), 5522-5524.

CHAPTER 5: THE INFLUENCE OF METAL IONS ON THE DYNAMICS OF SUPPORTED PHOSPHOLIPID LANGMUIR FILMS

Adapted with permission from:

Stephen. M. Baumler, and Gary J. Blanchard; The Influence of Metal Ions on the Dynamics of Supported Phospholipid Langmuir Films. Langmuir (2017), 33, 2986–2992.

5.1 Abstract

The translational diffusion dynamics of the zwitterionic lipid, 1,2-dimyristoyl-*sn*-glycero-3-phosphocholine (DMPC) at a planar phosphorylated support surface containing metal ions (Mg^{2+}, Ca^{2+}, Ba^{2+}, Ni^{2+}, Zn^{2+}, Cd^{2+}, Zr^{4+}) was investigated using X-ray photoelectron spectroscopy (XPS) and fluorescence recovery after photobleaching (FRAP). Fluorescence recovery curves yielded diffusion constants on the order of 2-5 $\mu m^2/s$ for the chromophore-tagged 12:0 NBD-Lyso-PC. Ionic interactions between the zwitterionic head-group and metal ions were found to play a secondary role in mediating lipid fluidity. This work provides quantitative insight into the extent to which the fluidity of a supported lipid film is mediated by the ionic interactions between head-group and surface vs. that of the lipid-lipid tail-group interactions.

5.2 Introduction

Supported lipid monolayers are an important structural motif that can be used to understand the fundamental processes that account for the properties of certain biomimetic interfaces and plasma membrane structures. The monolayer structure provides a comparatively simple structural motif for the characterization of acyl chain interactions as well as interactions between the support and the lipid. The most common methods used to prepare supported lipid systems involve a Langmuir approach (Langmuir-Blodgett[1-2] or Langmuir-Schaeffer[3]) or by the rupture and spreading of small lipid vesicles (vesicle fusion).[4] Regardless of preparation technique, these systems yield a film that maintains the diffusional properties comparable to multi-bilayer systems and these properties are known to be dependent on the supporting surface.[5]

Recent studies have examined the extent to which the underlying support influences the formation and adhesion of supported lipid bilayers prepared by the fusion deposition of small

unilamellar vesicles (SUVs) to a variety of supporting materials such as silica, glass, mica, various metal oxides such as TiO_2 and $SrTiO_3$, and more recently inorganic nanoparticles.[6-10] In all studies, the underlying support was shown to have a marked effect on both the rupture and spreading processes of the SUVs.

Similarly, both pH and ionic strength have been shown to play important roles in the formation of supported lipid bilayers through the SUV approach.[11] Studies have recently examined the influence of metal ions such as Mg^{+2},[12] Ca^{2+}, [13-16] and Sr^{2+} [17-18] on the roles of adhesion and stability. In these studies, the metal ions were shown to provide added adhesion and stability through the screening of charges, modifying ionic interactions between lipids and support. In a similar fashion, pH has been shown to modulate the formation of different lipid structural motifs through charge mediation at the metal oxide interface.[19]

Utilizing the formation and adhesion of SUVs, we have shown previously that robust air-stable lipid layers can be formed through the aid of zirconium-phosphate (ZP) chemistry and is dependent upon the lipid head-group used in self-assembly process.[20] The DMPC lipid adlayers formed by this approach were found to be structurally complete and nominally homogeneous monolayers. Similar studies have examined the role to which different metal ions play in mediating lipid-surface interactions in the formation of the lipid-metal-phosphonate films.[21] The formation of structurally robust lipid films through this lipid-metal coordination process were found to rely upon the use of metal ions with high charge and small ionic radius. These films, compared to their ZP counterpart, were found to be spatially heterogeneous with only partial coverage.

While there have been many studies on the effect of metal cations, pH, ionic strength, and supporting metal oxide surface on the formation of supported lipid films, relatively little work has

been done examining how these films behave after formation. Pretreatment effects, namely changes in surface roughness, have been shown to change the diffusional properties of the supporting lipid layers.[22-23] The diffusional properties appear to be mediated, in part, by the presence of an ill-defined water underlayer (~20-40Å) between the lipid head-groups and support surface.[24-25] Recent work has suggested that electrostatically induced ordering of the water underlayer may alter diffusional properties of supported lipid layers due to a frictional component from "hydration forces" between the support surface and lipid head-groups.[26-27]

While the presence of divalent cations has been shown to affect both the formation and adhesion of SUVs to the surface, there are two issues that remain unresolved. The lipid interlayer interactions can serve to mask the interactions of primary concern here, namely the support-lipid interaction, and the presence and influence of metal ions in the water layer between the support and the lipid remains to be elucidated fully. In the present study we have examined the influence of not only the underlying surface, but also metal ions contained in the galley between the supporting surface and lipid head-groups on the diffusional properties of the supported lipid monolayer. We use the Langmuir-Blodgett method[1-2] to provide a controlled means of forming these films in the presence of the various metal ions. Diffusional measurements of chromophores in the supported film are an effective means of characterizing interactions between the lipid and the supporting surface as well as intermolecular interactions between the supported lipids.

5.3 Experimental

Materials. 1,2-dimyristoyl-*sn*-glycero-3-phosphocholine (DMPC) and 1-(12-[(7-nitro-2-1,3-benzoxadiazol-4-yl)amino]dodecanoyl)-2-hydroxy-*sn*-glycero-3-phosphocholine (NBD-LPC) were purchased from Avanti® Polar Lipids, Inc. (Fig. 5-1). Chloroform was purchased from

Macron Fine Chemicals and used as received. 2,4,6 Trimethyl pyridine (99%), acetonitrile (HPLC), barium chloride dihydrate (99.9%), cadmium chloride (99.9%), calcium chloride dihydrate (99%), magnesium chloride hexahydrate (98%), nickel chloride hexahydrate (reagent plus), phosphorus oxychloride (99%), Trizma® Hydrochloride (>99.0%), Trizma® base (>99.9%), zinc chloride (>98%), and zirconium oxychloride octahydrate (98%) were purchased from Sigma Aldrich and used as received. Water was obtained from a Milli-Q Plus water purification system and used for all experiments.

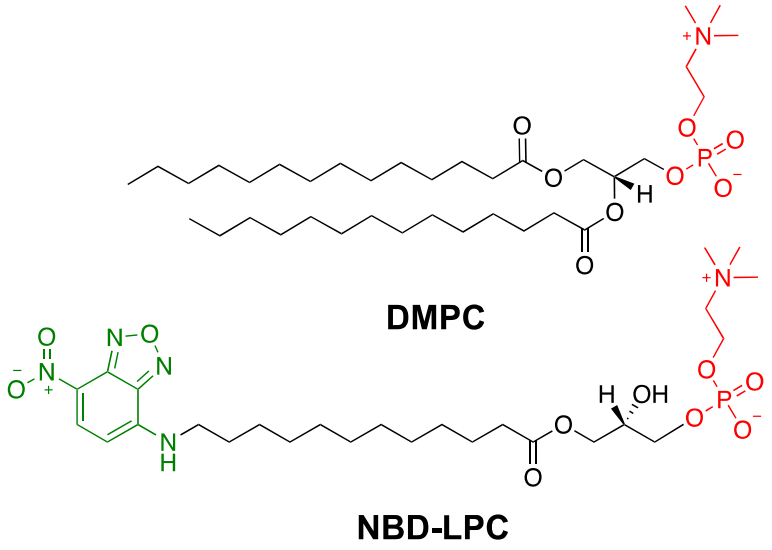

Figure 5-1: Chemical structures of 1,2-dimyristoyl-sn-glycero-3-phosphocholine (DMPC) and 1-(12-[(7-nitro-2-1,3-benzoxadiazol-4-yl)amino]dodecanoyl)-2-hydroxy-sn-glycero-3-phosphocholine (NBD-LPC).

Substrate Phosphorylation. The round coverglass substrates were composed of D263M borosilicate glass (#1.5 x 25 mm dia., Warner Instruments) and were placed in piranha solution ($1H_2O_2$:$3H_2SO_4$, *Caution! Strong oxidizer!*) for 30 min. After cleaning, the substrates were sonicated for 5 minutes with water and thoroughly rinsed with dry acetonitrile. The substrates were then exposed to phosphorus oxychloride (0.4 mL) and 2,4,6-trimethylpyridine (0.4 mL) in

10 mL dry acetonitrile for 3 hrs. The substrates were rinsed thoroughly with dry acetonitrile and kept covered in water until needed for deposition.

Formation of DMPC Monolayers. We use the term "DMPC monolayer" in reference to a monolayer at the air–water interface and "DMPC film" in reference to the monolayer transferred to the solid support. Phospholipid monolayers were prepared on a Langmuir trough (Nima) equipped with a paper Wilhelmy plate. The aqueous subphase was composed of 50 mM Tris buffer at pH 7.5 and 1mM of the chosen metal chloride. The temperature of the subphase was maintained at 20.0 ± 0.5 °C using a circulating water bath (Fisher) attached to the trough. A 30 μL aliquot of a 1 mg/mL DMPC/NBD-LPC (2 mol%) in chloroform solution was used for monolayer spreading. During spreading, care was taken to prevent the spreading needle from touching the surface as well as preventing the surface pressure from rising above 0.5 mN/m in order to ensure complete spreading. After spreading, the monolayer was allowed to equilibrate for 15 min. to ensure solvent evaporation and monolayer relaxation. The barriers were moved inward at a rate of 5 mm/min (<1 $Å^2$/molecule-min) until monolayer collapse. The isotherms were equally adjusted to account for solvent evaporation in the DMPC/NBD-LPC solution by 5 μL/hr.

Formation of Phospholipid Films. The phospholipid films were prepared by the Langmuir–Blodgett technique.[1-2] A large Teflon® Langmuir trough (KSV Nima) equipped with a dipping mechanism and a platinum Wilhelmy plate attached to a balance with an automated feedback system was used to maintain a constant surface pressure during film transfer. The temperature of the subphase was maintained at 20.0 ± 0.5 °C using a circulating water bath (Fisher) attached to the trough. The subphase and monolayer spreading solution were as described above.

The larger trough required 70 μL of a 1 mg/mL DMPC/NBD-LPC (2 mol%) solution. The barriers were moved inward at a rate of 5 mm/min (<1 $Å^2$/molecule-min) to compress the surface monolayer to 25 mN/m. The compressed monolayer was allowed to equilibrate for 15 min before it was transferred onto the glass support. The monolayer was transferred (upstroke) at a dipping speed of 5 mm/min while keeping the pressure constant. Transfer ratios for the films were measured to be 1.0 ± 0.1. The coated slides were placed in an Attofluor® cell chamber (Invitrogen) and gently covered with the subphase solution before FRAP measurements were made.

Fluorescence Recovery After Photobleaching (FRAP). FRAP measurements were conducted on a Nikon C2+ confocal laser scanning microscopy system consisting of a Nikon Eclipse Ti-E inverted microscope with a confocal scanning system (Nikon Ti-S-CON). The NBD-LPC was excited with the 488 nm line of a diode laser (Nikon Lu-N4), and emission was detected at 525 nm using a standard PMT detector (Nikon C2-DU3). A 20x objective lens was used for the films. Two independently prepared DMPC films were measured with a minimum of 10 measurements at random locations. Initial intensities (I_{pre}) were measured for 10 s. The bleaching time was set to 2 s at 100% laser power, and the recovery signal $I_{frap}(t)$ after photobleaching was collected over 2 min.

To account for acquisition bleaching, the recovery signals, $I_{frap}(t)$, were normalized using double normalization described by Phair *et al.* (eqn. 5-1).[28] $I_{frap\text{-}pre}$ is the average stimulation region intensity prior to photobleaching, $I_{ref\text{-}pre}$ is the average reference intensity prior to photobleaching, $I_{ref}(t)$ is reference intensity after photobleaching, and $frap(t)$ is the calculated normalized intensity.

$$frap(t) = \frac{I_{ref-pre}}{I_{ref}(t)} \cdot \frac{I_{frap}(t)}{I_{frap-pre}} \qquad 5\text{-}1$$

XPS Measurements. XPS measurements were performed on a Perkin-Elmer Phi 5600 ESCA instrument equipped with an Al Kα X-ray source to illuminate the sample at a take-off angle of 45°. Samples were analyzed at pressures between 10^{-9} and 10^{-8} Torr with a spot size is ca. 250 mm^2 and a pass energy of 187.9 eV and 29.4 eV for the survey and detailed scans, respectively. Survey scans of 0–1100 eV binding energy and detailed scans for the metal ion of interest as well as C1s, O1s, P2p, and Sn $3d_{5/2}$ or Si2p were measured for all samples. All peaks were corrected in reference to the C1s peak associated with adventitious C at 284.8 eV. Peak areas were determined by Shirley background subtraction and an area correction using calibrated sensitivity factors.

5.4 Results and Discussion

Langmuir monolayer organization mediation by metal ion identity. To better understand the influence of metal ion identity on the dynamics and physical characteristics of a supported zwitterionic phospholipid monolayer, surface pressure *vs.* mean molecular area isotherms were performed (Figs. 5-2 and 5-3). Changes in the isotherm were examined *vs.* changes in the metal ion identity.

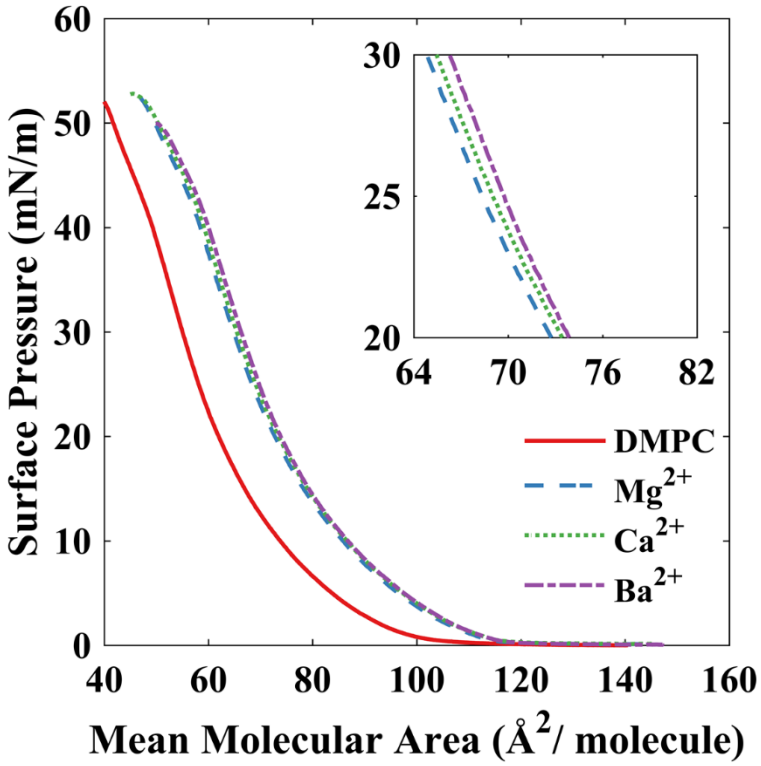

Figure 5-2: Surface pressure / mean molecular area-isotherm of the DMPC/NBD-LPC monolayers formed on subphases containing buffer (red solid), and 1 mM $MgCl_2$ (blue dash), $CaCl_2$ (green dot), or $BaCl_2$ (purple dash-dot). Inset: Expanded region showing mean molecular area at dipping pressure.

We first examined the effect of the alkaline earth metals (Mg^{2+}, Ca^{2+}, Ba^{2+}) on the isotherms. The alkaline metals showed an increase in mean molecular area vs. DMPC on the buffer phase containing no metal ions (we discuss the implications for this increase below). However, there was only a slight discernable difference between the alkaline earth metal identity and the mean molecular area of the DMPC monolayer. Next we examined the effect of a series of transition metals (Ni^{2+}, Zn^{2+}, Cd^{2+}, Zr^{4+}) on the isotherms. The transition metal ions also showed an increase in mean molecular area *vs.* DMPC on a buffered subphase without metal ions added. In contrast to the alkaline earth metals, the transition metals show a clear difference between the metal ion identity and the mean molecular area per DMPC monolayer. A noticeable trend in mean

molecular area, similar to that seen for a fatty acid monolayer, is observed: Buffer < Ni^{2+} ≤ Zn^{2+} < Cd^{2+} < Zr^{4+}.[29]

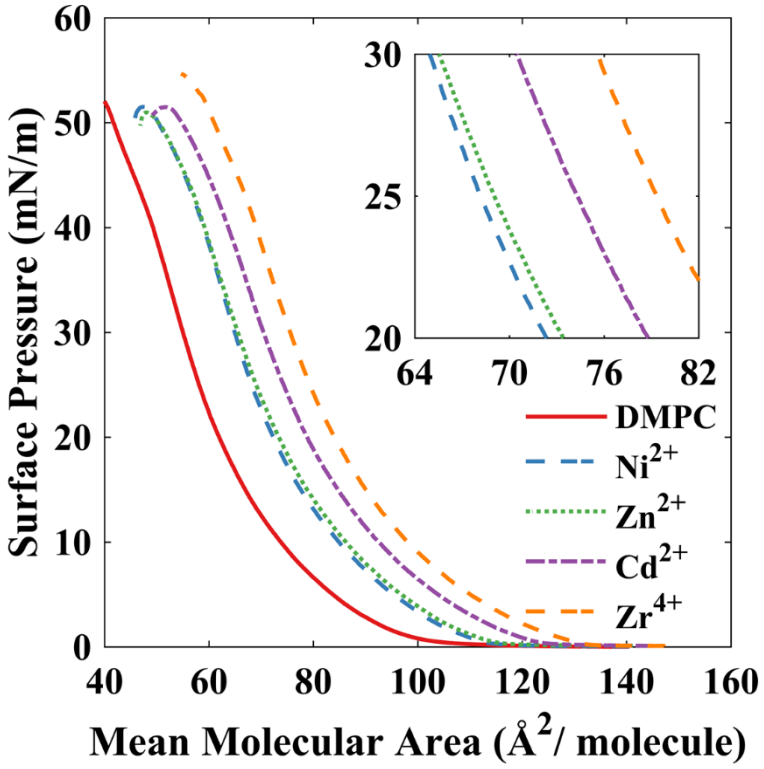

Figure 5-3: Surface pressure / mean molecular area-isotherm of the DMPC/NBD-LPC monolayers formed on subphases containing buffer (red solid), and 1 mM $NiCl_2$ (blue dash), $ZnCl_2$ (green dot), $CdCl_2$ (purple dash-dot), or $ZrOCl_2$ (orange dash). Inset: Expanded region showing mean molecular area at dipping pressure.

We correlate the increase in mean molecular area with increased competition for the anionic lipid phosphate moieties at the interface between the cationic metal ions in the subphase and the pendent (cationic) choline groups. At pH = 7.5, the phosphocholine head-group will be deprotonated leading to a net neutral[30] or, as suggested by recent molecular dynamics simulations, a slightly negative (-0.53*e*) charge.[31-32] Regardless of the overall charge of the monolayer without metal ions, the introduction of the positively charged metal cations (+2*e*) into the subphase disrupts any preexisting electrostatically induced local organization between the pendent lipid choline

(+0.75*e*) and phosphate moieties (-1.28*e*). The magnitude of disruption is likely dependent upon the strength of interaction between the metal ion and phosphonate group.[33-35]

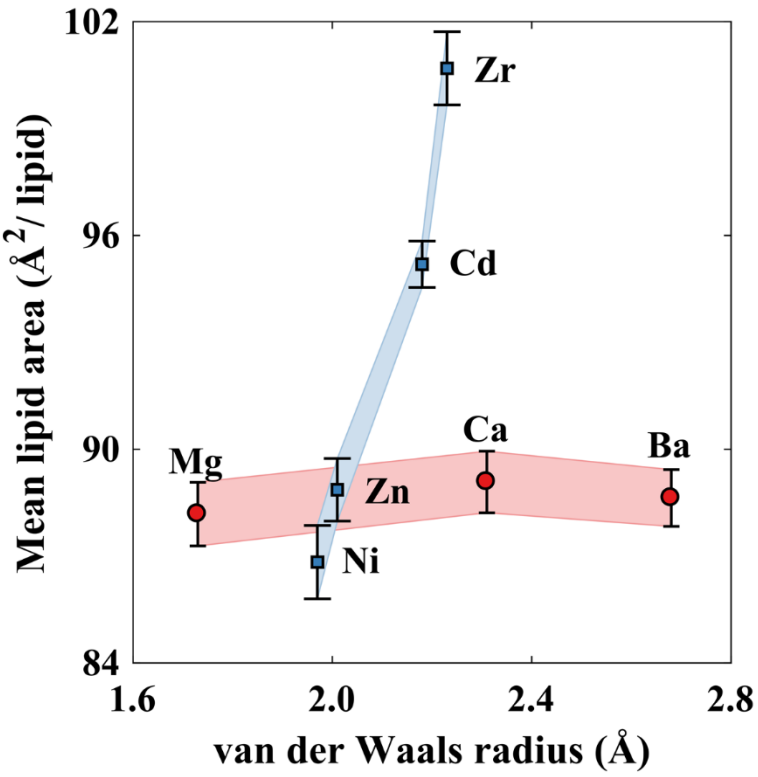

Figure 5-4: Interactions between the metal ions and lipid monolayer are shown as the mean lipid area vs. Metal ion van der Waal radius. Error bars are calculated by extrapolation of a line tangent to the isotherm between 20-30 mN/m down to 0 mN/m.

The electrostatic competition between metal ions, anionic phosphonate, and cationic choline are correlated as a change in the mean molecular area of the lipid monolayer for a given metal ion's van der Waal radius (Fig. 5-4).[36] We assert that as the attractive interaction between (cationic) metal ion and (anionic) phosphonate group increases, a concurrent increase in repulsive interactions between either individual metal ions at the interface or metal ions and the pendant phosphocholine should occur (dependent upon metal ion-lipid stoichiometry) resulting in the observed expansion of the isotherms. In both instances, the induced disruption of mean molecular area is greater for the transition metals than for the alkaline earth metals. The increased disruption

from the transition metal ions is likely due to the increased thermodynamic stability for the metal-phosphonate transition metal complexes over their alkaline earth metal counterparts.

Electrostatic interactions mediate transfer of metal ions from subphase to support surface. XPS was utilized to better understand the interactions mediating transfer of the metal ions to the support surface. An idealized diagram of the supported film surface is shown in Fig. 5-5. The values listed in Table 5-1 are relative intensities (corrected by the appropriate sensitivity factor) for the alkaline earth and transition metals transferred to either a phosphorylated fluorine-doped tin oxide (FTO) or phosphorylated silica surface versus phosphorus (P2p), tin ($Sn3d_{5/2}$), and silicon (Si2p) peaks.

Table 5-1: Relative metal ion surface coverage for the phosphorylated FTO and glass surfaces are reported versus phosphorus (P2p), tin (Sn3d5/2), and silica (Si2p) peak areas.

	FTO		Glass[a]
Metal ion	**M^{x+}:Sn 3d5/2**	**M^{x+}:P 2p**	**M^{x+}:Si 2p**
Mg^{2+} (2s)[c]	-	-	-
Ca^{2+} (2p)	0.03	0.22	0.03
Ba^{2+} (3d5/2)	0.06	1.18	0.04
Ni^{2+} (2p3/2)	0.06	0.40	0.03
Zn^{2+} (2p3/2)	0.22	1.59	0.22
Cd^{2+} (3d5/2)	0.04	0.61	0.07
Zr^{4+} (3d)[b]	0.80	-	1.07

[a,b] P2p peaks were unresolved

[c] Mg2s peak was unresolved. The Mg KLL auger peak (305.5 eV) is present in the Mg survey scan, indicating transfer (Fig. A5-1)

XPS provides a semi-quantitative assessment of the presence of metal ions on the surface after transfer from the LB-trough. For all metal ions, except magnesium, signal intensities were present above baseline indicating that metal ions are transferred from the LB-trough to the supporting surface (example survey scans and detailed scans are shown in Figs. A5-1, A5-2, A5-3). For a process where the metal ion transfer to supporting surface is mediated by lipid-phosphonate

interactions (1:1 M^{x+}:DMPC) an expected ratio of M^{x+}:P is *ca.* 0.18 ± 0.04, whereas metal ion transfer mediated by surface phosphates (1:1 M^{x+}:surface phosphate) an expected ratio of M^{x+}:P is *ca.* 0.82 ± 0.04 (calculations can be found in appendix A5.1). The observed ratios between the metal ion and phosphorus peaks suggests that the surface phosphates, not lipids, are primarily mediating metal ion transfer.

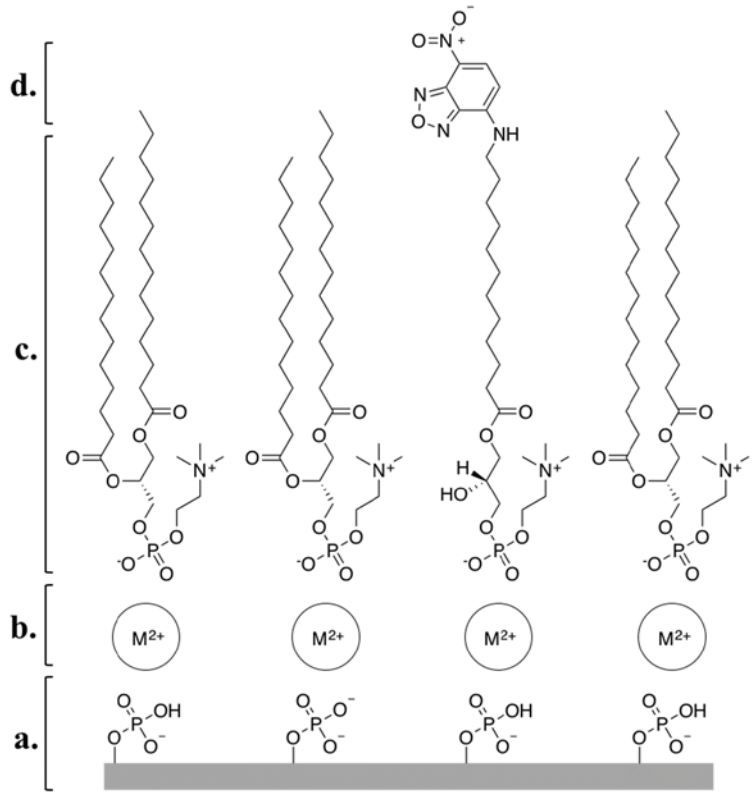

Figure 5-5: Idealized diagram of the prepared supported lipid layer. The films are comprised of the phosphorylated glass support (a.), metal ion and aqueous under-layer (b.), and DMPC/NBD-LPC film (c.) with buffer adlayer (d.).

We note that both Zn^{2+} and Zr^{4+} have much higher ratios relative to the other metal ions. Given the buffered pH of 7.5 and relatively low hydroxide K_{sp} of zinc, the increased Zn^{2+} ratio is attributed to the transfer of neutral $Zn(OH)_2$ species into the adventitious water layer described earlier. The higher Zr^{4+} ratio is attributed to both complete surface phosphate coverage and also

due to the transfer of other soluble species such as $ZrO(OH)_y^{2-y}$ (including nonstoichiometric water) or hydrous oxide polymers from the trough to surface.[37-38]

Phospholipid Langmuir film dynamics minimally affected by metal ion identity. Fluorescence recovery after photobleaching (FRAP) experiments were performed on the film surfaces to better understand the influence of the metal ion identity in the under-layer on the dynamics of the supported DMPC film. The translational diffusion of the fluorescent probe NBD-LPC in the DMPC film was measured to evaluate this relationship.

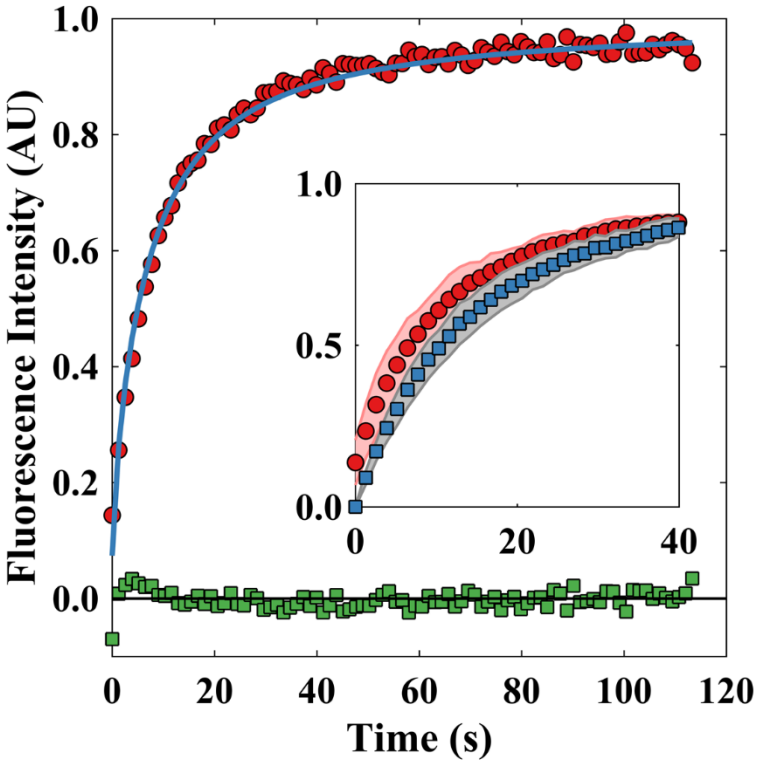

Figure 5-6: Normalized FRAP recovery curve from one SiO_x surface fitted to the full reaction-diffusion model. Residuals are plotted below. Inset: Average of all trials on the SiO_x (red circles) and phosphorylated surface (blue squares) are plotted with error (standard deviation) represented as shading.

Typical normalized recovery curves and fits for the DMPC films supported on a glass surface are shown in Fig. 5-6. The fluorescence recovery curves were fitted to a single binding-site model described by eqn. 5-2 where *f* represents the free, unbound fluorescent probe, *m*

represents a binding site, and *b* represents a bound complex of fluorescent probe and binding site. The rate constants for this reaction are described as k_{on} and k_{off} for association and dissociation, respectively.

$$f + m \underset{k_{off}}{\overset{k_{on}}{\rightleftarrows}} b \qquad \text{5-2}$$

There are many different models used for the fitting of FRAP data and we assert that the full reaction-diffusion model is best suited under the experimental conditions relevant to this work. The use of a pure diffusion model that does not account for interactions between the support and the monolayer when binding is present, such as the Soumpasis model, is inappropriate.[39] Similarly, caution is also warranted in using models that have no analytical dependence on the bleaching spot size, such as the off-rate dependent recovery described by Bulinski.[40] Bulinski *et al*. showed that for cases when diffusion is much faster than the binding rate constant and timescale of the measurement, the fluorescence recovery is determined by the dissociation rate constant, k_{off} (eqn. 5-3).[40]

$$frap(t) = 1 - e^{-k_{off} t} \qquad \text{5-3}$$

To determine the applicability of fitting our FRAP recovery curves to the reaction-dominant model described by eqn. 5-3, k_{off} is determined as a function of bleaching spot size for DMPC/NBD-LPC on a phosphorylated surface (Fig 5-7). The reaction dominant model relies upon the assumption that on the timescale of the experiment, diffusion is rapid and can be neglected, however the clear dependence of k_{off} on spot size suggests that for our experimental conditions, the use of the reaction-dominant recovery model is not appropriate. This finding also suggests that for this zwitterionic lipid system, the relationship between binding rates for a given spot size occurs on a slightly faster timescale than diffusion (*i.e.* $k^*_{on}\omega^2/D_f > 1$).[41]

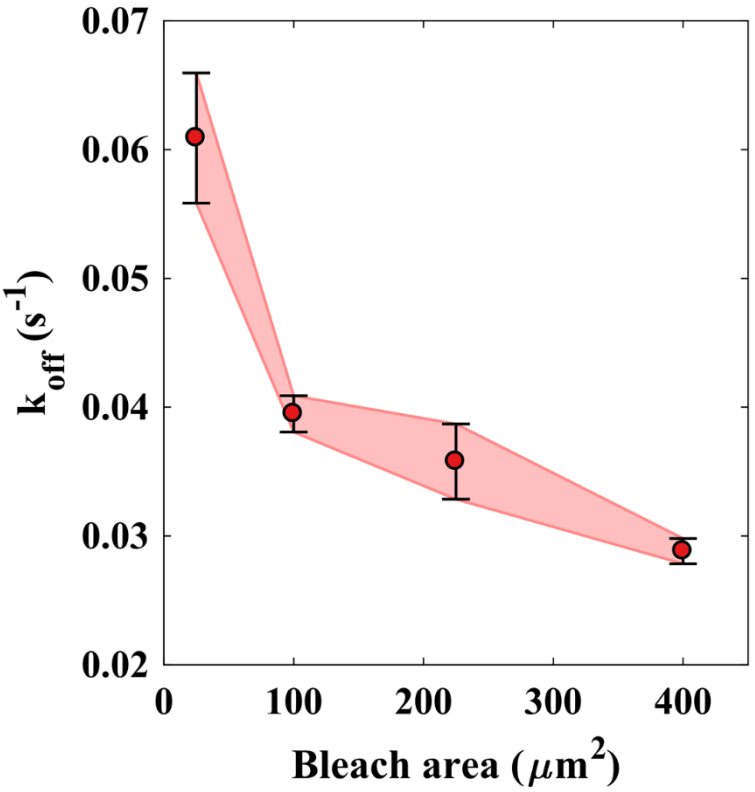

Figure 5-7: Bleaching spot area vs. lipid dissociation rate (k_{off}) determined by the reaction dominant model. Error bars represent 95% confidence interval.

Using this single binding-site model, the FRAP curves were fit using the full reaction-diffusion model described by Sprague *et al*. (eqn. 5-4).[41]

$$frap(t) = L^{-1}\left\{\frac{1}{p} - \frac{F_{eq}}{p}\cdot\left[1 - 2K_1(q\omega)I_1(q\omega)\right]\cdot\left(1 + \frac{k^*_{on}}{p + k_{off}}\right) - \left(\frac{B_{eq}}{p + k_{off}}\right)\right\}$$

$$q = \left[\left(\frac{p}{D_t}\right)\left(1 + \frac{k^*_{on}}{p + k_{off}}\right)\right]^{1/2} \qquad 5\text{-}4$$

$$k^*_{on} = k_{on}[m]$$

Where L^{-1} indicates the inverse Laplace transform of the bracketed function, F_{eq} and B_{eq} are related to k^*_{on} and k_{off} by eqn. A5-8, K_1 and I_1 are the modified Bessel functions, and ω is the radius of the bleaching spot. (A detailed explanation of the equation and mathematics behind the model is shown in appendix section A5.2). Using the full reaction-diffusion model yields the parameters

k_{on}^*, k_{off}, and D_t where k_{on}^* and k_{off} are the rate constants for the lipid-surface binding interactions and D_t is the diffusion constant for the fluorescent probe in the film.

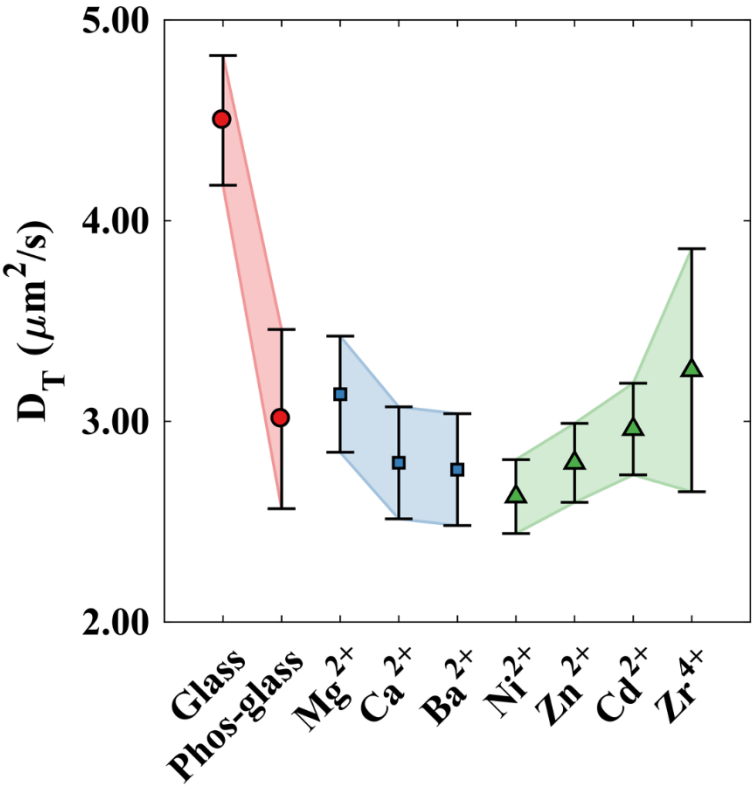

Figure 5-8: Translational diffusion coefficients acquired from fitting the full reaction diffusion model for each prepared surface. Error bars represent 95% confidence interval.

The diffusion constants for each surface are shown in Fig. 5-8 and Table A5-2. The diffusion constant for the DMPC/NBD-LPC monolayer was observed to be the fastest for the unmodified glass surface in the absence of metal ions. The slowed diffusion on the phosphorylated surface is attributed to the increased ionic interactions of the pendent choline (cationic) with the negatively charged phosphate groups. At pH = 7.5 the phosphorylated surface will be more negatively charged than silica, yielding increased interaction between the pendent (cationic) choline and surface.

Interestingly, for both the alkaline earth metals and the transition metal ions, the trend in diffusion constants matches the trend in metal-ligand formation constants (K_f) for complexation with a simple ligand (L), such as methyl-phosphonic acid (MPA) (eqn. 5-5, Fig. 5-9, assuming 1:1 M:L stoichiometry).

$$M + L \rightleftarrows ML$$
$$K_f = \frac{[ML]}{[M][L]} \qquad 5\text{-}5$$

For MPA, pK_{a2} is reported as 7.5 and pK_{a1} is reported as 2.3, while pK_{a1} for DMPC is ~1.[42,30] Given that the phosphonic acid moiety of both MPA and DMPC contribute a -1 charge at pH = 7.5, the interactions are expected to be similar. The same trends were also observed when comparing the diffusion constants to aminoethane-phosphonic acid formation constants. While a correlation between diffusion and K_f does appear to exist, the trend exists within the observed error, indicating that the metal ion-phosphate binding plays a minimal role in driving the diffusion in these systems.

The statistically significant difference among the specified surfaces was determined by one-way ANOVA. Among the different alkaline metal surfaces $F(2,58) = 2.0$, $p = 0.14$ and among differing transition metal ion surfaces $F(3,71) = 3.2$, $p = 0.03$ (Tables A5-3-A5-6). While the observed diffusion coefficients for the transition metal ions show a significant statistical difference and correlate with the metal-ligand formation constants (Fig. 5-9), the percent difference of the diffusion coefficients among the metal surfaces is relatively low (22%). We discuss below how the dominant forces mediating the fluidity in these films are lipid-lipid van der Waals dispersion interactions.

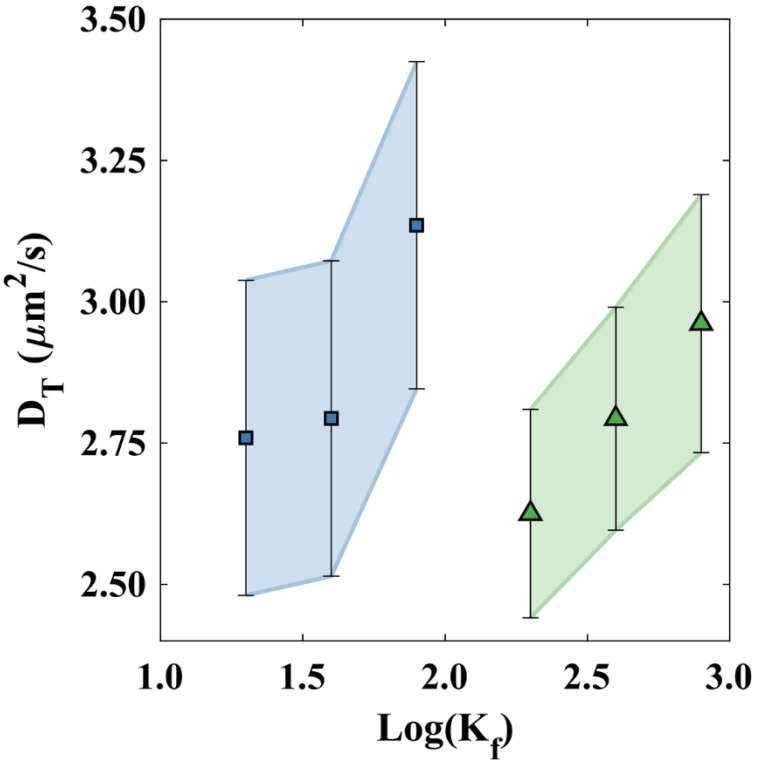

Figure 5-9: Log of formation constants for methylphosphonic acid to each metal ion vs. translational diffusion coefficient. Error bars represent 95% confidence interval.

Ionic interactions are secondary to acyl chain dispersion interactions in mediating film fluidity. To better understand the contributions relating to the binding events occurring at the interface between the PC head-group and the support, we used the full reaction-diffusion model to estimate the free energy of binding for the metal-PC system eqn. 5-6,

$$K_{eq} = k_{on}^{*} / k_{off}$$
$$\Delta G_{MP-L}^{0} = -RT \ln\left(K_{eq}\right) \qquad 5\text{-}6$$

An idealized mechanism for the energies required for diffusion to occur is shown in Fig. 5-10. We find that for the free energy of binding associated with the diffusional measurements ($\Delta G_{MP\text{-}L}$) is ~ -4.4 ± 0.4 kJ/mol. This interaction energy is much less than typical covalent binding

energies and is ~3 times less than estimated dispersive energies between individual lipid tail-groups ($\Delta G_{L\text{-}L}$ ~12-18 kJ/mol-DMPC). [43-44] The translational diffusion can be considered in the context of having two contributions to the activation energy for diffusion, one from ionic interactions between metal and head-group ($E_{MP\text{-}L}$), the other from dispersion interactions between lipid tail-groups ($E_{L\text{-}L}$), and we assert that these factors can be considered as simply additive. We consider that the MP-L and L-L interactions are separable and thus add linearly.

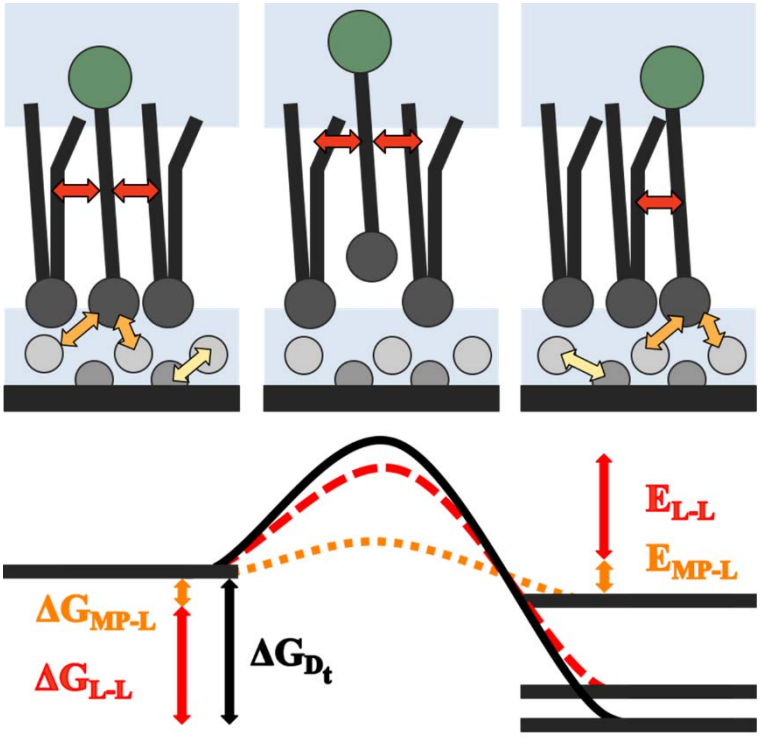

Figure 5-10: Idealized representation of the energies required for the NBD-LPC to undergo translational diffusion in a DMPC layer. The translational diffusion is governed by both an activation energy from the metal phosphonate-lipid interaction ($E_{MP\text{-}L}$) and activation energy from the lipid-lipid van der Waals dispersion interactions ($E_{L\text{-}L}$). The free energy for translational diffusion (ΔG_{Dt}) is therefore governed by the contributions from both metal phosphonate-lipid ($\Delta G_{MP\text{-}L}$) and lipid-lipid interactions ($\Delta G_{L\text{-}L}$).

It is important to note that changing metal ion identity affects both $\Delta G_{MP\text{-}L}$ and $\Delta G_{L\text{-}L}$ due to changes in lipid-lipid spacing and thus dispersion interactions (Fig. 5-5). Using the formation constants from MPA, we find that the free energy of binding associated with the MP-L interactions

is 1.1 ± 0.5 kJ/mol and 2.4 ± 0.3 kJ/mol for the for the alkaline earth metals and transition metal ions, respectively. For a two-chained 14-carbon molecule separated by a distance of 8.6Å, in a hexagonal close packing arrangement, the attractive dispersion energy is expected to be approximately 18 kJ/mol (calculations contained in appendix section A5.5).

Accounting for changes in distances between lipid molecules (Fig. 5-5) due to changes in metal ion identity, and approximating for changes in dispersion energy based on changes in intermolecular distances, we find that the free energy changes associated with changes in metal ion identity are ~6 kJ/mol and ~7 kJ/mol for the for the alkaline earth metals and transition metal ions, respectively. Given that the energies for dispersive forces ($\Delta G_{L\text{-}L}$) are ~2-3 times larger than the energies contributed from the metal to lipid interactions ($\Delta G_{MP\text{-}L}$), we assert that the diffusion is mediated primarily by interactions between the DMPC molecules.

5.4 Conclusions

Despite the zwitterionic and net-neutral nature of the phosphocholine head-groups, interactions between metal-ions introduced into a supporting subphase and the lipids are sufficient to alter the organization and density of the monolayer. This disruption in organization is greater for transition metals than for the alkaline earth metals examined in this study. Contrary to the observed influence of the metal ions on the organization of the lipid monolayers, minimal differences in diffusion were observed. The lack of influence of metal ions in the sub-layer is attributed to the majority of diffusion being mediated by lipid-lipid interactions and van der Waals dispersion interactions rather than by binding interactions with the metal ions and surface moieties. Experimental studies are currently underway examining the influence of lipid-lipid interactions to provide a cohesive and quantitative understanding of the individual contributions at play.

APPENDIX

APPENDIX

A5.1 XPS Analysis

To determine the expected ratio between metal and phosphorus mediated by the surface or lipid, we first estimate the total number of phosphorus present:

$$P_{Total} = P_{Surface} + P_{Lipid} \quad \text{A5-1}$$

The content of surface phosphorus is estimated assuming complete phosphorylation of all present surface hydroxides (5-8 OH/nm^2).[45-47] The phosphorus content provided from the lipids is estimated using the known mean molecular area from the Langmuir isotherms. At 25mN/m the average molecular area is *ca.* 69 Å^2/molecule (0.69 nm^2/molecule), at 1 P/Lipid this represents 1.4 P/nm^2. The ratio of metal to phosphorus is given by:

$$M^{x+} : P = \frac{M^{x+}}{P_{Total}} \quad \text{A5-2}$$

Assuming a surface mediated transfer and a 1:1 ratio of metal ion to surface phosphorus:

$$M^{x+} = P_{Surface} \quad \text{A5-3}$$

Assuming a lipid mediated transfer and a 1:1 ratio of metal ion to lipid phosphorus:

$$M^{x+} = P_{Lipid} \quad \text{A5-4}$$

Given these set of assumptions, the expected M^{x+}:P ratio for a surface mediated transfer process is 0.78 for 5 P/nm^2 and 0.85 for 8 P/nm^2 yielding an estimated ratio 0.82 +/- 0.04.

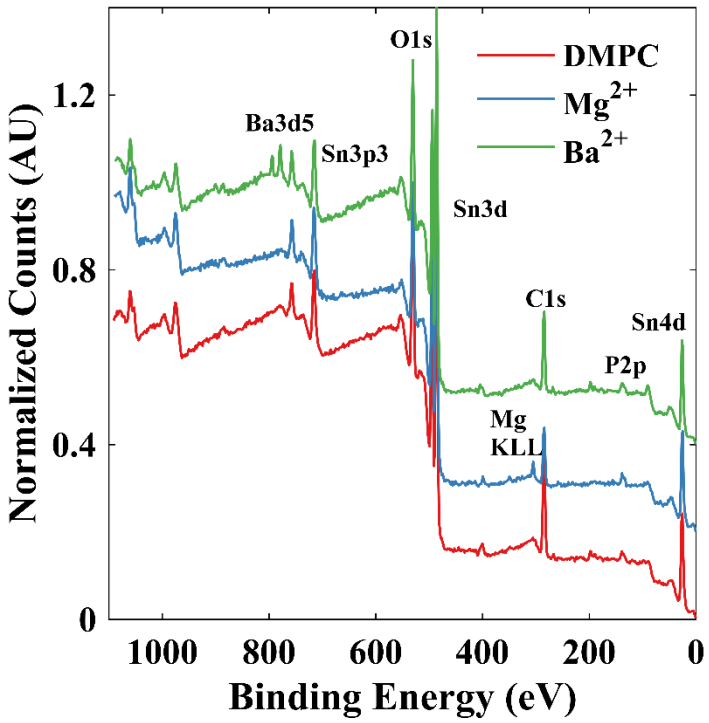

Figure A5-1: XPS survey spectra of DMPC (red), Mg^{2+} (blue), and Ba^{2+} (green) are shown.

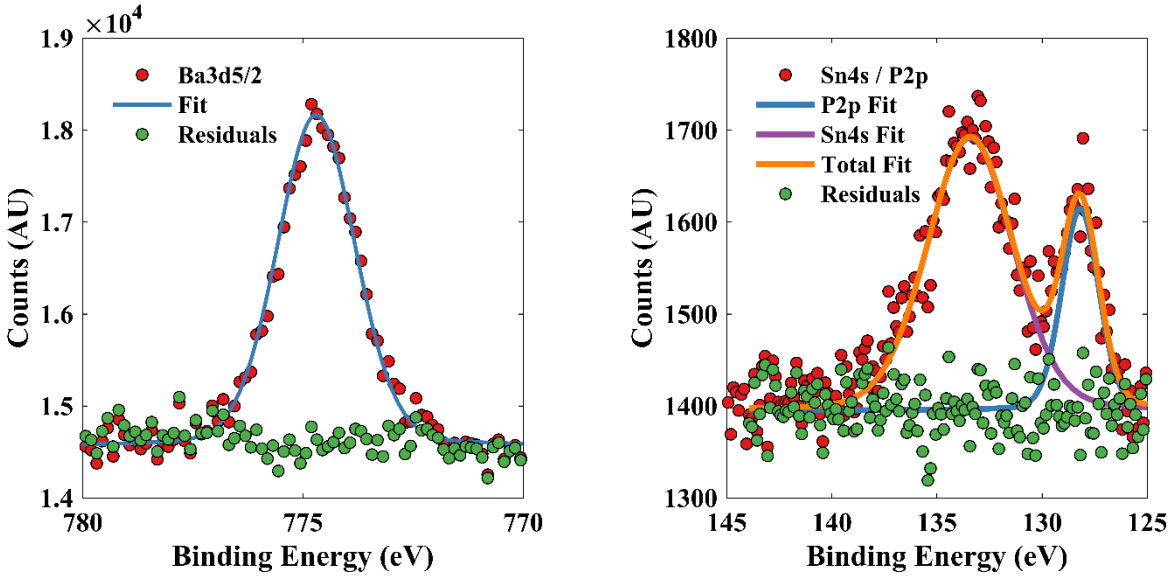

Figure A5-2: (left). Fit of the XPS spectral data for a DMPC/NBD-LPC film containing Ba^{2+} is shown. The Ba3d5/2 peak is fit to a Gaussian-Lorentzian curve after Shirley background subtraction. Figure A5-3: (right). Representative convoluted fits for the overlapping Sn4s and P2p peaks on the Ba^{2+}/DMPC/NBD-LPC film.

A5.2 Analysis of FRAP curves by the Full Reaction-Diffusion Model

The FRAP curves were fit using the full reaction-diffusion model described by Sprague et. Al.[41] We briefly summarize the model system described by Sprague and relate the assumptions and equations to our lipid film system below. The analysis starts with a simple single binding site model eqn. A5-5:

$$F + M \underset{k_{off}}{\overset{k_{on}}{\rightleftarrows}} B \qquad \text{A5-5}$$

where $F = [f]$ represents the concentration of free diffusing molecule (NBD-LPC), $M = [m]$ represents the concentration of available binding site (adsorbed metal ions), and $B = [b]$ represents the concentration of bound complex between NBD-LPC and the adsorbed metal.

Assuming the system has reached equilibrium prior to the bleaching event, and that the binding sites are immobile, the recovery can be described by a set of coupled reaction-diffusion equations eqn. A5-6:

$$\frac{\partial f}{\partial t} = D_t \nabla^2 f - k_{on}^* f + k_{off} b$$
$$\frac{\partial b}{\partial t} = k_{on}^* f + k_{off} b \qquad \text{A5-6}$$

where D_t is the diffusion constant of the NBD-LPC, $k^*_{on} = k^*_{on}[m]$ is the pseudo first-order rate constant derived by assuming that the $M = [m]$ is constant, and ∇^2 is the Laplacian operator. In the case presented here, both assumptions are assumed valid. The surfaces were allowed to equilibrate ~10 minutes prior to imaging and a period of 10 seconds was collected prior to the bleaching event to assure equilibrium was reached. The binding sites in this case are considered to be any binding interaction with the surface and the surface is assumed to be immobile on the timescale of the measurement.

Because the system is at equilibrium at the start of the FRAP experiment both *F* and *B* are at equilibrium:

$$\frac{df}{dt} = \frac{db}{dt} = 0$$
$$k_{on}^{*} F_{eq} = k_{off} B_{eq} \qquad \text{A5-7}$$

Assuming normalization of the FRAP curves, the final recovery of the free and bound species is equal to:

$$F_{eq} + B_{eq} = 1$$
$$F_{eq} = \frac{k_{off}}{k_{on}^{*} + k_{off}}, B_{eq} = \frac{k_{on}^{*}}{k_{on}^{*} + k_{off}} \qquad \text{A5-8}$$

One way to analytically solve the reaction-diffusion differential equations is to take the Laplace transform of the coupled equations. The inverse Laplace transform was performed using the matlab function *invlap.m* on the analytical equation:

$$frap(t) = \mathcal{L}^{-1}\left\{\frac{1}{p} - \frac{F_{eq}}{p}\cdot\left[1 - 2K_1(q\omega)I_1(q\omega)\right]\cdot\left(1 + \frac{k_{on}^{*}}{p + k_{off}}\right) - \left(\frac{B_{eq}}{p + k_{off}}\right)\right\} \qquad \text{A5-9}$$

where *frap(t)* is recovered by taking the inverse Laplace transform, F_{eq} and B_{eq} are related to k^{*}_{on} and k_{off} by eqn. 4, K_1 and I_1 are the modified bessel functions, ω is the radius of the bleaching spot and *q* is described by eqn. A5-10:

$$q = \sqrt{\left(\frac{p}{D_f}\right)\left(1 + \frac{k_{on}^{*}}{p + k_{off}}\right)} \qquad \text{A5-10}$$

A5.3 FRAP Recovery Curves and Fitting

The FRAP recoveries were fit using the matlab routine *lsqcurvefit.m* with Eqs. A5-9 & A5-10 for the full reaction-diffusion model. After fitting, the FRAP recoveries were averaged for each

surface and are shown in Table A5-1 for the dissociation constant k_{off}, and Table A5-2 for the diffusion coefficient D_T.

Table A5-1: Dissociation constant (*koff*) data acquired by fitting FRAP curves with the reaction-dominant model.

Surface	N	Mean k_{off} (10^{-3} s^{-1})	Std. Dev.	Std. Error	95% Confidence Interval for Mean Upper Bound	95% Confidence Interval for Mean Lower Bound	Minimum	Maximum
SiO_x	19	26.8	13.2	5.9	20.8	32.7	3.3	57.0
PO_x-SiO_x	20	27.2	18.3	8.0	19.1	35.2	0.1	55.4
Mg	19	34.3	22.3	10.0	24.2	44.3	1.0	68.6
Ca	22	32.9	20.2	8.4	24.5	41.3	0.0	75.3
Ba	18	26.7	18.7	8.6	18.0	35.3	2.5	77.0
Ni	21	39.1	20.6	8.8	30.2	47.9	2.4	75.7
Zn	25	28.9	15.4	6.0	22.8	34.9	2.8	78.0
Cd	17	29.9	24.9	11.9	18.0	41.7	1.5	84.4
Zr	9	27.1	15.7	10.2	16.9	37.3	7.7	52.1

Table A5-2: Diffusion coefficient data acquired by fitting FRAP curves with the full reaction-diffusion model.

Surface	N	Mean (D_T)	Std. Dev.	Std. Error	95% Confidence Interval for Mean Upper Bound	95% Confidence Interval for Mean Lower Bound	Minimum	Maximum
SiO_x	19	4.50	0.72	0.32	4.18	4.82	3.53	6.17
PO_x-SiO_x	20	3.01	1.02	0.45	2.56	3.46	1.69	5.20
Mg	19	3.14	0.64	0.29	2.85	3.42	2.24	4.40
Ca	22	2.79	0.67	0.28	2.51	3.07	1.67	4.03
Ba	18	2.76	0.60	0.28	2.48	3.04	1.86	3.91
Ni	21	2.63	0.43	0.18	2.44	2.81	1.89	3.62
Zn	25	2.79	0.50	0.20	2.60	2.99	1.79	3.74
Cd	17	2.96	0.48	0.23	2.73	3.19	2.33	4.07
Zr	9	3.25	0.93	0.61	2.65	3.86	1.90	4.58

A5.4 One-way ANOVA Testing of the Fitted Results

One-way ANOVA analysis was performed on the series of FRAP recoveries for each surface. The average results for each surface are shown as a box plot in Figure A5-4. The central

red mark represents the median and the edges of the box represent the 25th and 75th percentiles of the data. Whiskers are shown to extend to the most extreme data points, where outliers are represented individually. The notches in the plot correspond to the 95% confidence interval, where if the notches of one surface do not overlap another surface, the two medians are significantly different to 95% confidence.

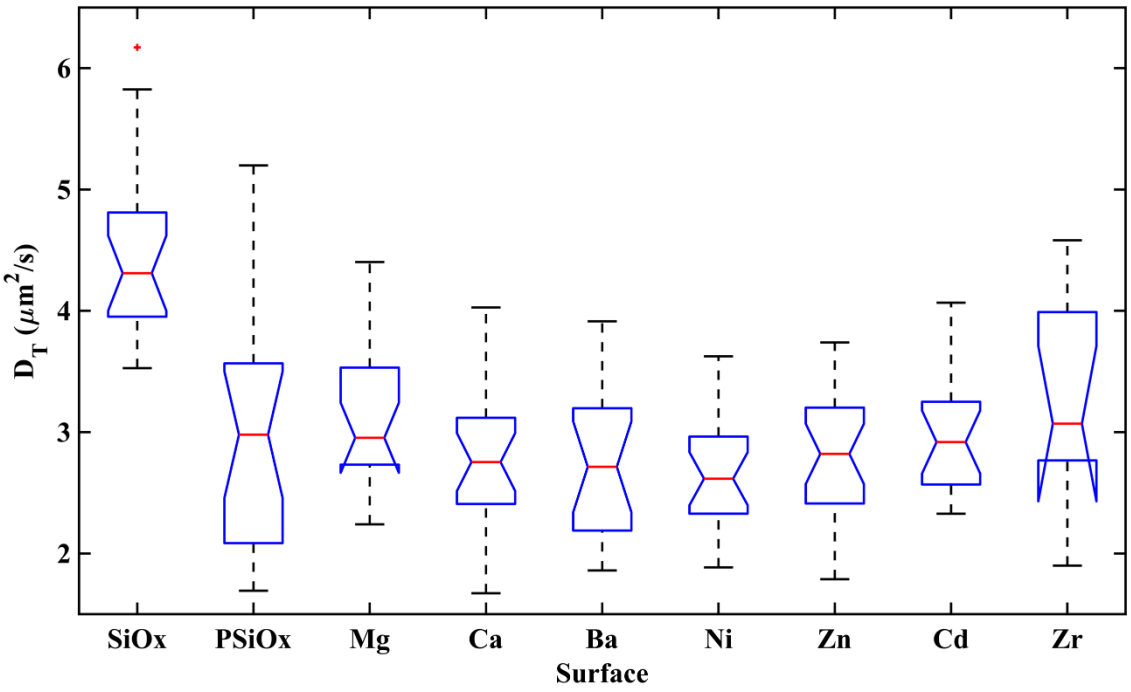

Figure A5-4: Box plot for the fitted diffusion coefficients of all trials on each surface. The red line represents median, whiskers represent maximum and minimum values, and red asterisks are considered outliers. Notches in the box plot represent 95% confidence intervals for each surface.

Using a Chi-Square goodness-of-fit test to the 5% significance level, trials for each surface were normally distributed and ANOVA analysis was performed. ANOVA analyses are shown for all surfaces (Table A5-3), among all metal surfaces (Table A5-4), among the alkaline metals only (Table A5-5), and among the heavy metals only (Table A5-6).

Table A5-3: One-way ANOVA test among all surfaces.

	Sum of Squares	df	Mean Square	F	Significance
Between Surfaces	49.0	8.0	6.1	13.5	6.9E-15
Within Surfaces	72.9	161.0	0.5		
Total	121.9	169.0			

Table A5-4: One-way ANOVA test among all metal surfaces.

	Sum of Squares	df	Mean Square	F	Significance
Between Surfaces	4.6	6.0	0.8	2.2	5.0E-02
Within Surfaces	43.3	124.0	0.3		
Total	47.9	130.0			

Table A5-5: One-way ANOVA test among alkaline metal surfaces

	Sum of Squares	df	Mean Square	F	Significance
Between Surfaces	1.7	2.0	0.8	2.0	0.14
Within Surfaces	23.0	56.0	0.4		
Total	24.7	58.0			

Table A5-6: One-way ANOVA test among heavy metal surfaces.

	Sum of Squares	df	Mean Square	F	Significance
Between Surfaces	2.82	3.00	0.94	3.2	0.03
Within Surfaces	20.34	68.00	0.30		
Total	23.16	71.00			

A5.5 Interaction Energy Calculations

The interaction energy between the DMPC molecules was estimated by a summation of the dispersive energies between two parallel (two-chained) 14-carbon alkyl chains.[43-44] The dispersion attraction energy (W_{DMPC}) between two parallel saturated DMPC chains is given by:

$$W_{DMPC} = \alpha \frac{3\pi N}{8\lambda D^5} \qquad \text{A5-11}$$

where α is the interaction energy between two methylene units, *N* is the number of methylene units (14 for DMPC), λ is the length of the individual methylene units (1.26Å), and D is the separation distance between chains (calculated from the mean molecular area isotherms at the transfer pressure of 25mN/m).

The total interaction energy in the monolayer case assumes a hexagonal close packing arrangement and is a summation of attractive energies from the first closest interacting group at radius, r_1, to the nth group at a radius of r_n, where r is the interchain separation distance calculated from the radius of the mean molecular area isotherms at the transfer pressure.

$$r_n = 2nr$$
$$W_M = 2 \cdot \left(\sum_1^n N_n W_{DMPC}(r_n) - W_{DMPC}(r_1) \right) \qquad \text{A5-12}$$

where N_n is the number of nearest neighbors (i.e. $N_1 = 6$), and $W_{DMPC}(r_n)$ is the DMPC interaction energy at a separation distance of r_n and all summations have been made to n=12.

REFERENCES

REFERENCES

1. Blodgett, K. B., Films built by depositing successive monomolecular layers on a solid. *J. Am. Chem. Soc.* **1935,** *57* (6), 1007-1022.

2. Langmuir, I., The adsorption of gases on plane surfaces of glass, mica and platinum. *J. Am. Chem. Soc.* **1918,** *40* (9), 1361-1403.

3. Langmuir, I.; Schaefer, V. J., Activities of Urease and Pepsin Monolayers. *Journal of the American Chemical Society* **1938,** *60* (6), 1351-1360.

4. Leonenko, Z. V.; Carnini, A.; Cramb, D. T., Supported planar bilayer formation by vesicle fusion: the interaction of phospholipid vesicles with surfaces and the effect of gramicidin on bilayer properties using atomic force microscopy. *Biochimica et Biophysica Acta (BBA) - Biomembranes* **2000,** *1509* (1–2), 131-147.

5. Tamm, L. K.; McConnell, H. M., Supported Phospholipid Bilayers. *Biophysical Journal* **1985,** *47*, 105-113.

6. Richter, R. P.; Bérat, R.; Brisson, A. R., Formation of solid-supported lipid bilayers: An integrated view *Langmuir* **2006,** *22*, 3497-3505.

7. Beneš, M.; Billy, D.; Benda, A.; Speijer, H.; Hof, M.; Hermans, W. T., Surface-dependent transitions during self-assembly of phospholipid membranes on mica, silica, and glass. *Langmuir* **2004,** *20*, 10129-10137.

8. Starr, T. E.; Thompson, N. L., Formation and characterization of planar phospholipid bilayers supported on TiO2 and SrTiO3 single crystals. *Langmuir* **2000,** *16*, 10301-10308.

9. Xu, J.; Stevens, M. J.; Oleson, T. A.; Last, J. A.; Sahai, N., Role of Oxide Surface Chemistry and Phospholipid Phase on Adsorption and Self-Assembly: Isotherms and Atomic Force Microscopy. *J. Phys. Chem. C* **2009,** *113*, 2187-2196.

10. Liu, J., Interfacing zwitterionic liposomes with inorganic nanomaterials: Surface forces, membrane integrity, and applications. *Langmuir* **2016,** *32*, 4393-4404.

11. Cremer, P. S.; Boxer, S. G., Formation and Spreading of Lipid Bilayers on Planar Glass Supports. *Journal of Physical Chemistry B* **1999,** *103*, 2554.

12. Ekeroth, J.; Konradsson, P., Bivalent-Ion-Mediated Vesicle Adsorption and Controlled Supported Phospholipid Bilayer Formation on Molecular Phosphate and Sulfate Layers on Gold. *Langmuir* **2002,** *18*, 7923-7929.

13. Ralf Richter, A. M., Alain Brisson, Pathways of Lipid Vesicle Deposition on Solid Surfaces: A Combined QCM-D and AFM Study. *Biophysical Journal* **2003,** *85*, 3035-3047.

14. Richter, R. P.; Brisson, A. R., Following the Formation of Supported Lipid Bilayers on Mica: A Study Combining AFM, QCM-D, and Ellipsometry. *Biophysical Journal* **2005,** *88*, 3422-3433.

15. Reviakine, I.; Simon, A.; Brisson, A., Effect of Ca2+ on the morphology of mixed DPPC-DOPS supported phospholipid bilayers. *Langmuir* **2000,** *16*, 1473-1477.

16. Reviakine, I.; Brisson, A., Formation of supported phospholipid bilayers from unilamellar vesicles investigated by atomic force microscopy. *Langmuir* **2000,** *16*, 1806-1815.

17. Seantier, B.; Kasemo, B., Influence of Mono- And Divalent Ions on the Formation of Supported Phospholipid Bilayers via Vesicle Adsorption. *Langmuir* **2009,** *25*, 5767-5772.

18. Dacic, M.; Jackman, J. A.; Yorulmaz, S.; Zhdanov, V. P.; Kasemo, B.; Cho, N.-J., Influence of Divalent Cations on Deformation and Rupture of Adsorbed Lipid Vesicles. *Langmuir* **2016,** *32* (25), 6486-6495.

19. Cho, N.-J.; Jackman, J. A.; Liu, M.; Frank, C. W., pH-Driven Assembly of Various Supported Lipid Platforms: A Comparative Study on Silicon Oxide and Titanium Oxide. *Langmuir* **2011,** *27* (7), 3739-3748.

20. Oberts, B. P.; Blanchard, G. J., Headgroup-Dependent Lipid Self-Assembly on Zirconium Phosphate-Terminated Interfaces†. *Langmuir* **2009,** *25* (24), 13918-13925.

21. Oberts, B. P.; Blanchard, G. J., Ionic Binding of Phospholipids to Interfaces: Dependence on Metal Ion Identity. *Langmuir* **2009,** *25* (22), 13025-13033.

22. Seu, K. J.; Pandey, A. P.; Haque, F.; Proctor, E. A.; Ribbe, A. E.; Hovis, J. S., Effect of Surface Treatment on Diffusion and Domain Formation in Supported Lipid Bilayers. *Biophysical Journal* **2007,** *92* (7), 2445-2450.

23. Scomparin, C.; Lecuyer, S.; Ferreira, M.; Charitat, T.; Tinland, B., Diffusion in supported lipid bilayers: Influence of substrate and preparation technique on the internal dynamics. *The European Physical Journal E* **2008,** *28* (2), 211-220.

24. Johnson, S. J.; Bayerl, T. M.; McDermott, D. C.; Adam, G. W.; Rennie, A. R.; Thomas, R. K.; Sackmann, E., Structure of an adsorbed dimyristoylphosphatidylcholine bilyaer measured with specular reflection of neutrons. *Biophysical Journal* **1991,** *59*, 289-294.

25. Castellana, E. T.; Cremer, P. S., Solid supported lipid bilayers: From biophysical studies to sensor design. *Surface Science Reports* **2006,** *61* (10), 429-444.

26. Jackman, J. A.; Tabaei, S. R.; Zhao, Z.; Yorulmaz, S.; Cho, N.-J., Self-Assembly Formation of Lipid Bilayer Coatings on Bare Aluminum Oxide: Overcoming the Force of Interfacial Water. *ACS Applied Materials & Interfaces* **2015,** *7* (1), 959-968.

27. Jackman, J. A.; Zan, G. H.; Zhao, Z.; Cho, N.-J., Contribution of the Hydration Force to Vesicle Adhesion on Titanium Oxide. *Langmuir* **2014,** *30* (19), 5368-5372.

28. Phair, R. D.; Gorski, S. A.; Misteli, T., Measurement of dynamic protein binding to chromatin *in vivo*, using photobleaching microscopy. *Meth. Enzymol.* **2004,** *375*, 393-414.

29. Kundu, S.; Langevin, D., Fatty acid monolayer dissociation and collapse: Effect of pH and cations. *Colloids and Surfaces A: Physicochemical and Engineering Aspects* **2008,** *325*, 81-85.

30. Marsh, D., *CRC handbook of lipid bilayers*. CRC Press: Boca Raton, FL, 1990.

31. Davis, J. E.; Rahaman, O.; Patel, S., Molecular dynamics simulations of a DMPC bilayer using nonadditive interaction models. *Biophys J* **2009,** *96* (2), 385-402.

32. Stern, H. A.; Feller, S. E., Calculation of the dielectric permittivity profile for a nonuniform system: Application to a lipid bilayer simulation. *The Journal of Chemical Physics* **2003,** *118* (7), 3401.

33. McLaughlin, S., The electrostatic properties of membranes. *Annual review of biophysics and biophysical chemistry* **1989,** *18*, 113-136.

34. Bloch, J. M.; Wenbing, Y., Condensation of monovalent and divalent metal ions on a Langmuir monolayer. *Physical Review A* **1990,** *41*, 844-862.

35. Vaknin, D.; Travesset, A., Bjerrum pairing correlations at charged interfaces. *Europhysics Letters* **2006,** *74*, 181-187.

36. *CRC Handbook of Chemistry and Physics, 96th Ed.* CRC Press: Boca Raton, FL, 2016.

37. Major, J. S.; Blanchard, G. J., Covalently Bound Polymer Multilayers for Efficient Metal Ion Sorption. *Langmuir* **2001,** *17* (4), 1163-1168.

38. Tulock, J. J.; Blanchard, G. J., Investigating Hydrolytic Polymerization of Aqueous Zirconium Ions Using the Fluorescent Probe Pyrenecarboxylic Acid. *The Journal of Physical Chemistry B* **2002,** *106* (14), 3568-3575.

39. Soumpasis, D. M., Theoretical analysis of fluorescence photobleaching recovery experiments. *Biophysical Journal* **1983,** *41*, 95-97.

40. Bulinski, J. C.; Odde, D. J.; Howell, B. J.; Salmon, T. D.; Waterman-Storer, C. M., Rapid dynamics of the microtubule binding of ensconsin in vivo. *Journal of Cell Science* **2001,** *114*, 3885-3897.

41. Sprague, B. L.; Pego, R. L.; Stavreva, D. A.; McNally, J. G., Analysis of Binding Reactions by Fluorescence Recovery after Photobleaching *Biophysical Journal* **2004,** *86*, 3473-3495.

42. Popov, K.; Ronkkomaki, H.; Lajunen, L. H., Critical Evaluation of Stability Constants of Phosphonic Acids. *Pure Applied Chemistry* **2001,** *73*, 1641-1677.

43. Shapiro, E.; Ohki, S., The Interaction Energy Between Hydrocarbon Chains. *Journal of Colloid and Interface Science* **1973,** *47*, 38-49.

44. Salem, L., Attractive Forces between Long Saturated Chains at Short Distances. *Journal of Chemical Physics* **1962,** *37*, 2100-2113.

45. Zhuravlev, L. T., Concentration of hydroxyl groups on the surface of amorphous silicas. *Langmuir* **1987,** *3* (3), 316-318.

46. Zhuravlev, L. T., The surface chemistry of amorphous silica. Zhuravlev model. *Colloids and Surfaces A: Physicochemical and Engineering Aspects* **2000,** *173* (1-3), 1-38.

47. McCafferty, E.; Wightman, J. P., Determination of the concentration of surface hydroxyl groups on metal oxide films by a quantitative XPS method. *Surface and Interface Analysis* **1998,** *26* (8), 549-564.

CHAPTER 6: CONCLUSIONS AND FUTURE DIRECTIONS

6.1 Conclusions and Future Directions

The goal of this research has been to better understand how the molecular scale interactions at play in a supported model membrane system affect the dynamical properties. The motivation for this work is the creation of fluid and robust thin films with a wide range of properties for applications such as chemical sensing, separations, self-healing membranes, molecular electronics, and tribology. The use of these films for such applications is attractive, but is currently limited due to the incomplete understanding of the interplay between interfacial and intermolecular interactions that ultimately give rise to the dynamic properties. Bulk-scale properties are often inferred from molecular scale viscosity measurements (fluorescence anisotropy decay) or bulk-scale measurements are made inferring molecular scale properties. Understanding the interactions that are operative in mediating the dynamical properties over a large range of length scales will allow for the tailoring of these films to the desired set of applications.

The focus of the work contained within this dissertation has been on biomimetic model membrane systems for applications in chemical sensing and separations. These systems often rely on transmembrane proteins as the chemically selective or transducing agent. There are a variety of methods used to prepare and examine biomimetic membrane systems including unsupported systems such as black lipid membranes,[1-3] lipid vesicles,[4-7] and supported systems such as solid supported,[8-10] and hybrid bilayer membranes.[11-13] This work has focused on the use of solid supported model membranes due to the diversity of chemical means available to control the dynamical properties such as: pH, presence and identity of metal ions in the subphase and buffer overlayer, surface composition and roughness, as well as the necessity of a solid support for transfer of the chemical response information of interest from the chemically selective element to the detector.

In Chapter 2 of this dissertation, the instrumental methods used to examine the morphology and dynamical properties of supported model membranes systems is described with a focus on the measurement of rotational and translational diffusion behavior of fluorescent probe molecules. Brewster angle microscopy (BAM) is introduced as a means to observe changes in the morphology of amphiphilic molecules such as alkanoic and alkyl phosphonic acids, or lipids, at an air/water interface as a function of pressure applied to form a monolayer and under a variety of chemical and physical conditions. Fluorescence Anisotropy Decay Imaging (FADI) is introduced as a means to spatially resolve variations in the fluorescence anisotropy decay dynamics of monolayer or bilayer films. The information available from these measurements allow for a quantitative measurement of the rotational diffusion properties of a fluorescent probe molecule, as well as changes in film morphology due to compositional changes of the supporting surface or organic monolayer. Lastly, methodology for the examination of Fluorescence Recovery After Photobleaching (FRAP) measurements is described. FRAP dynamics depend on the type of fluorescent probe used, the morphology of the interfacial layer and any surface-adlayer interactions. A variety of functional models are considered to best model the observed data, with a goal of obtaining translational diffusion constants, and association/dissociation rate constants for interfacial binding site events.

In Chapter 3 we reported on changes to the rotational diffusion dynamics of perylene within a tethered lipid monolayer.[14] The data revealed slowed dynamics in the lipid monolayer exposed to air compared to more rapid diffusional dynamics when immersed in aqueous solution. The central question in these findings is why the addition of an aqueous adlayer increases the motional freedom of the chromophore. The decrease in rotational diffusion time constant of perylene imbedded in a lipid monolayer covered by an aqueous overlayer is likely associated with a change

in the extent of organization of the lipid acyl chain region upon exposure to the aqueous overlayer. Electrochemical data indicating *ca.* 52% coverage of the lipid monolayer suggests there is ample spatial heterogeneity available for reorganization to occur. Ellipsometric and contact angle data are consistent with a nonpolar and spatially heterogeneous lipid (sub)monolayer interface. Unfortunately, based on the measurements made, little information is available on the length scale(s) of the organized regions at the interface. Future studies using chromophores with different aspect ratios (*e.g.* DPH)[15] may shed light on the degree of lipid acyl chain conformational organization. Additionally, at the time these measurements were made, both the FRAP and FADI instruments were not yet available in the Blanchard lab. Reexamination of these films using confocal fluorescence imaging (FRAP and FADI) could provide substantially more insight into the characteristic organizational domain sizes of such interfaces.

The work described in Chapter 4 investigated the dynamics of a tethered BODIPY chromophore contained within an alkylphosphonic acid LB film.[16] The goal of this work was to quantitate both the fluidity and adhesion strength of the organic adlayer to the interface using the combination of translational and rotational diffusion data. By examining the diffusional behavior of this tethered chromophore over length scales ranging from molecular (FADI measurements) through macroscopic (μm-to-mm, FRAP measurements), we demonstrated a direct and novel means for evaluating organic adlayer binding strength to a supporting surface. Using steady state and fluorescence lifetime imaging data, we were able to determine the motional freedom that is characteristic of the BODIPY chromophore and the effect of aggregation on molecular motion within the ODPA film. The data provided insight into the binding strength of a barium phosphonate species to a silica surface and, by extension, provide an estimate of the binding strength for related interfaces. We observed binding strengths from ΔG_{dis}, of *ca*. 20 kJ/mol. This

value is entirely consistent with interactions dominated by H-bonding[17] and there is also an observed chromophore concentration dependence suggesting some information on the interaction energy of the aggregated chromophores.

The strength of interaction for our monolayer containing barium with a silica support is very similar to the binding interactions responsible for the formation of alkanethiol monolayers on gold and mercury.[18-20] This finding is important because the spectroscopic evaluation of chromophore dynamics in an alkanethiol/gold SAM are limited by chromophore quenching due to the presence of a metal support,[21] and this method offers a way to estimate the expected dynamics for this family of systems.

Studies examining the role of chemical modification of the support as a means of controlling binding strength were performed in Chapter 5, however there remain a few unanswered questions pertaining to the system at hand. Even at the lower chromophore concentrations, some aggregation was present. The aggregation of chromophore is likely due to the dissimilar chemical structure between the ODPA and BODIPY probe molecule. To mitigate aggregation, preparation of a film with a chromophore similar to the chemical structure of the film is suggested for future studies. In addition, the combination of barium and ODPA was found to provide measurable diffusional properties on the timescale of minutes. Examination of a combination of ODPA and other metal systems were examined including Ca^{2+} and Cd^{2+}, however diffusion was slow (tens of minutes) and very little recovery was observed. These observations provide some key guidelines in the preparation of fluid and robust films, which will be discussed below.

Chapter 5 examined the role of chemical modification of the support via combination of phosphorylation of the support surface and varying the metal ion identity between the phosphorylated surface and organic adlayer as a means of controlling binding strength.[22] X-ray

photoelectron spectroscopy (XPS) was utilized to measure semi-quantitatively the amount of metal ions transferred during deposition of the films. Fluorescence recovery after photobleaching (FRAP) revealed the translational diffusion properties of the BLPA chromophore after deposition onto a solid support. The addition of metal ions into the subphase was sufficient to alter the organization and density of the amphiphile monolayer at the air/water interface, despite the net-neutral character of the zwitterionic DMPC lipid. The disruption was found to be significantly greater for the transition metal ions relative to the alkaline earth metals examined in the study. Despite the observed influence of the metal ions on the organization of the lipid monolayers at the air/water interface, minimal differences in diffusion were observed upon transfer to a supporting surface. Given the observed transfer to, and presence of the metal ions at the supporting interface, the lack of influence of metal ions is attributed to diffusion being mediated by lipid-lipid interactions and van der Waals dispersion interactions.

The work presented in this dissertation shows both the ability to measure quantitatively the fluidity and binding strengths associated with supporting model membrane systems at a solid interface, and hints toward the ability to control the fluid and adhesion properties based on modification of the solid support. This work provides a few key lessons to guide future investigations of these types of systems. (i.) The addition of an aqueous adlayer at the organic interface disrupts organization of the alkyl region, but is essential for diffusional measurements to be made. (ii.) Chromophores should be chosen with chemical structure similar to the amphiphile used in the film formation if aggregation is to be mitigated. (iii.) The addition of different metal ions into the subphase shows promise as a means of modulating film fluidity and adhesion.

One area for future investigation should be to understand the role of the lipid-lipid chain interactions relative to the binding constants to the metal ions. This can be accomplished by

changing the charge associated with the amphiphile headgroup, changing the lipid chain length, or changing the degree of saturation in the lipid acyl chain region to increase interchain distances and thereby limit dispersion interactions. Additional studies can be performed examining the temperature dependence of dynamics and morphology in these systems. Changes in temperature will likely give rise to changes in surface-lipid, lipid-lipid, and lipid-chromophore interactions. Further changes in the supporting surface charge or spatial charge distribution via changes in the metal oxide used for the support, or electrical bias of the interface could provide further control over the fluidity and adhesion. A quantitative understanding of the interplay between the physical interactions involved at these interfaces will open the door to a general way to tailor systems with desired adhesion and diffusion properties for the required application.

REFERENCES

REFERENCES

1. Montal, M.; Mueller, P., Formation of bimolecular membranes from lipid monolayers and a study of their electrical properties. *Proc Natl Acad Sci U S A* **1972,** *69* (12), 3561-6.

2. Mueller, P.; Rudin, D. O.; Tien, H. T.; Wescott, W. C., Reconstitution of cell membrane structure in vitro and its transformation into an excitable system. *Nature* **1962,** *194*, 979-80.

3. Mueller, P.; Wescott, W. C.; Rudin, D. O.; Tien, H. T., Methods for Formation of Single Bimolecular Lipid Membranes in Aqueous Solution. *J Phys Chem-Us* **1963,** *67* (2), 534-535.

4. Hope, M. J.; Bally, M. B.; Mayer, L. D.; Janoff, A. S.; Cullis, P. R., Generation of Multilamellar and Unilamellar Phospholipid-Vesicles. *Chemistry and Physics of Lipids* **1986,** *40* (2-4), 89-107.

5. Hope, M. J.; Bally, M. B.; Webb, G.; Cullis, P. R., Production of Large Unilamellar Vesicles by a Rapid Extrusion Procedure - Characterization of Size Distribution, Trapped Volume and Ability to Maintain a Membrane-Potential. *Biochimica Et Biophysica Acta* **1985,** *812* (1), 55-65.

6. Mayer, L. D.; Bally, M. B.; Hope, M. J.; Cullis, P. R., Techniques for Encapsulating Bioactive Agents into Liposomes. *Chemistry and Physics of Lipids* **1986,** *40* (2-4), 333-345.

7. Mayer, L. D.; Hope, M. J.; Cullis, P. R., Vesicles of Variable Sizes Produced by a Rapid Extrusion Procedure. *Biochimica Et Biophysica Acta* **1986,** *858* (1), 161-168.

8. Tamm, L. K.; Mcconnell, H. M., Supported Phospholipid-Bilayers. *Biophys J* **1985,** *47* (1), 105-113.

9. Trojanowicz, M., Miniaturized biochemical sensing devices based on planar bilayer lipid membranes. *Fresen J Anal Chem* **2001,** *371* (2), 246-260.

10. Richter, R. P.; Berat, R.; Brisson, A. R., Formation of solid-supported lipid bilayers: An integrated view. *Langmuir* **2006,** *22* (8), 3497-3505.

11. Plant, A. L., Self-Assembled Phospholipid Alkanethiol Biomimetic Bilayers on Gold. *Langmuir* **1993,** *9* (11), 2764-2767.

12. Plant, A. L., Supported hybrid bilayer membranes as rugged cell membrane mimics. *Langmuir* **1999,** *15* (15), 5128-5135.

13. Plant, A. L.; Tarlov, M., Self-Assembled Monolayers as Substrates for Planar Model Membranes. *Biophys J* **1993,** *64* (2), A298-A298.

14. Baumler, S. M.; Blanchard, G. J., Lipid adlayer organization mediated by a liquid overlayer. *Spectrochim Acta A* **2012,** *98*, 429-435.

15. Mitchell, D. C.; Litman, B. J., Effect of Cholesterol on Molecular Order and Dynamics in Highly Polyunsaturated Phospholipid Bilayers. *Biophys. J.* **1998,** *75*, 896-908.

16. Baumler, S. M.; Reidy, T. M.; Blanchard, G. J., Diffusional motion as a gauge of fluidity and interfacial adhesion. Supported alkylphosphonate monolayers. *J Colloid Interf Sci* **2016,** *468*, 145-155.

17. Blanchard, G. J., A study of the state-dependent reorientation dynamics of oxazine 725 in primary normal aliphatic alcohols. *Journal of Physical Chemistry* **1988,** *92* (22), 6303-6307.

18. Blomgren, E.; Bockris, J. O. M.; Jesch, C., The adsorption of butyl, phenyl and naphthyl compounds at the interface mercury-aqueous acid solution. *J. Phys. Chem.* **1961,** *65* (11), 2000-2010.

19. Karpovich, D. S.; Blanchard, G. J., Direct Measurement of the Adsorption Kinetics of Alkanethiolate Self-Assembled Monolayers on a Microcrystalline Gold Surface. *Langmuir* **1994,** *10* (9), 3315-22.

20. Schessler, H. M.; Karpovich, D. S.; Blanchard, G. J., Quantitating the Balance between Enthalpic and Entropic Forces in Alkanethiol/Gold Monolayer Self Assembly. *J. Am. Chem. Soc.* **1996,** *118* (40), 9645-9651.

21. Karpovich, D. S.; Blanchard, G. J., Dynamics of a tethered chromophore imbedded in a self-assembled monolayer. *Langmuir* **1996,** *12* (23), 5522-5524.

22. Baumler, S. M.; Blanchard, G. J., The Influence of Metal Ions on the Dynamics of Supported Phospholipid Langmuir Films. *Langmuir* **2017,** *33* (12), 2986-2992.